University of Southampton

Faculty of Physical Sciences and Engineering

Optoelectronics Research Centre

POWER-SCALING OF WAVELENGTH-FLEXIBLE TWO-MICRON FIBRE SOURCES

By

ANTONIN BILLAUD

Thesis for the degree of Doctor of Philosophy

September 2017

UNIVERSITY OF SOUTHAMPTON

ABSTRACT

FACULTY OF PHYSICAL SCIENCES AND ENGINEERING

OPTOELECTRONICS RESEARCH CENTRE

DOCTOR OF PHILOSOPHY

POWER-SCALING OF WAVELENGTH-FLEXIBLE TWO-MICRON FIBRE SOURCES

By Antonin Billaud

In this thesis we explore thulium doped silica fibre based sources, focusing on laser and amplified spontaneous emission behaviours. We analyse new ways of improving fibre cavity performances by first demonstrating a novel way of manufacturing doped fibres showing high pump absorption whilst retaining ease of use for cleaving and splicing. This new process offers a trade-off between circular and non-circular fibre geometries by maintaining advantages of both configurations. An implementation process on fibre drawing towers is detailed for future large scale production of highly circular active fibres with high mode scrambling, resulting in high pump absorption comparable, and potentially higher, to octagonal fibre. We then introduce a new way of improving fibre tip movement insensitivity in free-space feedback arms by utilising corner-cubes as reflective elements, with results showing transverse fibre tip movement of more than a millimetre in specific configurations whilst maintaining high feedback efficiency. Output power variation of less than 35% was demonstrated over a translation window of ±1.2mm in some cases.

Exploiting the movement insensitive properties offered by a corner-cube, a tunable ring laser based on fibre tip movement and a Fabry-Perot etalon is demonstrated. Up to 5nm of quasi-continuous fine tuning is proven with a theoretical accuracy of 8pm/μm fibre tip movement and a linewidth lower than 1.5GHz is demonstrated. Potential for rapid wavelength scanning and for much broader tuning over a window of few tens of nm is proposed with further modifications of the experimental setup to allow wider fibre tip movement without feedback losses appearing.

Focus is then centred on the broad tuning capabilities on thulium doped silica fibres and a CW laser source allowing tuning over more than 130nm in the 2μm band is described. Tuning is achieved by the use of a digital micro-mirror device (DMD) coupled with a diffraction grating, allowing further spectral shaping. Up to 8.5W of output power is displayed, pump power limited, with capabilities for multi-wavelength emission and spectral power density shaping by adjustment of the micro-mirror matrix reflective pattern. Modification of the system was explained in order to achieve different requirements, either by improving tuning range, accuracy or minimal linewidth.

Utilising the fast dynamics of a doped fibre cavity, a cavity is built around an acousto-optic modulator to frustrate lasing in order to create a feedback tolerant pulsed amplified spontaneous emission (ASE) source. This source was designed to allow generation of a pulsed wavelength-controllable ASE via the use of a DMD coupled with a diffraction grating. A core-pumped setup is demonstrated, reaching tuning from 1860 to 1950nm and a cladding-pumped architecture is built for longer wavelengths generation to improve compatibility with amplifier stages. This source displayed tuning performances from 1940 to 2020nm with peak power of up to 1.5kW and pulses shorter than 100ns. Multi-waveband behaviour is demonstrated and output bandwidth is controlled through the DMD. A cladding-pumped amplification stage is described and amplification of the ASE output by 15dB, reaching up to 72W, pump limited, was demonstrated corresponding to peak powers of more than 5kW. Prospects for pumping of a ZGP OPO cavity with an ASE are discussed, detailing the potential benefits of utilising a bandwidth-adjustable ASE source for mid-infrared generation.

Table of Contents

Table of Figures

Declaration of Authorship

I, Antonin Billaud, declare that the thesis entitled "Power-scaling of wavelength-flexible 2µm fibre sources" and the work presented in the thesis are both my own, and have been generated by me as the result of my own original research.

I confirm that:

-this work was done wholly or mainly while in candidature for a research degree at this University;

-where any part of this thesis has previously been submitted for a degree or any other qualification at this University or any other institution, this has been clearly stated;

-where I have consulted the published work of others, this is always clearly stated;

-where I have quoted from the work of others, the source is always given. With the exception of such quotations, this thesis is entirely my own work;

-I have acknowledged all main sources of help;

-where the thesis is based on work done by myself jointly with others, I have made clear exactly what was done by others and what I have contributed myself;

-parts of this work have been published as: [see Appendix]

Signed:

Date:

Acknowledgments

I would like to thank my supervisors, Professor Andy Clarkson for the freedom he gave me during my PhD and the wide range of projects he suggested, and Dr Peter Shardlow for following my work, advising me and being there whenever I had questions, however dumb they were and however busy he was.

I would also like to thank the members, present and past, of the ASSS group for their help. In particular Dr Jae Daniel, for his availability to answer my questions regarding his work whilst living on the other side of the world and Dr Alex Butler for his steady rate of answers to my questions with a ratio of one a day. To the all PhD students from the ASSS group, thank you for being there, allowing me to discuss physics, borrow stuff (with or without their knowledge) and always discover new things.

I am particularly grateful to Laura Bimboes for supporting me every day, particularly during writing, and lending me her ear to explain my work on a daily basis

I would like to acknowledge Leonardo Airborne & Space Systems for their support, and its members, Dr Ian Elder and Dr Rob Lamb, for the constructive discussions and the lending of crucial components.

Notation

AOM	Acousto-Optic Modulator
AOTF	Acousto-optic tunable filter
ASE	Amplified Spontaneous Emission
CW	Continuous Wave
DM	Dichroic Mirror
DMD	Digital Micro-mirror Device
FP	Fabry-Perot
FSR	Free Spectral Range
FWHM	Full Width Half Maximum
FWTM	Full-Width at Tenth of Maximum
HR	High Reflectivity
LMS	Localised Mode Scrambler
MCVD	Modified Chemical Vapour Deposition
MFD	Mode Field Diameter
MEMS	Micro-Electro-Mechanical Systems
MO	Master Oscillator
MOPA	Master Oscillator Power Amplifier
MOFA	Master Oscillator Fibre Amplifier
MPE	Maximum Permissible Exposure
NA	Numerical Aperture
OAP	Off-Axis Parabolic (mirror)
OCT	Optical Coherence Tomography
OPO	Optical Parametric Oscillator

OSA	Optical Spectrum Analyser
PA	Power Amplifier
PM	Polarisation Maintaining
RF	Radio Frequency
SBS	Stimulated Brillouin Scattering
SPD	Spectral Power Density
SRS	Stimulated Raman Scattering
WDM	Wavelength-Division Multiplexing
ZGP	Zinc Germanium Phosphide

Chapter 1. Introduction

1.1 Motivation

Over the past few decades, high power lasers have been implemented in many markets (metal and plastic processing, medical applications…), replacing previous technologies and offering new capabilities. Thus many goods have benefited from the use of lasers during their manufacture such as laser marking of materials ranging from plastics to metals. In areas such as automotive and industrial manufacturing, high power lasers offer the possibility for fast processing and welding of metals with many other advantages such as their flexibility of use, compared to arc welding for example which requires access to both sides of the part to weld. Lasers also have many medical applications, ranging from surgery with ablation of tissues to cancer detection. The semiconductor industry is a continuously growing market, using lasers for lithography purposes. A new area of development making use of the availability of high power lasers is the additive manufacturing type of processing which uses laser sintering in order to create parts more complex than ever possible with traditional techniques. The defence sector is also heavily investigating new laser based technologies, driven by the demand in directed energy applications.

Optical fibre lasers possess a main advantage for power scaling from their robust architecture and can be used for many of the aforementioned applications. Based on the principle of total internal reflection, signal and pump are both guided in a fibre, allowing long interaction lengths and tight confinement resulting in distributed gain and a laser having low threshold and high slope efficiency compared to conventional bulk solid-state lasers. Fibre core diameters are usually kept below 40µm to ensure good beam quality, up to near perfect beam profile for single-mode fibres whilst fibre cladding diameters are in the order of few hundreds of microns with a device length ranging from one to tens of meters. From a power scaling point of view, a thin and long device leads to low thermal load per unit length, is easier to thermally manage at high powers and is less sensitive to thermal effects. High power fibre lasers often operate in a cladding-pumping configuration where signal is generated and confined in an inner core doped with active ions, whilst the pump light propagates in an inner-cladding. This configuration allows the use of low brightness laser diodes for pumping whilst maintaining single mode operation of the generated signal which is quite beneficial for power scaling. The first demonstration of a kilowatt-level near diffraction limited fibre laser was achieved in 2004 [1.1] with 1.36kW in Yb-fibre lasers and increased regularly with more than 10kW single mode in 2009 [1.2]. Spatial beam combination also became more prominent, allowing easy access to multi-kW output by combining kW level sources, reaching more than 100kW over the years with a multi-mode output having a M^2 of 50 [1.3]. Moreover, many off-the-shelf high power fibre lasers achieve high conversion efficiencies, particularly based on ytterbium fibres, with slope efficiencies reaching more than 90% via diode pumping [1.4].

Fibre lasers are of high interest as they offer the advantage of conserving a similar cavity architecture when operating from the Watt level to kW level even though the latter requires better thermal management. and their fabrication is highly automated, benefitting from the techniques and components previously developed for the telecom industry, fibre laser manufacturing can be highly automated via the use of perfected processes such as Modified Chemical Vapour Deposition (MCVD) to produce high quality doped fibre or fibre fusion splicers and cleavers necessary for fibre fusing. These high quality reliable components with high accuracy greatly reduce the complexity and time of construction of high power lasers, promoting rapid manufacturing.

Fibre lasers seem to offer many benefits compared to other laser systems; particularly for high beam quality and high average power. However, compared to bulk lasers, they only offer low pulse energy capabilities due to low maximal energy storage and as the tight mode confinement obtained from the small fibre core coupled with the long interaction length leads to much lower nonlinear loss thresholds than for bulk lasers. This is particularly true for a pulsed mode of operation where high peak power is targeted. Up to tens of mJ have been demonstrated in fibre sources with pulse length in the nanosecond regime, requiring specific cavity designs that are detrimental to beam quality. Improving these performance figures would require drastic architecture changes for small pulse energy gains compared to bulk lasers where tens of mJ is easily achieved and power scaling to much higher values can be done through increase of the resonator mode size [1.5].

Even though fibre lasers in pulsed regime cannot compete with bulk lasers energy wise, reaching the mJ-level in fibre configurations [1.8] with 2mJ achieved in fibreised femtosecond regime in 2011 [1.9] and 26mJ in Q-switched configuration in 2012 [1.10] whereas bulk laser such as gas achieved multi-tens of J in pulsed regime decades ago [1.11] and are now commercially available form company such as Coherent (up to 100mJ at 1micron) or Thales (up to 12J at 1064nm and 8J at 532nm from the GAIA products). Fibre lasers however offer many advantages justifying their quick implementation in the manufacturing industry such as their easy-to-implement thermal management and low sensitivity to thermal changes previously mentioned. Another of their assets is their monolithic structure, avoiding the need for alignment and thus solving potential issues created by vibrations and movement often occurring in an industrial environment as well as long lifetime for such high power lasers without any maintenance needed.

In this thesis we focus on sources around 2µm either lasers or amplified spontaneous emission sources (ASE). Laser sources around 2µm have been intensively investigated first in bulk lasers and then in fibre systems as these sources have a lot of potential applications, such as in defence, engineering or even for medical purposes. This wavelength range is in high demand as 2µm light is in the ’eye-safe’ zone which makes it a the wavelength of choice for a range of applications such as LIDAR [1.6], free space communications [1.7] or defence counter-measures (This zone is considered as ’eye-safe’ as the absorption within the eye is increased around this wavelength range compared to near IR, leading to an increase in maximum permissible exposure (MPE) limits but direct exposure to a significant amount of power remains dangerous whatever the wavelength.). Most of the 2µm sources are based on thulium ions which, in a silica host, have a large fluorescence emission band from 1600 to 2200nm, allowing high wavelength tunability in this window with simple cavity configurations. Such a

wide wavelength band is quite attractive as it covers many spectroscopic features such as absorption bands of specific chemical components, from water vapour in the 1800-1920nm-band to CO_2 and methane. A strong absorption line of liquid water is also observed at 1940nm, making 2µm systems attractive for medical applications. Many other materials present absorption features in the thulium emission band such as plastics and polymers, allowing better cutting and welding of these materials than via current techniques. From a power scaling point of view in fibre lasers, 2µm sources compared to current 1µm sources allow larger fibre core in single mode operation, thus allowing higher energy storage (i.e. potential peak power) before reaching thermal or non-linear limitations.

ASE sources are of particular interest in this thesis as they offer many benefits compared to laser sources. Even though ASE is often seen as a nuisance or noise in laser systems, one of their advantages is the compatibility with multimode fibres whilst avoiding modal interference, and accordingly forbidding beam pointing stability issues to occur. This is possible due to ASE sources short coherence length compared to typical laser sources. Moreover, smoother spectra can be achieved as no longitudinal modes exist.

The medical field could also benefit from new tunable sources especially around 2µm as this matches water absorption lines and could be used for detection systems or laser surgery such as cancer cell eradication. A change of output wavelength, from one water absorption line to another, could lead to an output having the same power and Spectral Power Density (SPD) but with a different penetration depth in tissue.

1.2 Outline of thesis

In this thesis we explore new ways of improving fibre laser designs to optimise pump absorption in cladding pumping architectures and increase cavity stability by improving insensitivity to vibrations and movements. Novel resonator architectures designed for spectral control are explored based on components seldom used for this purpose, either in laser or ASE regime. All the experimental results reported in this thesis were achieved with thulium doped silica fibre but most of the new configurations described here can be applied to other wavelength bands through the use of the relevant active ions.

In chapter 2 the relevant background theory related to fibre laser and ASE operation is detailed. First, the main applications benefitting from the advantages offered by 2µm sources are listed. Then the matching rare-earth elements in the 2µm band such as thulium between 1.6 and 2.1µm or holmium between 2 and 2.2µm are described with the associated properties, particularly spectroscopic features and the cross-relaxation phenomena. Following, optical fibres are described, from single-mode to multimode operation, including characterisation methods. Beam propagation in free-space and characterisation of beam quality are explained as well as the various optical pumping schemes available with doped fibres. ASE sources are highlighted and their operation is explained, focussing on their advantages compared to conventional lasers, particularly for multi-mode fibre systems. Some of the most common tuning techniques compatible with fibre lasers are described before detailing the power scaling considerations related to fibre based systems. The Master Oscillator

Power Amplifier (MOPA) concept is explained, exploring its advantages. Lastly, a study of power-scaling limitations is made, focussing on the main detrimental non-linear effects such as Stimulated Brillouin Scattering (SBS), Stimulated Raman Scattering (SRS) and optical damage.

In chapter 3 we describe a new method to improve pump absorption in cladding-pumped architectures. We first describe the current fibre geometries used in double-clad fibres, their fabrication process and their limitations. In particular, we focus on the splicing issues linked to the use of non-circular fibre cladding geometries and we introduce a new fibre cladding alternating between circular and a D-shape profile. This fibre would have the advantages of a non-circular fibre, improving pump absorption through mode scrambling, whilst staying mostly circular for ease of cleaving and splicing. We then describe a fabrication process allowing the creation of such fibres by localised laser processing of the cladding surface of a circular fibre. A first demonstration of fabrication is made and a characterisation setup is described to measure pump absorption improvement and intrinsic losses. Experimental results are shown, linking length of the D-shaped section to pump absorption and depth of processing to losses. This method shows high improvement of pump absorption by only adding few D-shape points in the cladding surface. Finally, we propose a way to implement this fabrication process on the fibre drawing process by adding a CO_2 laser unit in order to produce fibres with localised mode scramblers on a large scale.

In chapter 4 we describe a new way of improving stability in free space feedback arms of fibre laser cavities. These cavities often contain a free-space part which requires tight alignment of the fibre tip for collimation and a high reflectivity plane mirror at the end of the feedback arm. Any movement of the fibre tip relative to the collimation optic due to heating or vibrations can lead to feedback efficiency drop, resulting in loss of power and damage inside the cavity. We demonstrate theoretically that by using a corner-cube as main reflective element instead of a plane mirror, tolerances on fibre tip movement can be increased by more than two orders of magnitude, allowing transverse fibre tip movement of more than a millimetre for a single-mode fibre whilst conserving high feedback efficiency. Reflectivity of a feedback arm as a function of displacement of the fibre tip before collimation is calculated and a linear cavity laser is constructed. Experimental verification shows tolerance improvement from 10µm with a plane mirror to up to 1.2mm with a corner cube. Limitations on this improvement are described and ways for further development are given. A new tuning technique based on a movement insensitive feedback arm is then proposed by the addition of a Fabry-Perot etalon inside the previous feedback arm. A ring laser containing this feedback arm is suggested to achieve a new way of reliable precise wavelength-tuning controlled by lateral fibre tip movement. Theoretical calculations are described, providing the upper limits of such a system. Demonstration of quasi-continuous wavelength tuning over few nanometers is shown by transverse fibre tip movement and prove high correlation with expectations. Requirements to avoid mode hopping and achieve higher control over tuning accuracy are described.

In chapter 5 we focus on a new cavity design offering Watt-level output power and wavelength tuning based on the utilisation of a Digital Micro-mirror Device (DMD) for wavelength selection. Such a system offers rapid agile tuning with accurate fast switching of the operating wavelength whilst conserving high efficiency and would

provide high reconfigurability depending on the user's needs. By exploiting a diffraction grating spatially chirping the beam, followed by a DMD, computer-controlled wavelength-selective feedback is achieved. This system showed up to 8.5W of output power, limited by pump power, with tuning over 131nm from 1913 to 2044nm and high beam quality with a M^2 of less than 1.2 at any wavelength. Linewidth of less than 0.13nm were achieved by reduction of the reflection area whilst conserving high feedback efficiency. Taking advantage of the DMD capabilities, multi-wavelength behaviour was demonstrated by having more than one reflective area on the micro-mirror matrix leading here to demonstration of three wavelengths operating in parallel. Adjustment of the reflective areas size in the non-chirped dimension allowed modulation of the feedback efficiency for each wavelength individually and thus, control of the Spectral Power Density (SPD) of a dual-wavelength spectrum was demonstrated with full spectral control managed by only one component.

In chapter 6 we introduce the benefits of ASE sources compared to laser operation such as the compatibility with multimode fibres without beam pointing instability arising. Current techniques to generate ASE outputs are described as well as their limitations. A cavity design allowing the creation of an ASE source whilst maintaining feedback inside the cavity is then introduced based on the use of an Acousto-Optic Modulator (AOM). The addition of an AOM forbids lasing whilst tolerating feedback. Demonstration of pulsed ASE behaviour in a cavity containing a feedback arm and an output coupler is shown in two configurations based on thulium fibres, targeting either short or long wavelengths of the thulium emission band. A new design based on the previous DMD-controlled tunable laser with the addition of the AOM is explored, allowing wavelength-controllable ASE to be generated through wavelength-selective feedback. Results show up to 7W output power, pump limited, and pulse behaviour for several repetition rates is characterised. Furthermore, the possibility of spectral shaping by control of the reflective area shape on the DMD is described. Lastly, an amplifier stage is developed to reach high peak power for a future Zinc Germanium Phosphide (ZGP) OPO pumping experiment. This amplification stage allows for up to 15dB amplification, reaching 72W of output power, at the cost of slight spectral broadening. Theoretical limits of the amplification such as SRS and SBS are discussed.

In chapter 7 we draw our conclusions of the work presented in this thesis. The key results of each experiments are summarised and particular focus is given on future prospects of the concepts developed throughout this thesis, particularly the possibility of a new generation ASE sources for many applications such as OPO pumping.

1.3 References

1.1. Jeong, Y., et al., *Ytterbium-doped large-core fiber laser with 1.36 kW continuous-wave output power.* Optics Express, 2004. **12**(25): pp. 6088-6092.

1.2. Stiles, E., *New developments in IPG fiber laser technology*, in *5th International Workshop on Fiber Lasers*. 2009.

1.3. Shcherbakov, E., et al. *Industrial Grade 100 kW Power CW Fiber Laser*. in *Advanced Solid-State Lasers Congress*. 2013. Paris: Optical Society of America.

1.4. *Nufern Inc.*; Available from: http://www.nufern.com/.

1.5. Banerjee, S., et al., *High-efficiency 10 J diode pumped cryogenic gas cooled Yb:YAG multislab amplifier.* Optics Letters, 2012. **37**(12): pp. 2175-2177.

1.6. Sugimoto, N., et al., *Eye-Safe 2.1µm Ho Lidar for Measuring Atmospheric Density Profiles.* Optics Letters, 1990. **15**(6): pp. 302-304.

1.7. Rockwell, D.A. and G.S. Mecherle, *Wavelength selection for optical wireless communications systems.* Optical Wireless Communications Iv, 2001. **4530**: p. 27-35.

1.8 Jauregui, C, et al.,High-power fibre lasers, NATURE PHOTONICS, NOV 2013, Volume 7 Issue 11, pp. 861-867

1.9 Eidam, T.et al. *Fibre chirped-pulse amplification system emitting 3.8 GW peak power*. Opt. Express**19**, 255–260 (2011).

1.10 Stutzki, F.et al. *26 mJ, 130 W Q-switched fibre-laser system with near-diffraction-limited beam quality*. Opt. Lett.**37**, 1073–1075 (2012).

1.11 Dragulinescu, D. et al., *A 23 Joules, CO2 pulsed laser*, Revue Roumaine de Physique, 1976, volume 21, pp.665-669

Chapter 2. Background

An optical fibre source offers both waveguiding and signal amplification in a single region: the doped core which allows for high power scaling whilst conserving a robust architecture. The long interaction length offered by the use of active fibres coupled with mode confinement and high overlap of the doped region with the resonator mode results in high small-signal gain and low thresholds with ease of thermal management. Moreover, single-mode operation is permitted at high power levels thanks to the waveguiding property of optical fibres, achieving near ideal Gaussian beam profiles in output.

Laser sources operating around 2µm have been a subject of interest for many years. The development of active fibres doped with rare earth thulium and/or holmium ions have allowed rapid progress in this area of research. The first two-micron lasers were based on bulk crystals; however fibre lasers operating in this band quickly followed [2.1, 2] and, with advent of higher brightness pump diodes and efficient cladding pumping schemes, have been scaled in power to the kilowatt regime [2.3, 4], surpassing the performance of bulk lasers in terms of average power and efficiency.

In this chapter we discuss the main fields of interest for 2µm systems and the wavelength tuning techniques associated with 2µm fibre sources. We then investigate the various dopant options for laser emission around the 2µm wavelength, focussing particularly on thulium ion and its advantages for power scaling. We discuss the mode guidance of optical fibre and theory of Gaussian beam propagation in free space as well as the different optical pumping architectures associated with active fibres that are core and cladding pumping. Finally, we describe the relevant strategies for power scaling within a fibre-based architecture, highlighting the seed/amplifier MOPA combination and focussing on the limiting phenomena occurring in fibre architecture such as the detrimental effects of the relevant nonlinear processes and end-facet damages.

2.1 2µm sources applications

2.1.1 Laser processing

The latest generation fibre lasers are of main interest for future prospects in laser processing, from cutting and welding to engraving as they offer the possibility of tight focusing coupled with high power beams and can adapt to many types of materials. Laser processing is based on the material absorption; thus different processing wavelengths are required depending on the materials. Metal processing is currently processed at 1 or 10µm by the use of Yb-based solid-state lasers or CO_2 lasers due to their suitable wavelengths as well as their convenience and reliability. Processing of plastic however is quite inefficient at theses wavelengths due to the poor absorption whilst 2µm sources are of high interest due to their high absorption coefficient [2.5]. Moreover, laser processing requires high power and good beam quality for high processing efficiency which can potentially easily be

achieved in fibre-based 2µm sources due to high pump power commercially available whilst maintaining single-mode operation by scaling of the core radius compared to Yb-doped fibre lasers currently used.

2.1.2 Thulium lasers as pumping sources

Thulium fibre lasers are investigated as a pumping stage for a broad range of systems such as Ho-based lasers, either crystal of fibres. Holmium fibres offer the possibility to emit beyond the 2µm band (with an emission band centred around 2.1µm) but cannot be easily and efficiently pumped by currently available laser diodes. However, they allow in-band pumping around 2µm, offering the capability of a high quantum efficiency holmium laser pumped by a thulium fibre laser. Other solid-state lasers based on crystals work with a pumping transition addressed by a thulium fibre laser such as Ho:YAG lasers or Cr-based crystals. Ho:YAG crystals are pumped at 1907nm and are used to generate high peak power Q-switch emission at 2.1µm for many applications, ranging from laser surgery or to pumping of ZGP crystals for mid-IR generation for example [2.6-9]. Thulium fibre lasers are also used in 'thulium-pumped-thulium' schemes where a first Tm fibre laser is used to pump a second one as in-band pumping, generating longer wavelength with high slope efficiency. Pumping is usually done around 1900nm and signal is generated around 2000nm with slope efficiencies of more than 90% [2.10-13].

2.1.3 LIDAR and free-space communications

The 2µm range overlaps well with a high transmission atmospheric window whilst also corresponding to a high liquid water absorption zones. Such properties yield great interest for free-space applications as the liquid water absorption features make the 2µm area an 'eye-safe' zone [2.14] particularly fitting for free-space communications [2.15] where low loss of signal is desired whilst guaranteeing user safety is compulsory. Figure 2.1 shows the atmospheric transmission spectrum around the 2µm where high transmission can be observed for signals over 2µm whilst wavelengths between 1800 and 2000nm suffer from high absorption.

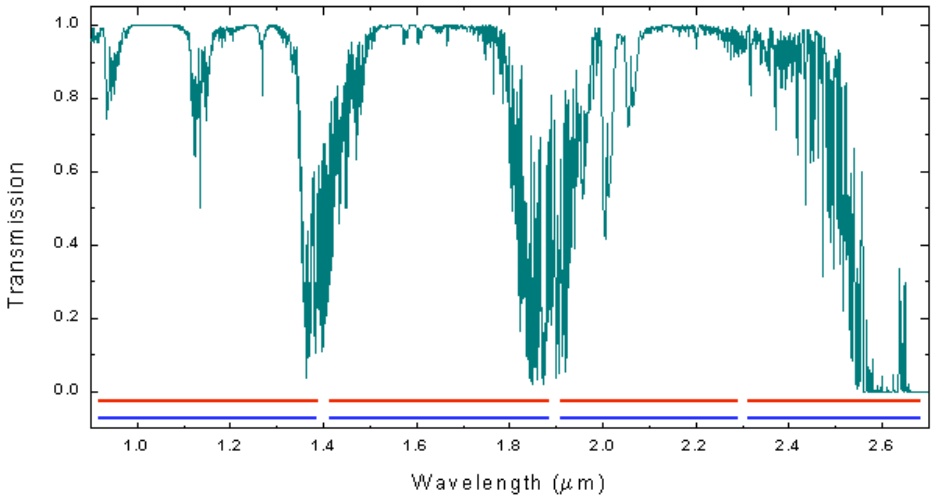

Figure 2.1 Atmospheric transmission spectrum around the 2µm wavelength, data from [2.16]

Absorption lines are heavily present in the 1700-2100nm region for many gaseous forms such as methane, carbon dioxide or water vapour [2.17] making such systems, particularly tunable ones, of great interest for LIDAR applications. Such sources can be used for simple gas detection to more complex LIDAR systems, where accurate position, speed and atmospheric concentration of a specified chemical is achieved [2.18-24].

An example of such application was the I-WAKE European project in the early 200s which consisted in using a Doppler-LIDAR system at 2µm in airports to detect wake vortex formations during take-off and landing. These turbulences are what defines the minimal waiting time required between each take-off/landing and the use of an eye-safe system for their detection and characterisation was primordial to increase airport capabilities whilst ensuring flight safety.

2.1.4 Medical uses

Many medical applications already benefit from 2µm solid-state lasers due to the short penetration depth in liquid water which is in the millimetre-scale compared to other commercially available systems based on other wavelengths (e.g. 1 or 10µm) giving penetration depth either in the 10s of centimetre or micron-scale [2.25]. A suitable penetration depth is required for skin medical treatment to achieve an optimal result whilst avoiding unwanted tissue damage and a long processing time. Many benefits could come from medical use of 2µm systems in many areas such as soft tissue surgery, Optical Coherence Tomography (OCT) or acne treatment [2.26-29]. Thulium fibres offer a wide wavelength-tuning range around 2µm allowing potential for accurate penetration depth selection by tuning of the source wavelength. 2µm lasers have been used over the years in surgery for cutting and ablation, particularly in lithotripsy [2.62], but also for intracranial surgery [2.63] as well as to favour blood coagulation during critical and cosmetic operations [2.64-65].

2.2 Rare-earth dopants in silica fibres for emission in the 2µm band

2.2.1 Thulium fibres

Thulium is one of the rare-earth (RE) elements whose ion form Tm^{3+} offers a laser transition around 2µm and is thus an interesting dopant for silica-host active fibres. Figure 2.2 shows the emission and absorption cross-sections of a Tm^{3+} doped fibre [2.30] and broad emission is observed from 1600 to 2100nm.

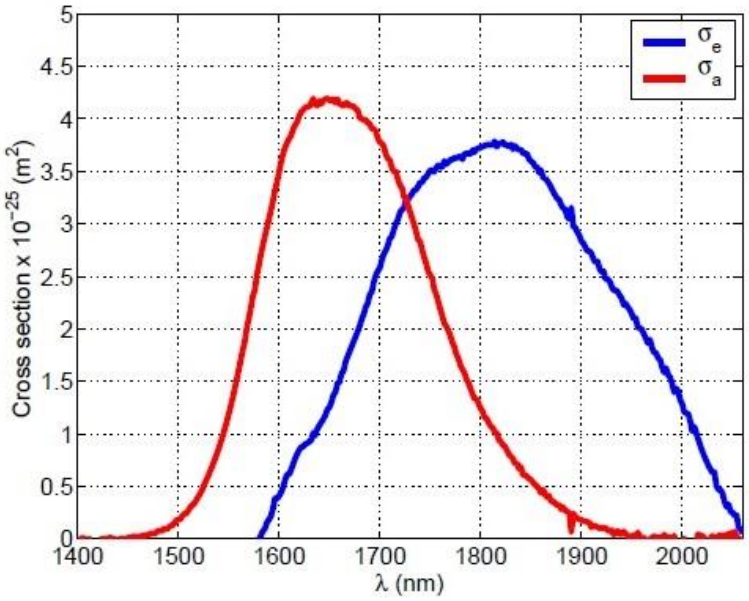

Figure 2.2 Emission and absorption cross-sections of $Tm^3$from [2.30]

Due to their broad emission range, Tm-doped silica fibres are of great interest due to their potential for broad wavelength tuning which could benefit many applications. Thulium fibres were investigated in the 80's and 90's with the first laser demonstrations limited to relatively low powers (~ few milliwatts) [2.1]. The performance of Tm-doped fibres has since then improved dramatically owing to optimisation of fibre fabrication processes (modified chemical vapour deposition process (MCVD)) allowing better control of the doping profile, lower OH impurity concentration control as well as higher Tm ion concentrations. In silica host, thulium laser emission has been demonstrated from 1665nm up to 2200nm [2.31, 32].

Figure 2.3 shows the energy levels of the Tm^{3+} ion and two pumping levels are available: from $^3H_6$ to $^3H_4$ or from $^3H_6$ to $^3H_5$, corresponding to 793nm and 1550nm. At first glance 1550nm pumping seems much more interesting as this would allow a conversion rate up to 78% (for an emission at 2µm) while 793 nm pumping would only allow a conversion rate up to ~40%.

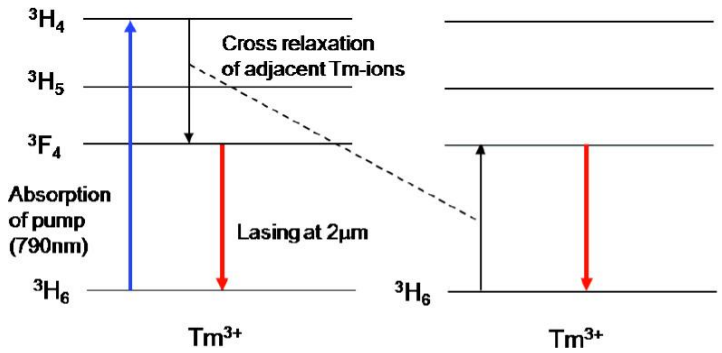

Figure 2.3 Energy levels of the thulium ion showing the cross-relaxation process [2.33]

But it has been shown experimentally that a 2-for-1 cross-relaxation process can occur if the concentration of Tm^{3+}ions is high enough [2.34-36]. Figure 2.3 shows pumping of a thulium ion with a 79x nm pump and its decay to the upper laser level. A thulium laser with a pumping source at 793 nm can be considered as a quasi-three-

level laser with an upper pump level ($^3H_4$) much higher than the 2µm laser energy level ($^3F_4$). This means that an electron excited from the ground-level to the upper pump level ($^3F_4$), decays non-radiatively to the upper laser level ($^3F_4$) via multi-phonon emission and then decays radiatively to the ground-level manifold by emitting a photon at 2µm. If Tm^{3+} concentration is high enough in the host, Figure 2.3 shows that dipole to dipole energy transfer can happen during this decay from $^3H_4$ to $^3F_4$ and thus from one pump photon at 793nm, two electrons have been excited from the ground level to the upper laser level and can generate two photons at 2µm. Another advantage of pumping at 793nm instead of 1550nm is the availability of pump power. 1550nm lasers are often Er/Yb fibre-based systems already being pumped by another laser at 980nm. Thus pumping at 793nm from laser diodes has a greater potential for higher output power and better wall-plug efficiency.

Whilst the laser transition of the thulium ion covers from 1600 to 2200nm, it is extremely difficult to cover the entire emission range with just one single fibre source. Trade-offs must be made when aiming for the short or long wavelengths of this range due to gain saturation caused by amplified spontaneous emission at short wavelengths coupled with a wavelength-dependent variation of quasi-three level behaviour.

Signal reabsorption of shorter wavelengths at low excitation levels moves the gain towards longer wavelengths where a 4-level behaviour is observed whilst at high levels of excitation, long wavelength operation is difficult due to high gain for short wavelength ASE. Thus, to reach the short wavelengths of the laser transition where high signal reabsorption occurs, short cavity length and high excitation density are essential. This is achieved with low doping concentration and core pumping which offers high pump brightness. To reach the long wavelength region, however, long fibre length with low brightness pumping from cladding pumping is beneficial. From the low emission cross-section at long wavelengths, high ion concentration is needed and long device length is required, making cladding-pumped systems more convenient. Such systems are often pumped with low brightness laser diodes, usually at 79xnm to benefit from the cross-relaxation phenomena. Core-pumped systems (often pumped at 1550nm) require much lower doping concentration to achieve similar absorption levels and operate towards the short wavelength range (1700 to 1950nm). Thulium-doped fibre lasers systems have been demonstrated at output with high power capability [2.4] via the use of amplifier stages, combined with high efficiency [2.3] and the possibility of narrow-linewidth high power output [2.37]. Thulium fibre laser systems are currently commercially available at mid-power (10s of Watts) for different suppliers such as Advalue Photonics or Cybel and with IPG offering up to 200W single-mode and multi-mode output powers of more than 500W possible on request.

2.2.2 Holmium fibres

Another focus of interest has been the development of holmium fibres to generate wavelengths over 2µm. Previous work with thulium fibres showed the difficulty to emit over 2.1µm due to the emission band of thulium while holmium offers the possibility of easily emit over 2.1, with demonstrations at 2.2µm [2.38] as its emission-cross section is still significant compared to Tm^{3+} after 2µm (Figure 2.4) [2.39].

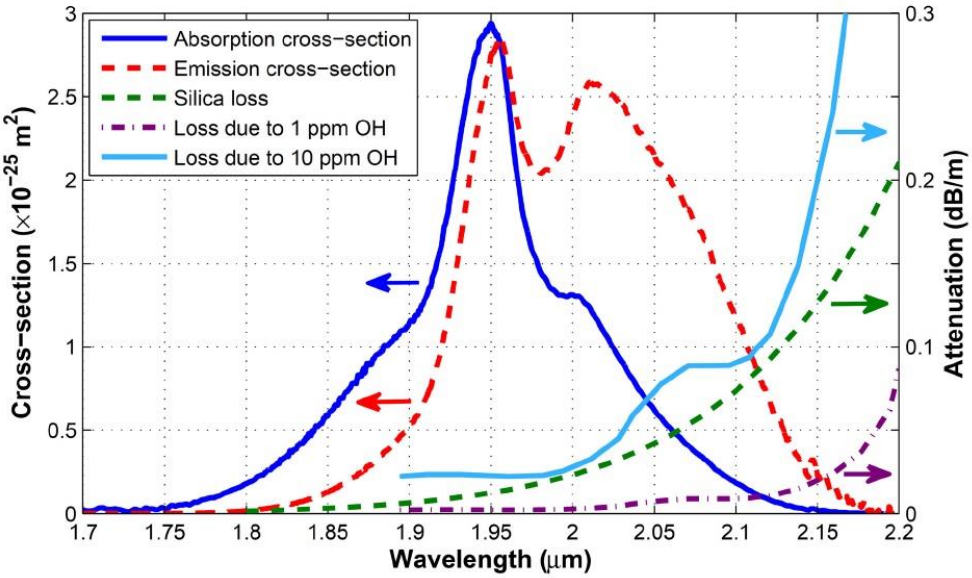

Figure 2.4 Emission and absorption cross-section of $Ho^{3+}$and silica and OH losses in the 2µm window from [2.39]

However, to generate longer wavelengths than 2.15µm one must face many problems, mainly due to the silica host. Figure 2.4 shows that silica fibres start to strongly absorb after 2.1µm and thus does not permit the use of long fibre lengths without the penalty of high loss. OH presence also introduces strong absorption after 2.1µm. Therefore, an efficient holmium doped fibre for long wavelengths operation (typically in the 2.1 to 2.2µm window) needs careful control over the OH concentration and possibly the use of other hosts. One of the purposes of such sources is in the defence field as a pump source for OPOs (Optical Parametric Oscillator) to convert light to the mid-infrared (3 to 5µm) band by nonlinear frequency conversion. Nowadays, holmium based systems permit generation of output wavelengths over 2.1µm which are used for applications as varied as mid-IR generation or medical surgery [2.6, 8, 9] but thulium fibre lasers are often part of the system as holmium ions Ho^{3+} offer an absorption band around 1.95µm (see Figure 2.4) while the previous absorption band is around 1150nm. This is a convenient pump wavelength that offers high efficiency compared to pumping it at 1150nm. One of the area of further development is the capability of using a 'chain' of active-fibres, going from a 793nm pump to an active thulium fibre generating 1.9µm and then converting it to 2.1µm or more by using a holmium doped fibre or even utilising fibres co-doped with thulium and holmium [2.40, 41]. Achieving high efficiency in a Thulium fibre laser requires a high dopant concentration and accordingly a large core fibre leading to a poor beam quality. Whilst advantage of such a system would be that the brightness of the final beam does not depend on the brightness of the thulium laser (at same power) with a double-clad configuration thus the first conversion can be multimode without modifying brightness or efficiency of the final output

2.3 Optical fibre waveguides and beam propagation

2.3.1 Optical fibre waveguides

Optical fibres are used to guide light, keeping the light injected into it by the use of total internal reflection. They are composed of a core and a cladding made of glass, with a small step index between the two media with light guided in the core with low propagation loss and high resistance to irregularities at the core/cladding interface. Figure 2.5 shows a schematic in index of an uncoated fibre. In actual systems, the glass cladding in coated with a low index polymer to retain the guiding property of the cladding whilst improving protection and resistance to damages.

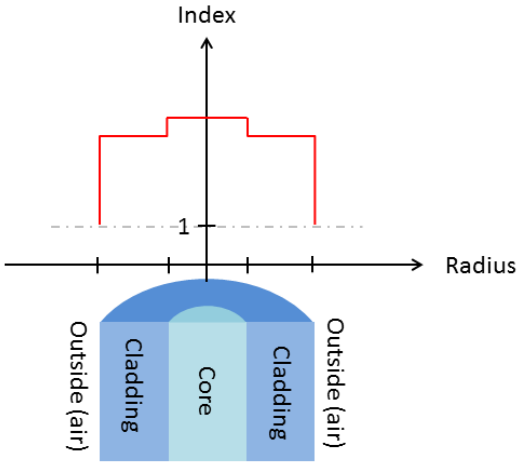

Figure 2.5 Index change in a step-index single-mode fibre

A smaller difference of index, however, leads to a smaller critical angle for total internal reflection. We can determine this maximal angle of acceptance θ from the fibre's numerical aperture (NA) where:

$$\mathrm{NA} = \frac{1}{n_0}\sqrt{n_{\mathrm{core}}^2 - n_{\mathrm{cladding}}^2} \tag{2.1}$$

Where n_0 is the refractive index of the medium before the fibre (generally air) and NA is $n_0 \sin\theta$ with θ the maximum acceptance angle of the fibre at the input face. By increasing the NA, rays with greater incidence angle are guided into the fibre and form electromagnetic field distributions in the fibre, also called modes. A parameter called the V parameter can be defined for step index fibres, which is related to the number of mode guided by the fibre [2.42] with:

$$V = k_0 r\sqrt{n_{\mathrm{core}}^2 - n_{\mathrm{cladding}}^2} \tag{2.2}$$

$$V = \frac{2\pi}{\lambda} r\mathrm{NA} \tag{2.3}$$

Where r is the core radius, k_0 the wavenumber and λ the propagating wavelength. If V<2.405, only the fundamental mode (which can be approximated to a mode having Gaussian intensity profile) can be guided through the fibre and the fibre is called single-mode. An increase of the V parameter will lead to an increase of the number of modes guided by the fibre. Above a value of 2.405, different modes are guided and methods might be applied to remove or decrease higher order modes if only the fundamental one is desired. This V-number is linked to the mode field diameter (MFD) for the fundamental mode in a step index fibre and can be calculated following Marcuse's equation [2.43]:

$$\omega_0 = r\left(0.65 + \frac{1.619}{V^{3/2}} + \frac{2.879}{V^6}\right) \tag{2.4}$$

Where ω_0 is the mode field radius at a $1/e^2$ point. In a step-index single mode-mode fibre, usually the core diameter is close to the mode field diameter. Single-mode step index fibres are designed to forbid propagation of all modes except the fundamental one through their design. The core diameter is matched to the MFD whilst the V-number is kept as close as possible to 2.405 to ensure single-mode operation.

2.3.2 Beam propagation and beam quality

The beam propagation of a Gaussian beam in free space is determined by:

$$\omega(z) = \omega_0\left[1 + \left(\frac{\lambda z}{\pi\omega_0^2}\right)^2\right]^{1/2} \tag{2.5}$$

Where z is the propagation distance from the waist position. From the waist position, we can define what is called the Rayleigh range (z_0) which corresponds to the distance where the beam area has expanded by a factor of 2 compared to the waist:

$$\omega(z_0) = \sqrt{2}\omega_0 \tag{2.6}$$

From the equations (**2.5**)and (**2.6**) we obtain:

$$z_0 = \frac{\pi\omega_0^2}{\lambda} \tag{2.7}$$

The beam propagation factor (M^2) is used to describe the far-field divergence of a beam compared to a diffraction-limited fundamental mode. This M^2 is determined by:

$$\omega(z) = \omega_0\left[1 + \left(\frac{M^2\lambda z}{\pi\omega_0^2}\right)^2\right]^{1/2} \tag{2.8}$$

Thus a beam with an M^2 bigger than 1 will have a divergence or waist M^2 bigger than a diffraction-limited beam at the same wavelength. One can also compare it to have a beam behaving like a diffraction-limited beam of higher wavelength.

2.3.3 Core and cladding pumping schemes

Active fibres are often used to convert light from one wavelength to another; the fibre's core is doped with different rare-earth ions then pumped at one wavelength and generates a longer wavelength. Optical fibres offer the possibility of a long overlapping length and high interaction of pump and signal. Pump light is injected into the fibre's core or cladding and no pump light escapes the cladding, leading to high pump absorption efficiency. Figure 2.6 shows cladding pumping in a fibre. In such a cladding pumping architecture, pump light is injected in the cladding.

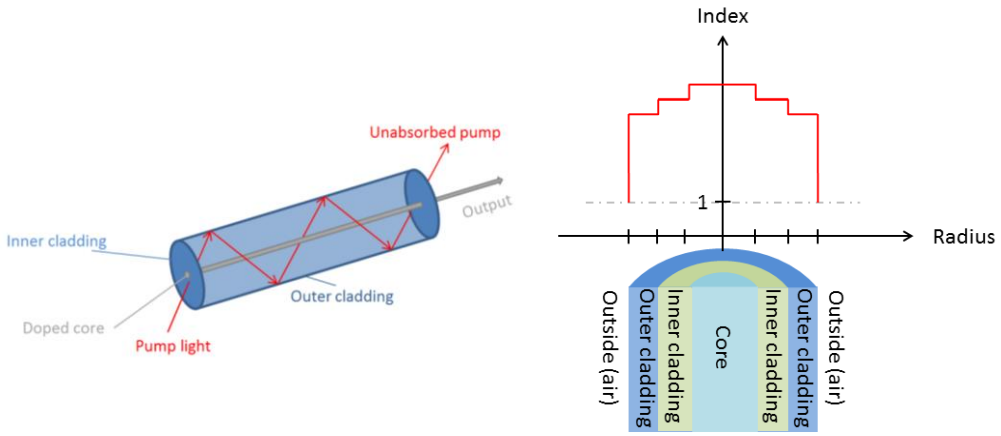

Figure 2.6 Schematic of a double-clad fibre for cladding pumping

Instead of having a core and a cladding, as in a core pumping architecture, the fibre possesses and inner and outer cladding with a second step index change. Therefore, pump light is guided into the inner cladding and interacts with the doped area, generating light which is then confined in the core. High-power fibre lasers are generally built in a cladded pumping arrangement with a lasing mode guided in the doped core and the pump propagating in the inner cladding. This configuration allows us to use lower pump brightness sources to be injected into the cladding whilst still generating a single-mode output with high brightness by the use of a core having a small V-number. This is an attractive way of power scaling whilst at the same time maintaining good beam quality [2.38].

2.4 Amplified Spontaneous Emission sources

An Amplified Spontaneous Emission source is referred to as an ASE source and offers a broad smooth output spectrum where no longitudinal modes are observed.

A solid-state laser consists of a cavity containing a gain medium optically pumped. In the small signal gain regime (low pump power), spontaneous emission is generated. Increasing pump power further, one reaches laser

threshold and longitudinal modes start to build up in the cavity (when gain overcomes losses). The light created is amplified by stimulated emission and has high temporal and spatial coherences with narrow spectral linewidth. To have an ASE source, the building of modes must be forbidden; this is usually done by suppressing feedback from one of the ends of the cavity. The most common method when utilising an active fibre as a gain medium is to angle-cleave one end to avoid light to be guided back into the core when reflected at the fibre/air interface (Fresnel reflection) [2.44]. Figure 2.7 shows a conceptual output spectrum of a laser and an ASE source, demonstrating longitudinal mode formation in the laser cavity and their presence in the generated spectrum.

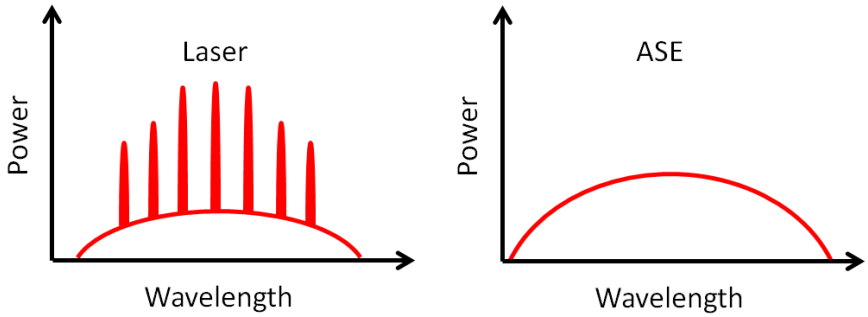

Figure 2.7 Spectral emission behaviour of a Laser and ASE source, showing longitudinal modes and their suppression

Such ASE sources have been previously generated in Yb-doped fibres at low and high output powers of more than 100W [2.45-48] through different techniques and then extended to Tm-doped fibres [2.44]. High output power ASE sources were recently demonstrated, making use of MOPA configurations in Yb-doped and Tm-doped fibres [2.49, 50].

The light generated by a fibre-based ASE source typically has a high spatial coherence allowing it to be focussed down to a small spot, but low temporal coherence. Therefore, large core or multimode fibres can be used without having any modal interference. This would allow power scaling of ASE sources whilst minimising issues about beam pointing stability or beam quality. Whilst ASE sources seem quite advantageous for amplification in multi-mode fibres compared to laser sources, spectral control of ASE sources is particularly difficult as the previously described technique is based on feedback suppression to frustrate lasing and achieve ASE behaviour. A spectrally-tailored ASE source, compatible with power scaling would be of great interest for many applications but would require being feedback tolerant to allow output spectrum tuning. A novel technique developed recently at the Optoelectronics Research Centre by Jae Daniel and based on cavity dynamics demonstrated ASE operation whilst tolerating feedback and is explained in Section 6.2.1 whilst a new system allowing spectral shaping of an ASE source is detailed.

2.5 Tuning techniques

Different tuning techniques can be used to adjust the output spectrum of a laser, particularly of a Tm-doped fibre laser. Many of the techniques used are based on free-space components for a wide tuning range even

though some tuning is still possible in a fully fibre-based system. Here we describe different architectures allowing tuning of a fibre laser.

2.5.1 Diffraction grating

One of the most popular approaches for tuning the laser output spectrum is the addition of a diffraction grating intra-cavity to select the wavelength to be fed back into the gain medium. Diffraction gratings are dispersive elements based on the wavelength dependent reflection of a periodic structure. The incoming light is dispersed at an angle that is dependent of the grating's period, the wavelength and the incoming angle. The diffraction equation for such a grating is given by:

$$m\lambda = d(\sin\theta_{in} + \sin\theta_{out}) \tag{2.9}$$

Where m in the diffracted order, θ_{in} and θ_{out} the incident and diffracted angles (with the grating normal as a reference) and d the spatial period of the grating used. A diffraction grating can be used in a Littrow configuration that consists of a retroreflective configuration shown in Figure 2.8.

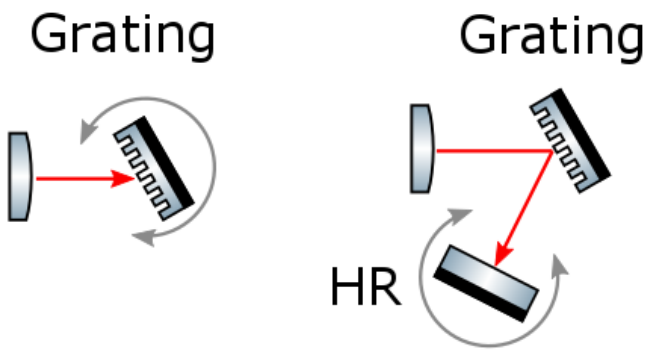

Figure 2.8 Littrow and Littman-Metcalf configuration of a diffraction grating for wavelength tuning in a laser.

Tuning of the output wavelength is then achieved by rotation of the diffraction grating. Such an element can also be used in a 'Littman-Metcalf' configuration (seen in Figure 2.8) where the grating angle is fixed and tuning is achieved by rotation of the feedback mirror. This second configuration leads to better resolution via a double-pass on the grating. The diffraction efficiency of a grating can reach up to 90 % in a Littrow configuration for the designed wavelength and polarisation. Such a tuning method allows quite accurate tuning over a wide range but requires the use of free-space optics with a collimated beam.

2.5.2 Volume Bragg Gratings

Volume Bragg gratings (VBGs) consist of a volume of photo-thermal refractive glass in which a periodic refractive index modulation has been written. These systems can be used in either a reflective or transmissive configuration and can have a reflectivity up to 99.9% due to the long interaction length and large index

modulation, combined with a sub-nm bandwidth that allows relatively narrowband wavelength selection quite easily. The operating wavelength is linked to the grating period by the following equation:

$$\lambda_{VBG} = 2\Delta n\cos\theta \tag{2.10}$$

Where θ is the incident angle relative to the grating normal, n the average refractive index of the medium and Δ the grating period. Tuning is then achieved by coupling the VBG to a mirror and rotating the VBG as shown in Figure 2.9. Much more accurate tuning is often achieved with a VBG than with a regular diffraction grating.

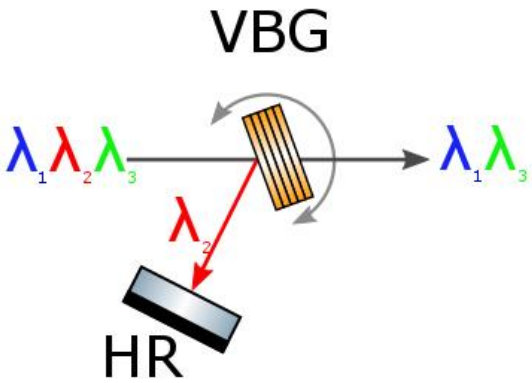

Figure 2.9 Wavelength-selectivity system by using a VBG coupled to a mirror

2.5.3 Fibre Bragg Gratings

Fibre Bragg gratings (FBGs) consist of a periodic index modulation directly written into the core of a fibre, allowing to have an all-fibre system. Reflectivity can be really high (up to 99.9%) with a high wavelength selectivity bandwidth as narrow as tens of picometres. The first order resonance wavelength for a fibre Bragg grating is:

$$\lambda_{FBG} = 2n_{eff}\Delta \tag{2.11}$$

where n_{eff} the effective index of the propagating mode and Δ the grating modulation period. Change of the modulation periods leads to some wavelength flexibility. This can be achieved by temperature control or mechanical constraints such as straining or compressing it. Strain tuning, where the grating is put under tension to increase the Bragg period, is used to shift towards longer wavelength but this can create cracks in the fibre, thus is often considered unreliable. Logically, compression of the grating can also be done to reach shorter wavelength. The compression process is much less susceptible to create microcracks into the fibre core, resulting into a higher reliability than the straining technique. Tuning but straining or compressing a FBG only allows tuning over few nanometers with up to 10nm in best cases which can be limitative depending on the desired application.

2.5.4 Acousto-optic tunable-filter

An Acousto-Optic Tunable-Filter (AOTF) is based on the acousto-optic effect and acts as a controllable bandpass filter which achieves high power handling and rapid tuning without requiring moving part. An acoustic wave is sent into a crystal by the application of a RF signal, its propagation creating an index modulation inside the crystal. A diffraction grating is therefore formed within the medium, deflecting a narrow band of wavelength at a fixed angle (see Figure 2.10). The AOTF has the property to have a diffracted beam angle independent of the desired wavelength, allowing it to be reflected by a static mirror. Wavelength selection is then achieved by changing the RF drive frequency.

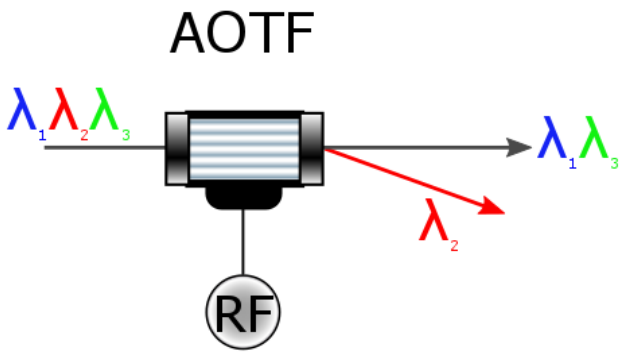

Figure 2.10 Wavelength selection by using an AOTF

As no moving mechanical part is involved in AOTF wavelength-tuning, rapid switching of wavelength can be achieved. Thanks to the crystal technology used similar to high-power handling AOMs for Q-switching, AOTFs are suitable for high power use and achieve high diffraction efficiency coupled with broad wavelength coverage from the crystals transparency. AOTFs achieve a spectral selectivity down to few nm in the near IR light and can be improved through a double-pass. Their main advantages in the tuning speed as no element requires to be realigned during tuning, only the RF signal sent to the AOTF is changed and can be adjusted at high frequency speeds up to MHz.

2.5.5 Fabry-Perot etalon

A Fabry-Perot etalon consists of two plane high reflectivity mirrors perfectly parallel with each other. As the mirrors are parallels, the light circulating in the etalon interferes at each round-trip, allowing wavelength selection as only the wavelengths interfering constructively will be transmitted.

One can define this as a cavity where the round-trip gain is called $\tilde{g}_{rt}$ and is dependent on the light frequency ω. Figure 2.11 shows a schematic of such a cavity.

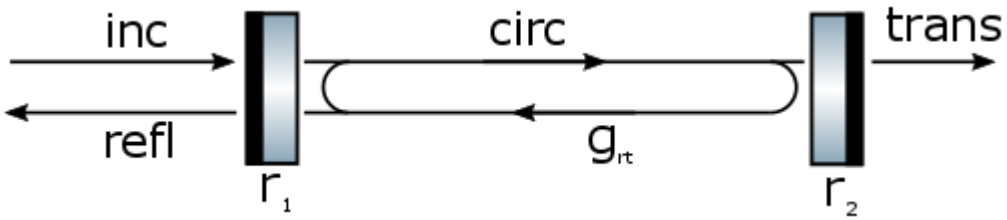

Figure 2.11 Fabry-Perot etalon schematic

In a stable regime:

$$\widetilde{E}_{circ} = jt_1\widetilde{E}_{inc} + \tilde{g}_{rt}(\omega)\widetilde{E}_{circ} \tag{2.12}$$

With

$$\tilde{g}_{rt}(\omega) = r_1 r_2 . \exp(-\alpha_0 p - j\omega p/c) \tag{2.13}$$

Where r_1 and r_2 are the mirrors reflectivity, p the round-trip distance, c the speed of light and α_0 the continuous losses inside the etalon. The round-trip gain always verifies

$$|\tilde{g}_{rt}(\omega)| \leq 1$$

From that, the cavity transmission as a function of light frequency can be deduced [2.51] :

$$\frac{\widetilde{E}_{trans}}{\widetilde{E}_{inc}} = \frac{-t_1 t_2 . \sqrt{\exp\left(-\alpha_0 p - \frac{j\omega p}{c}\right)}}{1-\tilde{g}_{rt}(\omega)} = \frac{-t_1 t_2}{\sqrt{r_1 r_2}} \cdot \frac{\sqrt{\tilde{g}_{rt}(\omega)}}{1-\tilde{g}_{rt}(\omega)} \tag{2.14}$$

Figure 2.12 shows the evolution of $\frac{I_{trans}}{I_{inc}}$ as a function of $\frac{\omega p}{2\pi c}$ obtained by using equation (**2.14**). High transmission is here achieved for wavelengths fitting the criteria $\omega_q = \frac{q2\pi c}{p}$. Transmission of up to 100% can be achieved with the transmission peaks getting sharper and narrower for etalon configurations having high reflectivity mirrors.

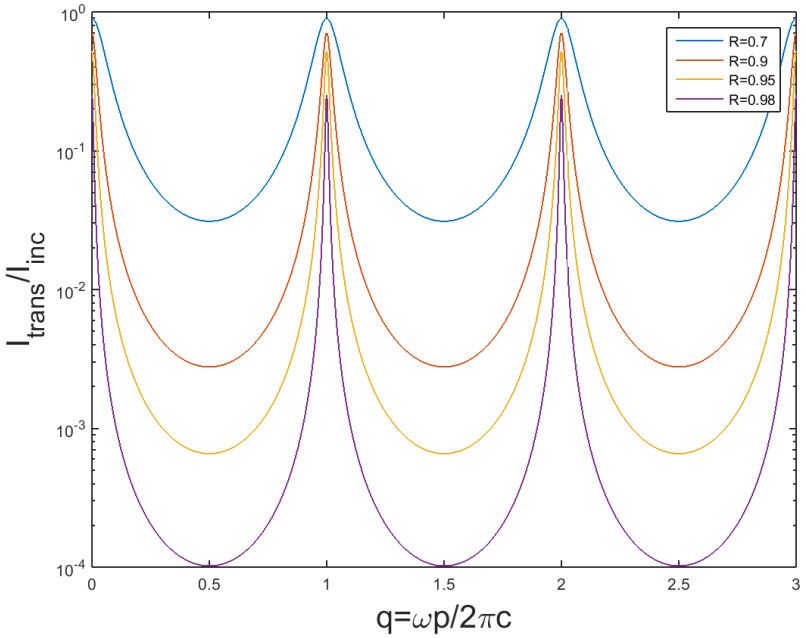

Figure 2.12 Transmission curve of a Fabry-Perot etalon

From that, the cavity reflectivity as a function of light frequency can be calculated with:

$$\frac{\tilde{E}_{refl}}{\tilde{E}_{inc}} = \frac{r_1^2 - \tilde{g}_{rt}(\omega)}{r_1\left(1 - \tilde{g}_{rt}(\omega)\right)} \qquad (2.15)$$

Figure 2.13 describes the evolution of $\frac{I_{refl}}{I_{inc}}$ as a function of $\frac{\omega p}{2\pi c}$ calculated from equation (**2.15**). Low reflection is obtained each time q is an integer. This result fits with what was described earlier in Figure 2.12 as high transmission is achieved when q is an integer.

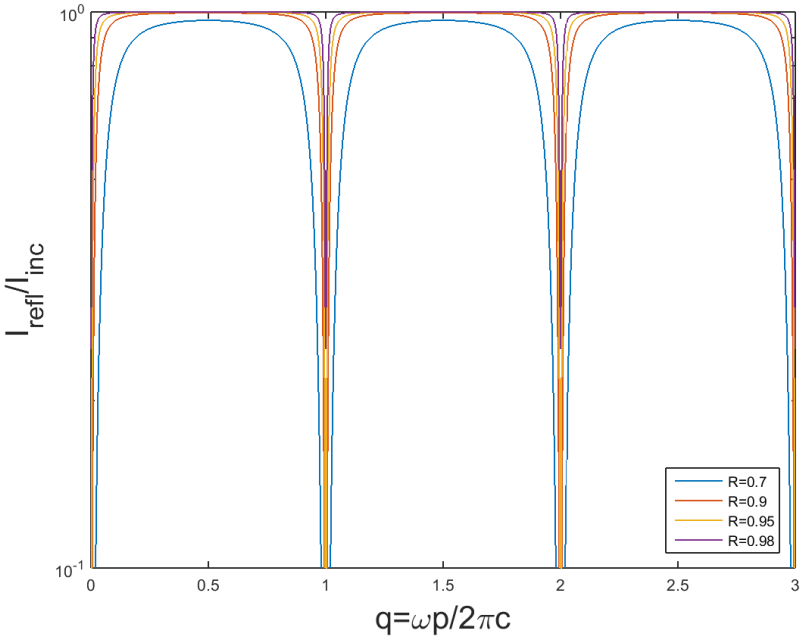

Figure 2.13 Reflectivity of a Fabry-Perot etalon

2.6 Power-scaling considerations

2.6.1 Master oscillator power amplifier principles

The idea behind a Master Oscillator Power Amplifier (MOPA) is to employ a seed source (i.e. the Master Oscillator (MO)) and to inject it into a Power Amplifier (PA) to increase the output power. The main advantage of this configuration compared to a single oscillator is that the seed can be built at relatively low power (compared to after amplification) and, thus, allows an accurate control of its characteristics such as wavelength, bandwidth (FWHM for example) or pulse duration. It can then be amplified to significantly higher power (a gain of between 10 and 30dB is often achievable in fibre amplifiers) without changing the primary characteristics of the output.

This configuration offers the possibility of changing the seed used without having to change the amplification process and is also easier to install as designing a laser with high output power and specific characteristics can be much more difficult than designing the same source a low power and then amplifying it through another device [2.52, 53]. Moreover, with this system most of the thermal heat load will be in the amplifier and therefore easier to deal with.

Amplifiers can be fully fibre-based depending on the setup used, thus allowing to combine seeds and amplifiers easily, each one being built independently from the other. However, the use of such a configuration can be troublesome as any reflected light from the amplifier to the seed could damage it if no isolator is used between the two systems. The amplifier must also be interlocked with the seed, as a rapid stop of the seed without a stop of the amplifier pumping diodes would damage the components. Non-linearities can also occur in the amplifier stage design if not suitable for the planned amplification as a long fibre amplifier will see its non-linear thresholds decrease and this might be problematic (as detailed later on in Section 2.6.2). Such non-linearity thresholds are of particular interest in this thesis, especially the Stimulated Brillouin Scattering threshold, as the focus applied on the generation and amplification of ASE output permit higher non-linear thresholds through signal linewidth increase and the use of multi-core fibres.

2.6.2 Non-linear effects

2.6.2.1 Stimulated Brillouin Scattering

Brillouin scattering occurs due to the χ^3 nonlinearity of a medium when an incident photon is converted into a slightly lower energy photon travelling in the backwards direction (called Stokes wave) and an acoustic phonon corresponding to the energy difference. This phenomenon can be very detrimental to laser operation, especially in single frequency and pulsed operation regimes, potentially leading to damage of the fibre or other optical components as the backwards travelling downward shifted photon can be amplified.

The frequency shift between these two photons is called Brillouin frequency shift and, for a backward Brillouin scattering only, equals:

$$\nu_B = \frac{2n\nu_a}{\lambda} = 8.2\ \text{GHz} \tag{2.16}$$

With n the refractive index, ν_a the acoustic velocity (5700m/s in a silica fibre), and λ the optical wavelength in vacuum. This gives a shift of 0.1nm at 2microns in a silica fibre. The maximum gain coefficient is obtained at ν_B and equals:

$$g_{Bmax} = \frac{\Delta_{\nu_B}}{\Delta_{\nu_B} + \Delta_{\nu_{signal}}} g_b(\nu_B) \tag{2.17}$$

With a bandwidth Δ_{ν_B} of 10MHz and a gain $g_b(\nu_B) = 8.38*10^{-11}\text{m/W}$

Compared to SRS, the SBS gain is strongly dependent on the signal linewidth, a narrow linewidth signal leading to high SBS gain. Moreover, the threshold value for SBS can be expressed as:

$$P_{th}^{SBS} \approx \frac{21A_{eff}}{g_{Bmax} l_{eff}} \tag{2.18}$$

Where A_{eff} is the effective area calculated from the MFD obtained with Marcuse's equation (eq. (**2.4**)), l_{eff} is the effective interaction length of the chosen propagating mode given by $l_{eff} = \frac{1-e^{-\alpha L}}{\alpha}$ with L the fibre length and α the loss (or gain) coefficient of the fibre at the specified wavelength.

In Figure 2.14 we simulate the SBS threshold as a function of the signal linewidth for a fibre having a core radius of 5µm and a length of 2m.

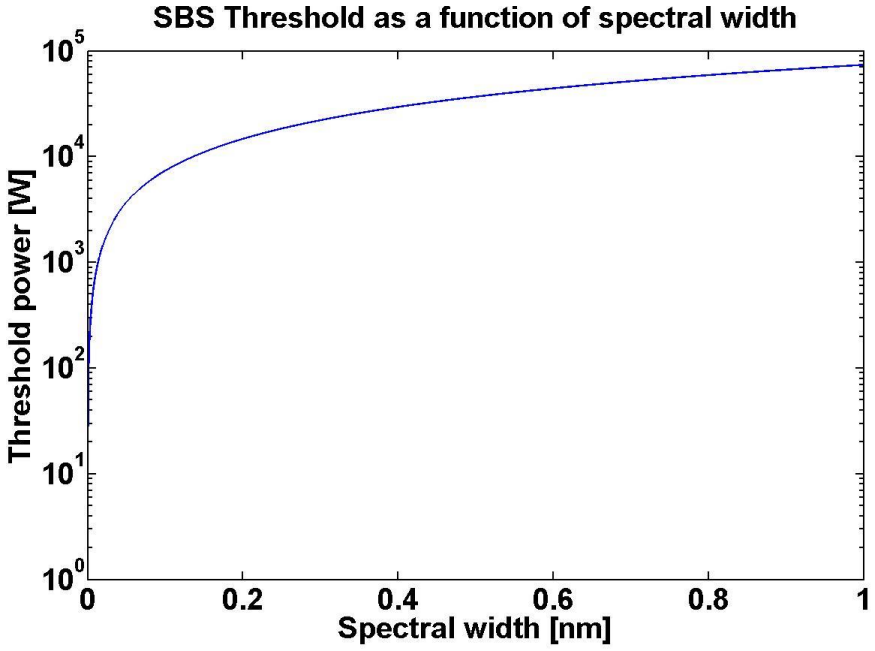

Figure 2.14 SBS threshold as a function of signal spectral width in an amplifier

One can see that for a narrow-linewidth source the SBS threshold can easily be lower than 100W peak power whilst broader spectra would lead to peak power threshold of more than 10kW, making broad sources such as ASE more suitable than laser for high power scaling by increasing the SBS threshold.

The timescale associated with SBS is linked to the acoustic wave build-up time which is in the order of 10ns, thus for pulse widths shorter than this value, the SBS threshold increases significantly, making other non-linear processes such as SRS the main issue. Different approaches are available in fibres to achieve significant power scaling whilst avoiding SBS by increasing SBS threshold through fibre core width fluctuations, thermal gradient or stress gradient along the fibre length broadening the gain bandwidth [2.54-56]. Another solution is to reduce the overlap of acoustic and optical modes by adjusting the acoustic index of the waveguide [2.57].

2.6.2.2 Stimulated Raman Scattering

Stimulated Raman scattering (SRS) comes from the Raman gain. This gain can be observed when sending two laser beams of same polarisation and different wavelengths in a Raman-active medium. The longer wavelength will experience amplification whilst the shorter will be attenuated due to energy transfer. Such a non-linear effect is effectively used in Raman amplifiers and Raman lasers as the gain can be quite high for a Stoke shift frequency dependant on the host, with a value of several THz for fused silica.

For Raman scattering, a pump photon is converted into a lower-energy signal photon (higher wavelength) and a phonon corresponding to the energy difference between these two photons is generated. This process can be seen as similar to SBS with the generated phonon having a much higher energy. This phonon can then be considered to be an optical phonon rather than an acoustic one. At high enough intensity the generated signal photons, called the Stokes wave, can act as pump for further Raman scattering creating a cascading process.

Raman scattering can be detrimental in fibre amplifiers, especially for pulsed amplification as high intensity is reached by the end of the amplification stage. Energy is transferred from the signal wavelength to longer wavelengths where amplification might not occur. Some solutions exist to avoid this problem such as chirped-pulse amplification or the use of special fibre designs to suppress Raman scattering via attenuation of the wavelength-shifted component.

The Raman gain is a function of the frequency shift and is maximal for a shift of +13THz in silica (corresponding to a shift from 2000nm to 2189nm), having a value [2.58]$g_{Rmax} = 10^{-13}\mathrm{m/W(at\ 13\ THz)}$

The Raman threshold is usually evaluated with the following equation [2.59]:

$$P_{th}^{SRS} \approx \frac{16A_{eff}}{g_{Rmax}l_{eff}} \tag{2.19}$$

However, the Raman gain is dependent on the host used and the maximal gain value given above is for silica fibres. Many specific fibres are designed to improve the Raman gain and actively utilise the Raman effect for

reaching otherwise unavailable wavelengths [2.60]. SRS can be exploited in a cascade configuration to achieve more than one down-shift and reach wavelengths further away from the pump wavelength [2.61].

2.6.3 Damage threshold

Damage in the fibre is also one of the main concerns at high power operation, particularly in pulsed regime. The glass fibre can be damaged by light intensity high enough to create ionisation and plasma formation inside the fibre. Theoretical values vary dependent on pulse width and core composition but an approximation can be made for ps to ns pulse widths by calculating the damage threshold of bulk silica illuminated at 1064nm with a maximal peak power P_{max} of [2.53]:

$$P_{max} \approx 1.5\text{kW}.\,\text{ns}^{0.5}/\mu\text{m}^2 \tag{2.20}$$

By multiplying this value by the beam area and dividing by the square root of the pulse width, maximum peak power is deduced. This damage often occurs at the high power output end of the fibre as the damage threshold is linked to peak power and small defect on the output surface might lower this threshold.

The use of endcaps can be used to increase beam size at the end facet, decreasing the beam intensity at the air/glass interface to improve damage threshold. Such endcaps consist in a pure fused silica coreless fibre matched to the active fibre added at the end of the system. Larger endcaps are also possible but require a more sophisticated process than simple splicing of a coreless fibre.

For a diffraction-limited beam, the mode field diameter increases as a function of this endcap length following:

$$\omega(z) \approx \frac{z.\,NA}{n_{clad}} + r_{core} \tag{2.21}$$

With z the endcap length. This length is often chosen so that the MFD equals half of the end-cap radius in order to also minimise feedback.

2.7 References

2.1. Hanna, D.C., et al., *Efficient and Tunable Operation of a Tm-Doped Fiber Laser.* Optics Communications, 1990. **75**(3-4): pp. 283-286.

2.2. Jackson, S.D. and T.A. King, *Theoretical modeling of Tm-doped silica fiber lasers.* Journal of Lightwave Technology, 1999. **17**(5): pp. 948-956.

2.3. Moulton, P.F., et al., *Tm-Doped Fiber Lasers: Fundamentals and Power Scaling.* Ieee Journal of Selected Topics in Quantum Electronics, 2009. **15**(1): pp. 85-92.

2.4. T. Ehrenreich, et al., *1-kW, all-glass Tm:fiber laser*, in *Fiber Lasers VII: Technology, Systems, and Applications (2010) (Session 16: Late breaking news).* 2010.

2.5. Mingareev, I., et al., *Welding of polymers using a 2 µm thulium fiber laser.* Optics and Laser Technology, 2012. **44**(7): pp. 2095-2099.

2.6. Hemming, A., et al., *99 W mid-IR operation of a ZGP OPO at 25% duty cycle.* Optics Express, 2013. **21**(8): pp. 10062-10069.

2.7. Budni, P.A., et al., *Efficient mid-infrared laser using 1.9-µm-pumped Ho:YAG and ZnGeP2 optical parametric oscillators.* Journal of the Optical Society of America B, 2000. **17**(5): pp. 723-728.

2.8. Leunig, A., et al., *Ho : YAG laser treatment of hyperplastic inferior nasal turbinates.* Laryngoscope, 1999. **109**(10): pp. 1690-1695.

2.9. Johnson, D.E., *Use of the Holmium-Yag (Ho Yag) Laser for Treatment of Superficial Bladder-Carcinoma.* Lasers in Surgery and Medicine, 1994. **14**(3): pp. 213-218.

2.10. Creeden, D., et al., *Resonantly pumped Tm-doped fiber laser with > 90% slope efficiency.* Optics Letters, 2014. **39**(3): pp. 470-473.

2.11. Ji, J.H., et al., *Minimize quantum-defect heating in thulium-doped silica fiber amplifiers by tandem-pumping.* 2012 Photonics Global Conference (Pgc), 2012.

2.12. Mond, M., et al., *1.9µm and 2.0µm laser diode pumping of Cr2+: ZnSe and Cr2+: CdMnTe.* Optics Letters, 2002. **27**(12): pp. 1034-1036.

2.13. Yao, B.Q., et al., *Holmium Laser In-Band Pumped by a Thulium Laser in the Same Host of YAlO(3).* Laser Physics, 2008. **18**(12): p. 1501-1504.

2.14. Wikipedia. *Maximum permissible exposure: IEC-60825-1*. Available from: https://en.wikipedia.org/wiki/Laser_safety#Regulations.

2.15. Li, Z., et al., *Thulium-doped fiber amplifier for optical communications at 2µm.* Optics Express, 2013. **21**(8): pp. 9289-9297.

2.16. *Gemnini observatory*. Available from: https://www.gemini.edu/sciops/telescopes-and-sites/observing-condition-constraints/ir-transmission-spectra.

2.17. J. Flaud, A.B., and N. Husson, *REFERENCES and SOURCES for HITRAN.* 2013(0, 4058–4097).

2.18. Cariou, J.P., B. Augere, and M. Valla, *Laser source requirements for coherent lidars based on fiber technology.* Comptes Rendus Physique, 2006. **7**(2): pp. 213-223.

2.19. Gagliardi, G., et al., *High-precision determination of the (CO2)-C-13/(CO2)-C-12 isotope ratio using a portable 2.008μm diode-laser spectrometer.* Applied Physics B-Lasers and Optics, 2003. **77**(1): pp. 119-124.

2.20. Kadwani, P., et al., *Atmospheric absorption spectroscopy using Tm: fiber sources around 2 microns.* Atmospheric and Oceanic Propagation of Electromagnetic Waves V, 2011. **7924**.

2.21. Kadwani, P., et al., *Atmospheric gas detection using broadband mid-IR thulium fiber-based sources.* Laser Technology for Defense and Security Vii, 2011. **8039**.

2.22. McComb, T.S., et al., *Atmospheric Transmission Testing Using a Portable, Tunable, High Power Thulium Fiber Laser System.* 2010 Conference on Lasers and Electro-Optics (Cleo) and Quantum Electronics and Laser Science Conference (Qels), 2010.

2.23. Rocco, A., et al., *A diode-laser-based spectrometer for in-situ measurements of volcanic gases.* Applied Physics B-Lasers and Optics, 2004. **78**(2): pp. 235-240.

2.24. Sonnenfroh, D.M. and M.G. Allen, *Absorption measurements of the second overtone band of NO in ambient and combustion gases with a 1.8μm room-temperature diode laser.* Applied Optics, 1997. **36**(30): pp. 7970-7977.

2.25. Hale, G.M. and M.R. Querry, *Optical-Constants of Water in 200nm to 200μm Wavelength Region.* Applied Optics, 1973. **12**(3): pp. 555-563.

2.26. Alexander, V.V., et al., *Photothermolysis of Sebaceous Glands in Human Skin Ex Vivo with a 1,708 nm Raman Fiber Laser and Contact Cooling.* Lasers in Surgery and Medicine, 2011. **43**(6): pp. 470-480.

2.27. Jelinkova, H., et al., *Diode-pumped Tm : YAP laser for eye microsurgery - art. no. 68712N.* Solid State Lasers Xvii: Technology and Devices, 2008. **6871**: p. N8712.

2.28. Scott, N.J., C.M. Cilip, and N.M. Fried, *Thulium Fiber Laser Ablation of Urinary Stones Through Small-Core Optical Fibers.* Ieee Journal of Selected Topics in Quantum Electronics, 2009. **15**(2): pp. 435-440.

2.29. Theisen, D., et al., *Cw high power IR-laser at 2μm for minimally invasive surgery.* Therapeutic Laser Applications and Laser-Tissue Interactions, 2003. **5142**: pp. 96-100.

2.30. Agger, S.D. and J.H. Povlsen, *Emission and absorption cross section of thulium doped silica fibers.* Optics Express, 2006. **14**(1): pp. 50-57.

2.31. Daniel, J.M.O., *WAVELENGTH SELECTION AND TRANSVERSE MODE CONTROL IN HIGH POWER FIBRE LASERS*, in *Faculty of Physical Sciences and Engineering, Optoelectronics Research Centre*. 2013, University of Southampton.

2.32. Li, J.F., et al., *Wide wavelength selectable all-fiber thulium doped fiber laser between 1925 nm and 2200 nm.* Optics Express, 2014. **22**(5): pp. 5387-5399.

2.33. Scott Christensen, G.F., and Bryce Samson, *Developments in thulium-doped fiber lasers offer higher powers.* SPIE, 2008.

2.34. Jackson, S.D., *Cross relaxation and energy transfer upconversion processes relevant to the functioning of 2µm Tm3+-doped silica fibre lasers.* Optics Communications, 2004. **230**(1-3): pp. 197-203.

2.35. Jackson, S.D. and S. Mossman, *Efficiency dependence on the Tm3+ and Al3+ concentrations for Tm3+-doped silica double-clad fiber lasers.* Applied Optics, 2003. **42**(15): pp. 2702-2707.

2.36. Kalaycioglu, H., A. Sennaroglu, and A. Kurt, *Influence of doping concentration on the power performance of diode-pumped continuous-wave Tm3+: YA1O(3) lasers.* Ieee Journal of Selected Topics in Quantum Electronics, 2005. **11**(3): pp. 667-673.

2.37. Goodno, G.D., L.D. Book, and J.E. Rothenberg, *Low-phase-noise, single-frequency, single-mode 608 W thulium fiber amplifier.* Optics Letters, 2009. **34**(8): pp. 1204-1206.

2.38. Jackson, S.D., et al., *High-power 83 W holmium-doped silica fiber laser operating with high beam quality.* Optics Letters, 2007. **32**(3): pp. 241-243.

2.39. Simakov, N., et al., *A cladding-pumped, tunable holmium doped fiber laser.* Optics Express, 2013. **21**(23): pp. 28415-28422.

2.40. Hemming, A., et al., *High power, narrow bandwidth and broadly tunable Tm3+, Ho3+-co-doped aluminosilicate glass fibre laser.* Electronics Letters, 2010. **46**(24): pp. 1617-1618.

2.41. Walsh, B.M., *Review of Tm and Ho materials; spectroscopy and lasers.* Laser Physics, 2009. **19**(4): pp. 855-866.

2.42. Gloge, D., *Weakly Guiding Fibers.* Applied Optics, 1971. **10**(10): p. 2252.

2.43. Marcuse, D., *Loss Analysis of Single-Mode Fiber Splices.* Bell System Technical Journal, 1977. **56**(5): pp. 703-718.

2.44. Shen, D.Y., et al., *Broadband Tm-doped superfluorescent fiber source with 11 W single-ended output power.* Optics Express, 2008. **16**(15): pp. 11021-11026.

2.45. Goldberg, L., et al., *High-power superfluorescent source with a side-pumped Yb-doped double-cladding fiber.* Optics Letters, 1998. **23**(13): pp. 1037-1039.

2.46. Kong, L.F., et al., *2W Yb-doped double-clad fiber superfluorescent source with 42 nm 3 dB bandwidth.* Optics and Laser Technology, 2005. **37**(8): pp. 597-600.

2.47. Wang, P., J.K. Sahu, and W. Clarkson, *High Power Single-ended Yb-doped Fiber ASE Source.* 2007 Conference on Lasers & Electro-Optics/Quantum Electronics and Laser Science Conference (Cleo/Qels 2007), Vols 1-5, 2007: pp. 1632-1633.

2.48. Wang, P., J.K. Sahu, and W.A. Clarkson, *110 W double-ended ytterbium-doped fiber superfluorescent source with M-2=1.6.* Optics Letters, 2006. **31**(21): pp. 3116-3118.

2.49. Liu, J. and P. Wang, *High-Power Broadband Thulium-Doped All-Fiber Superfluorescent Source at 2μm.* Ieee Photonics Technology Letters, 2013. **25**(3): pp. 242-245.

2.50. Schmidt, O., et al., *High power narrow-band fiber-based ASE source.* Optics Express, 2011. **19**(5): pp. 4421-4427.

2.51. Siegman, A.E., *Lasers*. Mill Valley, Calif.: University Science Books.

2.52. Jeong, Y., et al., *Power scaling of single-frequency ytterbium-doped fiber master-oscillator power-amplifier sources up to 500 W.* Ieee Journal of Selected Topics in Quantum Electronics, 2007. **13**(3): pp. 546-551.

2.53. Richardson, D.J., J. Nilsson, and W.A. Clarkson, *High power fiber lasers: current status and future perspectives.* Journal of the Optical Society of America B-Optical Physics, 2010. **27**(11): pp. B63-B92.

2.54. Hansryd, J., et al., *Increase of the SBS threshold in a short highly nonlinear fiber by applying a temperature distribution.* Journal of Lightwave Technology, 2001. **19**(11): pp. 1691-1697.

2.55. Kerttula, J., et al., *Tapered fiber amplifier with high gain and output power.* Laser Physics, 2012. **22**(11): pp. 1734-1738.

2.56. CANAT G. , L.L., LE GOUËT J. , FLEURY D., *OPTIC FIBER AMPLIFIER HAVING A HIGH BRILLOUIN THRESHOLD AND METHOD FOR MAKING SUCH AN AMPLIFIER*. 2014, OFFICE NATIONAL D'ETUDES ET DE RECHERCHES AÉROSPATIALES - ONERA.

2.57. Li, M.J., et al., *Al/Ge co-doped large mode area fiber with high SBS threshold.* Optics Express, 2007. **15**(13): pp. 8290-8299.

2.58. Stolen, R.H., A.R. Tynes, and E.P. Ippen, *Raman Oscillation in Glass Optical Waveguide.* Applied Physics Letters, 1972. **20**(2): p. 62-.

2.59. Smith, R.G., *Optical Power Handling Capacity of Low Loss Optical Fibers as Determined by Stimulated Raman and Brillouin-Scattering.* Applied Optics, 1972. **11**(11): p. 2489.

2.60. Bromage, J., *Raman amplification for fiber communications systems.* Journal of Lightwave Technology, 2004. **22**(1): pp. 79-93.

2.61. Supradeepa, V.R. and J.W. Nicholson, *Power scaling of high-efficiency 1.5µm cascaded Raman fiber lasers.* Optics Letters, 2013. **38**(14): pp. 2538-2541.

2.62. N. M. Fried, *"Thulium fiber laser lithotripsy: An in vitro analysis of stone fragmentation using a modulated 110 - watt Thulium fiber laser at 1.94 µm"*, Lasers in surgery and medicine, vol. 37, no. 1, pp. 53-58, 2005.

2.63. Passacantilli, E; et al., Assessment of the utility of the 2-µm thulium laser in surgical removal of intracranial meningiomas,LASERS IN SURGERY AND MEDICINE , 2013

2.64. Sanjay Kolte, et al., *Thulium laser coagulation for venous malformations of glans penis*, Asian Journal of Urology, Volume 3, Issue 2, 2016, pp 110-111

2.65. Batay, LE, et al., *Laser coagulation of tissues by 1,6 µm and 2 µm laser radiation*, INTERNATIONAL CONFERENCE ON LASERS, APPLICATIONS, AND TECHNOLOGIES 2007: LASER TECHNOLOGIES FOR MEDICINE, Volume 6734, 2007

Chapter 3. Localised fibre processing for improved pump absorption

3.1 Introduction

Good beam quality is required in many applications, such as material processing, and can easily be achieved by the use of doped-cores with a low V-number, thus only supporting the fundamental mode. Cladding pumping schemes based on double-clad fibre design offer the possibility of high beam quality whilst using low brightness, high power pump diodes. In such configurations, the multi-mode pump light propagates in the inner cladding while the laser light is generated and confined to the doped core.

In cladding-pumping architectures, each pump mode propagates differently, having a different overlap with the doped-core where absorption occurs. Therefore, mode scrambling is needed to redistribute the energy between modes in order to achieve high overall pump absorption efficiency. Many ways of improving fibre inner-cladding geometry to increase pump absorption in double-clad rare-earth doped optical fibres have been studied [3.1-5] ; mode scrambling is commonly done by using non-circular cladding geometries that break the circular symmetry and/or offset cores. This is a robust method for pump scrambling resulting in significant improvement of pump absorption with geometries such as D-shaped and octagonal (or quasi-octagonal). Some theoretical studies have shown significant improvement in pump absorption with non-circular fibre cladding shapes consisting of many non-planar surfaces [3.6]. These schemes are based on a continuous mode scrambling over the entire fibre length but lead to fibres with a non-circular geometry and possibly off-centred cores making cleaving and splicing to conventional circular fibres for integration rather challenging.

Splicing of two fibres together, usually to link passive and active ones, require both fibre cores to be perfectly aligned with a micrometric precision for single-mode fibres to avoid losses. Current splicers are often based on two side-view cameras aligning the fibres compared to each other, leading to the possibility of high quality reliable splicing by cladding alignment only for circular fibres possessing perfect circular symmetry and a centred core. However, exotic fibre shapes cannot be spliced by passive alignment and require active alignment coupled with possible rotation of the fibres to ensure both core and cladding alignment. Active alignment consists in injection of light in the first fibre core from a superluminescent LED (SLED) and detection of the light transmitted in the second fibre core. SLED are quite useful due to their highly stable output power reaching mW levels and their temporally incoherent output. The splicer then automatically adjusts the fibre's position to either maximise or minimise transmission, i.e. core alignment, depending on the active core composition. This method requires the use of a power metre compatible with the splicer used as well as a cladding stripper on each fibre to ensure that no light remains in the cladding that could otherwise adversely impact on the alignment process. Due to the added complexity and difficulty in achieving repeatability, off-centred core fibres and non-circular active fibres are often avoided in integrated systems where mounting speed and reliability are often the most important factors. Thus, circular fibre geometries are often desirable for integration purposes with fibreised

components compared to non-circular ones even though lower pump absorption is achieved for a given length of fibre.

Here we describe a novel way of improving pump absorption in circular optical fibres by localised laser processing of the fibre, creating point mode scramblers periodically distributed along the fibre. These processed points act to adiabatically change the fibre shape from circular to D-shape. This method offers the benefit of obtaining an active fibre alternating between circular cladding zones necessary for reliable efficient splicing and D-shaped areas required for cladding mode scrambling of the pump, leading to higher pump absorption. Such a fibre would benefit from the advantages of non-circular fibres whilst maintaining a mostly circular fibre cladding which allows easy cleaving and splicing by avoiding the need for active alignment and rotation of the fibres.

3.2 Background

3.2.1 Current fibre geometries

Fibre shapes are evolving towards more exotic forms [3.2, 3] for improved pump absorption such as quasi-circular fibre geometries (D-shaped or octagonal). Figure 3.1 shows three common cladding shapes that are: circular, octagon and D-shape, and ray tracing demonstrating one of the advantages of non-circular fibre claddings. By partly breaking the cladding symmetry, rays propagating inside a D-shaped or octagonal cladding have a higher chance of crossing the doped core and being absorbed, participating in efficient laser operation. Many parameters on D-shape fibres are available such as the D-shape percentage (ratio of smallest over highest cladding diameter in a cross-section) and the core eccentricity [3.4, 5] to improve pump absorption but each modification from a circular geometry leads to higher splicing difficulties.

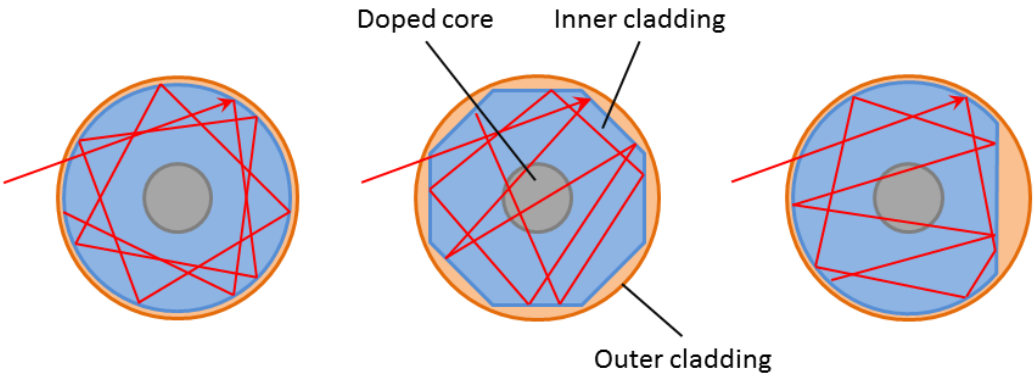

Figure 3.1 Common cladding geometries and their ray tracing showing core interaction

3.2.2 Current fabrication processes

Optical fibres are manufactured by pulling a preform into a fibre where the preform is a large scale version of the fibre. The glass is heated in a furnace up to its softening point and then pulled at the right speed to achieve

the desired cladding diameter. During this softening process, preform shape and core-to-cladding area ratio are maintained, thus, the targeted fibre geometry is usually included in the preform design.

3.2.2.1 Preform milling

To create a preform, doped glass is deposited in the inside of a large tube of passive glass via the Modified Chemical Vapour Deposition (MCVD) technique and then collapsed, obtaining a circular preform. To generate D-shaped fibres (or quasi-octagonal) the circular preform obtained after collapse is milled on one or more sides over its entire length. This milling is achieved by using diamond turning or ultrasonic techniques which both lead to an opaque surface, due to the relatively high roughness. Flame-polishing is then commonly used to remedy to this issue before pulling the fibre. This process has the advantage of being quite straightforward but can be quite limiting. Milling of a preform can lead to damage, rendering the entire preform useless, whilst the flame polishing adds impurities which can be problematic depending on the future use. Moreover, more complex shapes (e.g. concave surfaces) cannot be achieved via this process. Moreover, milling requires considerable care and the entire process is rather time consuming.

3.2.2.2 Laser processing of preforms

A new processing method was recently developed at the ORC based on the use of a CO_2 laser [3.7]. Fused silica has a short absorption depth of few microns (around 10µm) at the 10.6µm wavelength, which makes CO_2 lasers a good solution to process glass. The laser is used in the pulsed regime to ablate glass on the preform surface and the preform is put on computer-controlled stages, allowing the system to shape the preform. This solution has many advantages compared to the more classical approach of preform milling described previously. Firstly, as the processing is computer controlled, algorithms are used to determine the area needing processing to reach the desired shape. Secondly, due to the use of a contactless optical process for shaping, more complex shapes such as concave and convex surfaces can easily be obtained. This solution also offers high surface quality, avoiding the need for a fire-polishing step before the fibre drawing. Moreover, this method heavily reduces the time-scale for preform machining; octagonalisation of a 180mm preform was achieved in less than 90min compared to 2-3 days with classical milling techniques.

This new processing method would allow more efficient cladding shapes to improve pump scrambling; theoretical work was carried out by J. J. Morehead (unpublished) on cladding geometries with high number of surfaces and an optimised cladding geometry with 16 slightly concave faces was proposed for high pump absorption. Such geometry is quite close to circular compared to the commonly used D-shape and octagon ones, potentially offering easier splicing and lower losses. However, until recently, no method of fabrication was available to manufacture fibres or preforms with concave surfaces.

3.3 New processing concept

Light from a highly multimode 6W pump diode with a core diameter of 105µm and NA of 0.22 in a 125µm cladding diameter at 793nm from BWT was injected into the cladding of an in-house fabricated 10/200µm circular thulium fibre with a 3.5wt% doping concentration through the use of a 6+1:1 combiner. The pump diode

used here had a NA of 0.15 whilst the active fibre inner-cladding had a NA of 0.46. A cut-back measurement was performed to assess pump absorption evolution over the fibre length. The active fibre had a starting length of 1m and was kept straight to avoid any uncontrolled mode scrambling and losses from fibre bends. This cut-back measurement consists in assessing the pump power remaining for a defined length of active fibre, deducing the pump absorption coefficient. The active fibre is then cut of few centimeters and measurement is redone, leading to a curve of pump absorption in this fibre as a function of fibre length.

Figure 3.2 shows the evolution of pump absorption as a function of fibre length during cut-back; two gradients are clearly visible, a high gradient of 2dB/m over the first 30 centimeters followed by a lower one of 0.75dB/m once the modes overlapping well with the core are depleted and only the low absorption modes remain. For typical fibre lasers, a high overall pump absorption (> 10dB) is required, leading to the need for a rather long length of fibre (>13 m) in this case. Such long device lengths are quite problematic as they increase the risk of non-linear effects occurring by decreasing their thresholds (CF Chapter 2) and therefore limiting maximum output achievable. Core propagation and reabsorption losses also increase with device length, forbidding emission towards short wavelengths of the dopant emission band. Fibre lasers based on such fibres require short device length for low loss/high non-linear threshold/high efficiency operation but would have a low electrical-to-optical conversion due to the small amount of pump power absorbed.

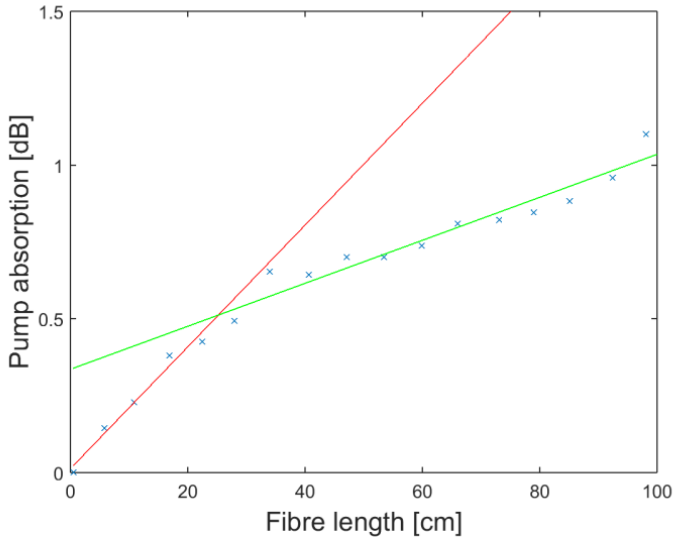

Figure 3.2 Pump absorption evolution in a circular fibre obtained by a cut-back measurement

Mode scrambling is therefore required to achieve higher and more uniform pump absorption per unit length in a desired fibre. This can be realised to some extent by bending/coiling/twisting of the fibre but leads to significant bend-induced losses in low NA large mode area fibres in order to reach satisfying levels of mode scrambling. A uniform pump absorption at a rate of 2dB/m would decrease the fibre length required from 13m to a mere 5m, decreasing the core propagation loss and reabsorption loss. This would in turn offer related advantages such as permitting greater wavelength flexibility towards short wavelengths and higher nonlinear limits.

Here we propose a new way to improve pump absorption in a circular fibre by periodic laser machining of its cladding to create Localised Mode Scramblers (LMSs). This process involves ablation of small sections of the inner-cladding by laser pulses from a CO_2 laser to create short D-shape regions periodically over the fibre length to facilitate mode scrambling at regular intervals whilst keeping an overall circular cladding shape as necessary for ease of splicing.

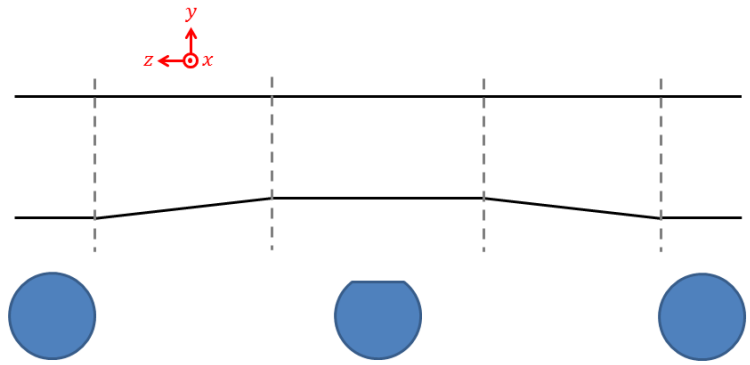

Figure 3.3 Schematic of an LMS along a fibre and fibre profile at different positions

An LMS consists of a D-shape zone surrounded by two transition zones from circular to D-shape and reverse. Figure 3.3 shows a conceptual schematic of a fibre with a LMS and its cross-section at different positions. The transitions zone lengths are to be chosen in order to be adiabatic.

The repetition distance required to maximise pump absorption whilst having the minimum number of LMSs over a selected length of fibre is determined from Figure 3.2. The optimum distance would be when the absorption curve starts to separate from its initial gradient. For the thulium fibre shown here, an optimal repetition distance would be every 25cm.

3.4 Experimental work

3.4.1 First demonstration of cladding shaping utilising a CO_2 laser

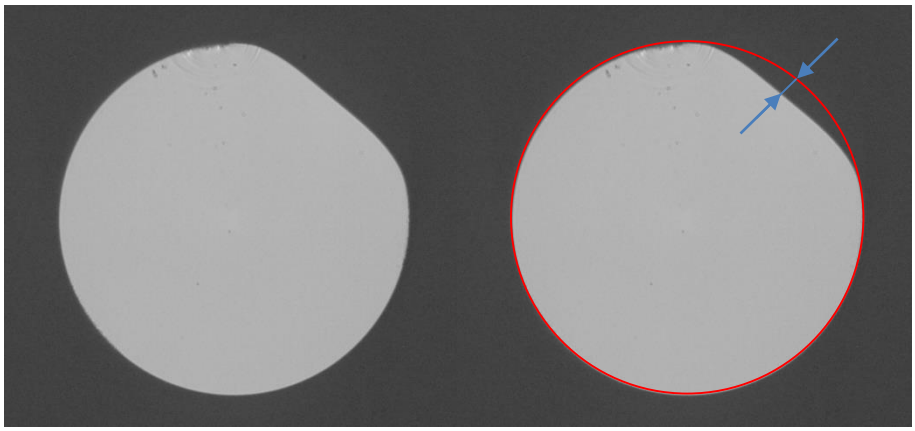

Figure 3.4 Cross-section picture of a 15µm deep LMS in a 200µm coreless fibre

The first demonstration of cladding shaping of a circular fibre cladding into D-shape by the process described earlier based on a CO_2 laser was achieved on a coreless 200µm pure silica fibre. Figure 3.4 shows the cross-section of this coreless fibre after processing in the centre of the created LMS and a D-shaped profile is observed. Control of the processing depth and thus of the D-shape percentage is achieved by modulation of the pulses length. The pulses length was increased to realise deeper D-shapes and Figure 3.5 shows a cross-section of LMS created with a maximum depth of 25µm in a 200µm coreless silica fibre.

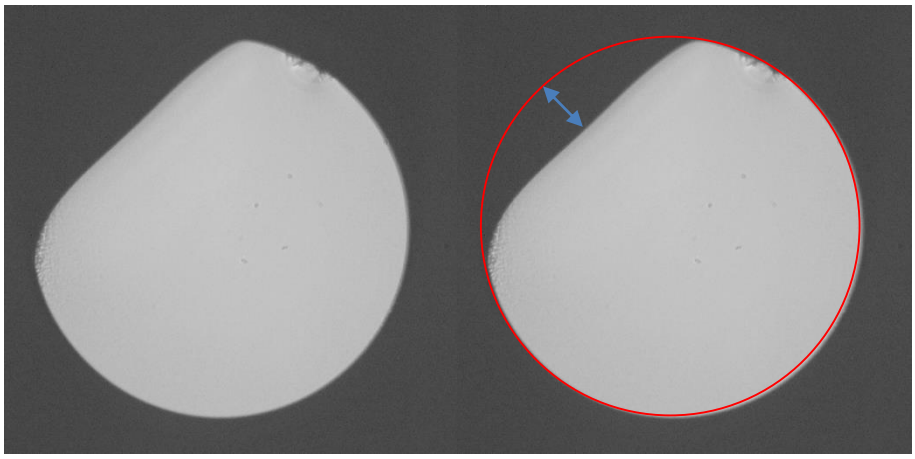

Figure 3.5 Cross-section picture of a 25µm deep LMS in a 200µm coreless fibre

3.4.2 Fabrication

The localised mode scramblers were created on a polymer coated circular silica-host fibre fabricated in-house and thulium doped at 3.5wt%. This fibre had a 10µm core diameter and a 200µm inner-cladding diameter with a core/cladding NA of 0.17/0.46. Processing of the fibre to create these LMSs required stripping of the polymer coating over small sections via the use of a hot-stripper instead of a more conventional three-hole fibre stripper to decrease the risk of breakage during coating removal. The localised mode scramblers were then created in the fibre by laser processing of the cladding via the use of a focused pulsed 100W CO_2 laser. The fibre was moved back from the horizontal focus point to a position where the beam expanded to a beam diameter of 1mm vertically by 200µm horizontally. The fibre was mounted on a vertical translation stage to allow fabrication of long LMSs with a multi-pulse process. The translation stage moved at a continuous speed of 100µm/s whilst the CO_2 laser was fired at a repetition rate of 50Hz to achieve low average thermal loading of the fibre leading to each consecutive pulse hitting the fibre after a displacement step of 2µm. Figure 3.6 shows the set-up used to process the fibre in order to create a LMS containing two clamps holding the fibre mounted on a vertical translation stage while being positioned a few millimetres away from the laser focus point. Single pulse ablation of the fibre cladding was not deemed as a viable solution as this process created non-adiabatic LMSs from the short transition lengths created. Moreover, a non-smooth fibre profile was created due to slight variation of the CO_2 laser profile.

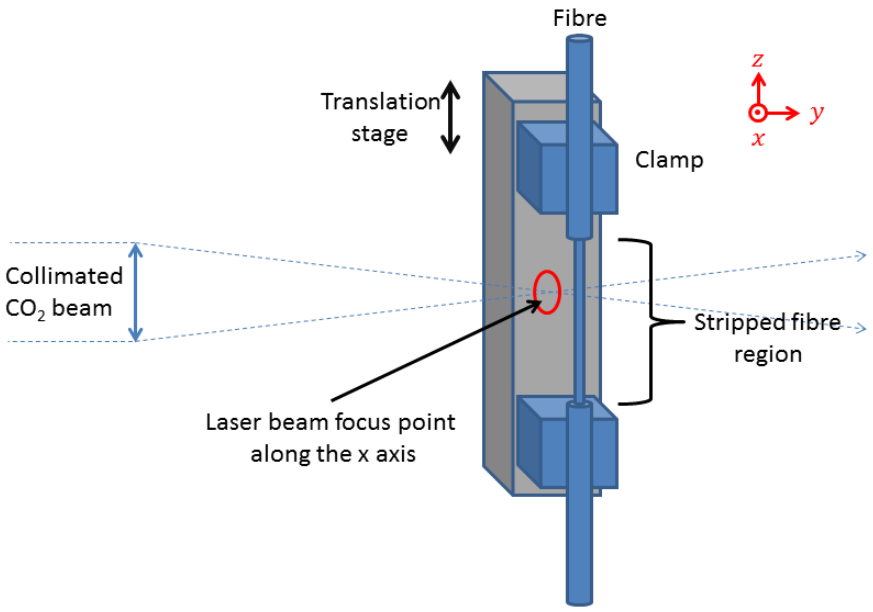

Figure 3.6 Fabrication system based on a CO_2 laser and a translation stage

Control of the laser pulse length allowed precise control of the ablation depth of the cladding. The pulse length was therefore ramped to control the LMS transition length. The laser ramping period was adjusted in order for the LMS's transition length to achieve an adiabatic behaviour, avoiding losses by having a sufficient transition length. Here, this was carried out by a pulse length ramping over 20 seconds corresponding to a 2mm length of fibre, starting below the ablation threshold at 40µs up to a pulse length of 65µs. The transition section created had a length of more than 1.5mm with a maximum depth of 15µm, corresponding to a tapering angle of 10mrad and a decrease in diameter from 200µm to 185µm, corresponding to a 8% D-shape of the fibre. This transition zone was made quite long to ensure adiabatic behaviour. No optimisation was made on this transition length to achieve adiabatic behaviour whilst reducing LMS length transition zone to the minimum.

To avoid pump light escaping from the cladding in the uncoated regions of the fibre, a small mount was designed and fabricated via 3D-printing to keep these sections suspended in air, whilst avoiding contamination. Recoating of the LMSs with low index polymer was not pursued as this would have incurred additional complexity and was not considered to be necessary for this proof-of-principle study.

3.4.3 Design parameters

To create these localised mode scramblers, few key parameters are available shown in Figure 3.7. The first one consists in the repetition distance D which can easily be deduced through a cut-back measurement (see Figure 3.2) whilst the others depend on the shape of the processed area.

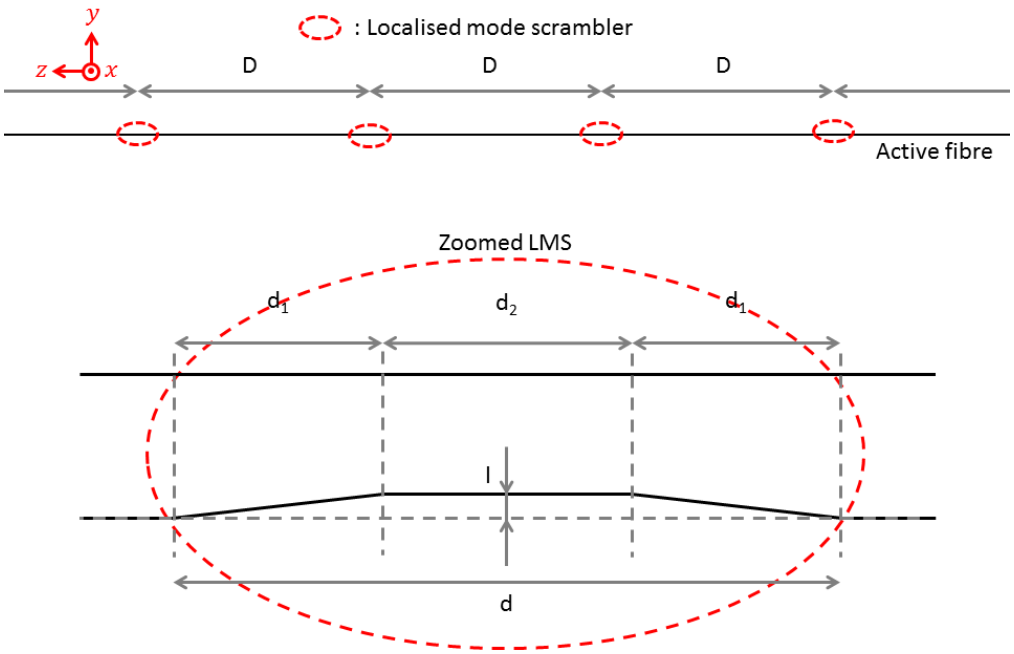

Figure 3.7 Design parameters for localised mode scramblers

The LMSs profile can be customised to achieve the most efficient mode scrambling of pump light whilst minimising propagation losses. Figure 3.7 shows the profile a LMS which can be divided into three parts: a transition zone from circular to D-shape, a D-shape zone and a transition zone from D-shape back to circular. The length d_1 of the transition zones can be adjusted to minimise losses whilst the D-shape zone length d_2 and its depth l (D-shape percentage) will modify the mode scrambling efficiency. Both transition zones will have the same length to achieve low losses in both directions as required for use in a linear laser cavity. All these parameters of the LMS's profile are adjusted by variation of the CO_2 laser pulses length, peak power and repetition rates. The pulse energy combined with the repetition rate will determine the depth of the LMS whilst the ramping and total process duration will adjust the LMS tapering angle and its total length.

3.4.4 Glass re-deposition

Slight specks of dirt were observed on the created LMSs; these are due to re-deposition of the ablated glass during the fabrication process. This unwanted phenomenon creates high losses along the LMS and needs to be avoided, especially as an active fibre will contain multiple LMSs (up to tens of them). Figure 3.8 shows the current disposal method of ablated glass by using a high ventilation system, vacuuming the ablated glass particles. Ablation of the glass leads to re-deposition of the vaporised particles higher than the processing point, thus this vacuuming system is combined with fibre processing from bottom to top. This way, any re-deposited material is re-ablated with the next pulses and removed by the exhaust.

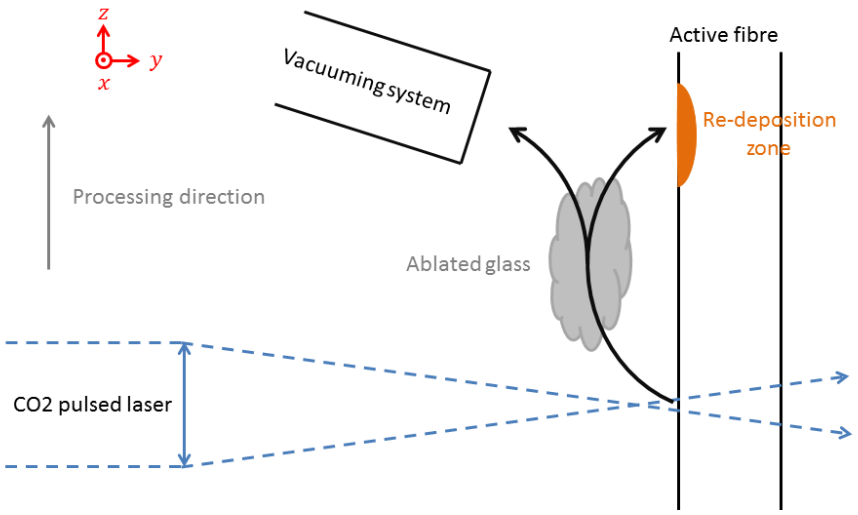

Figure 3.8 Vacuum system and processing procedure to avoid glass re-deposition during LMS fabrication

Figure 3.9 shows a side view along the Z axis of an entire LMS where almost no re-deposition is observed. As a comparison, a failed LMS is shown in Figure 3.10 where high re-deposition occurred as the LMS was processed from top to bottom instead of bottom to top. Both LMSs pictures shown on Figure 3.9 and Figure 3.10 have been vertically scaled (Y axis) by 300% for better visibility.

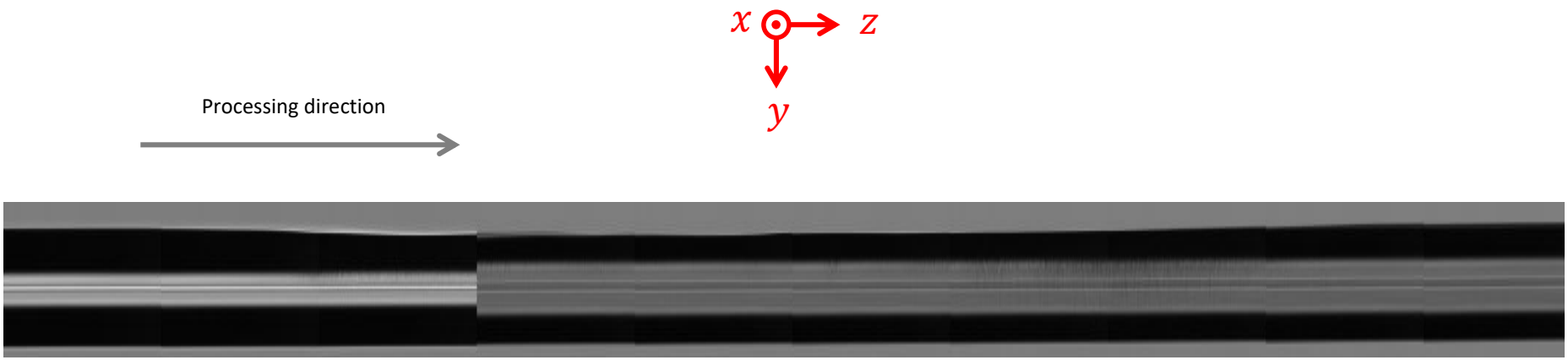

Figure 3.9 Lateral view of a 7mm-long LMS with low re-deposition

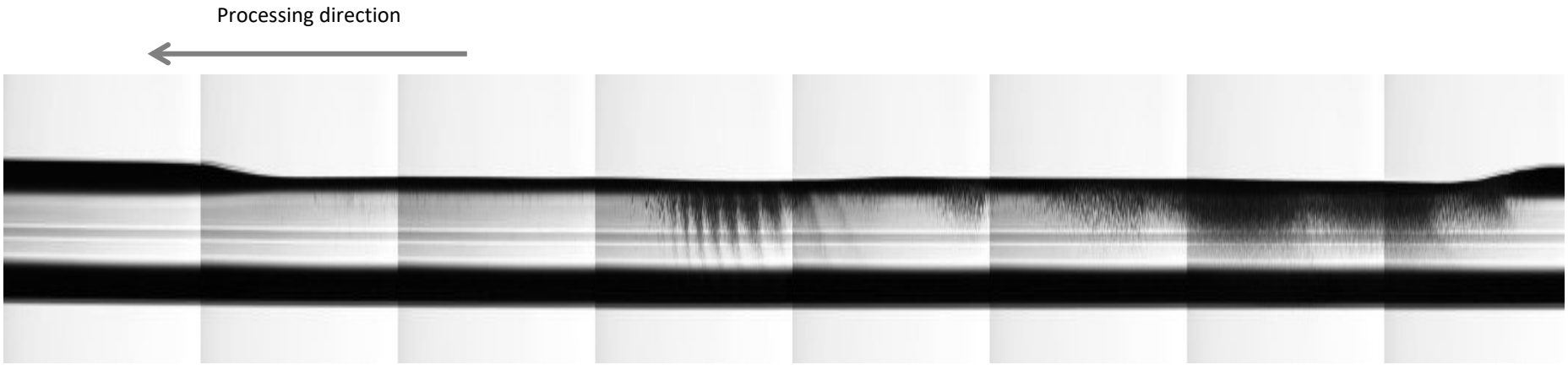

Figure 3.10 Lateral view of a failed 7mm-long LMS with high re-deposition

3.4.5 Characterisation

Figure 3.11 shows the system used to characterise the absorption efficiency and the propagation losses of a processed Tm fibre. Pump light was coupled from a BWT 105/125µm 6W laser diode at 793 nm together with a non-absorbing probe light from a 105/125µm 10W laser diode at 940 nm into the Tm fibre with the aid of a 6+1:1 fibre combiner. Both laser diodes had an NA of 0.15 whilst the fibre had a cladding NA of 0.46. The pump absorption efficiency (including propagation losses) was determined via a cut-back measurement and monitoring of the output power at 793nm whilst monitoring of the 940nm output power was used to ascertain the propagation losses created by the LMS. The fibre under test was kept straight to avoid bend-induced mode-scrambling.

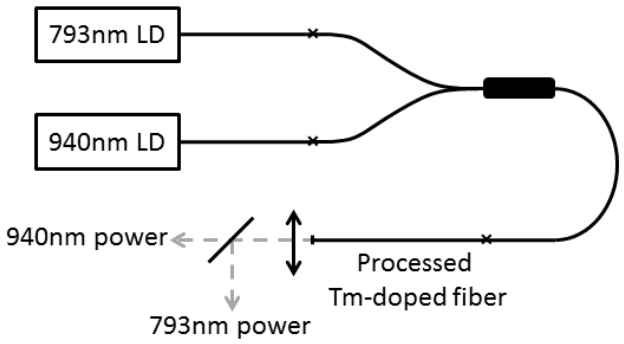

Figure 3.11 Characterisation system for loss and pump absorption measurement

The losses for LMSs with adiabatic transition zones corresponding to the ones described previously were measured to be of less than 1%. Shorter transition lengths with the same maximal depth (i.e. higher tapering angles) were tried out but losses of up to 6% were obtained for tapering angles of 50mrad.

3.5 Results

3.5.1 Influence of processing length

A set of one meter-long Tm-doped fibres with a circular cladding and a doping concentration of 3.5 ±0.3 wt% were processed to create LMSs with the same D-shape depth and transition length but with different total lengths. These fibres had a core/cladding diameter of 10/200µm Pulse duration evolution of the CO_2 laser is shown in Figure 3.12 as well as the LMSs's profile associated.

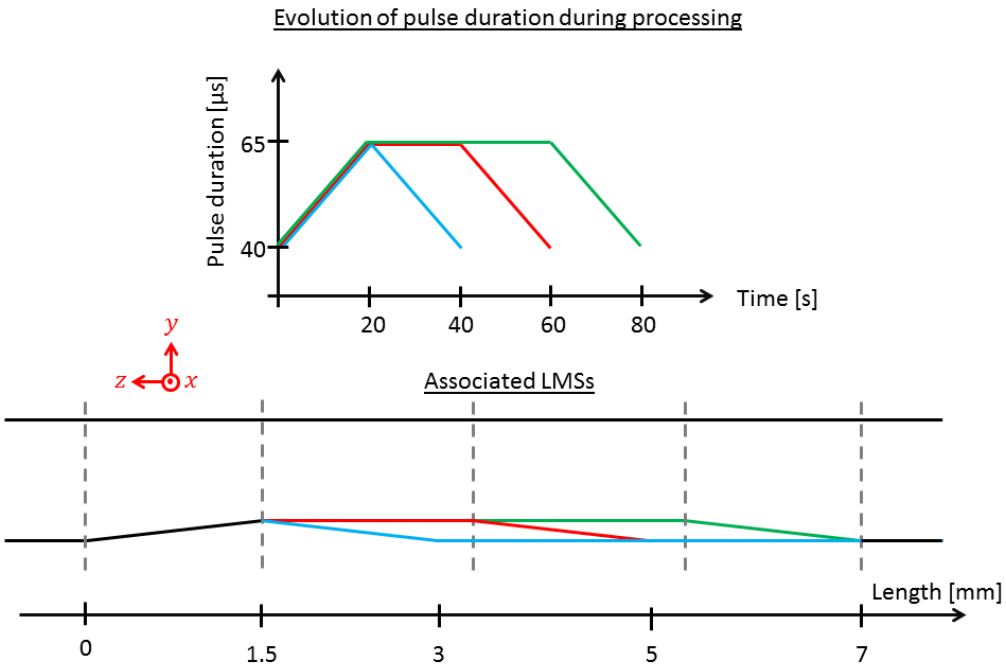

Figure 3.12 Temporal evolution of CO_2 laser pulse duration for LMS creation and the associated LMSs profiles

The laser pulse length was ramped from 40µs, below the ablation threshold, up to 65µs over 2mm, creating an adiabatic transition zone of 1.5mm and a D-shape depth of 15µm. The LMSs were generated in the middle of the fibre and had a respective length of 3, 5 and 7mm. This corresponds to a zone with a depth of 15µm of 0, 2 or 4mm. The absorption enhancement and the losses of these test-fibres were measured via a cut-back measurement and compared to a non-processed fibre tested previously (see Figure 3.2) and used as a baseline for pump absorption).

Figure 3.13 shows the evolution of pump absorption as a function of the mode-scrambler length, linking device length and pump absorption improvement. As the device length increases, the pump absorption improves due a longer interaction length with the incoming pump beam, leading to better mode scrambling, up to a maximum value of 1.4dB/m. By increasing the LMS length, the non-circular section of fibre increases leading to higher interaction with the light propagating in the fibre core. Here a quasi linear relation between LMS length and pump absorption (in dB) as the interaction length is kept quite short to ensure a mostly circular fibre cladding profile. It is expected that by increasing the LMS length to much larger values, the measured absorption for one meter of active fibre would quickly tend to the maximal absorption value observed in similar D-shaped and octagonal fibres (here of 2dB/m). A roll-over would be observed after a significant length of non-circular fibre profile of tens of mm.

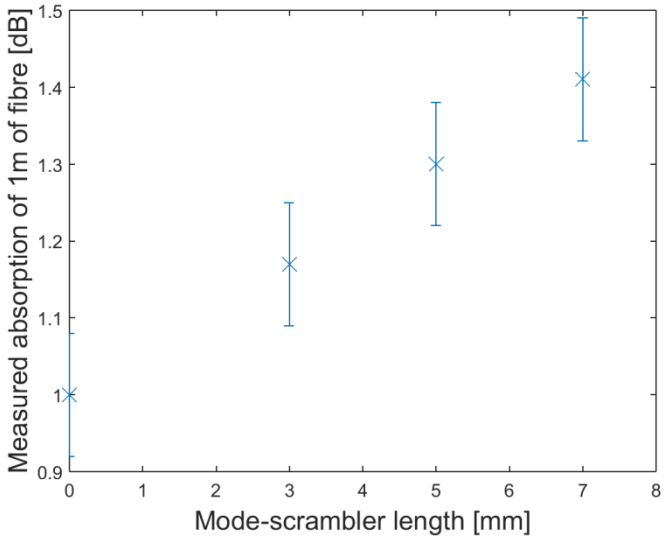

Figure 3.13 Pump absorption for 1m of fibre as a function of mode-scrambler length

Figure 3.14 shows a comparison of pump absorption over 1m for a non-processed fibre and one processed after 50cm with a LMS of 7mm. An increase in pump absorption from 1dB to 1.4dB was demonstrated in a meter-long fibre with a 7mm-long LMS. The processed fibre curve possesses the same gradient just after the LMS as the non-processed one at its beginning and both curves have the same slow gradient at their ends. Moreover, the curve associated with the processed fibre shows an increased gradient just after the LMS over a length of 25cm before going back to its original lower gradient. This distance corresponds to the repetition distance measured from Figure 3.2. No further decrease in gradient is observed for the non-processed fibre as the propagating modes remaining in the fibre after the first 30cm are slowly absorbed and thus a new decrease in gradient would occur over a much longer fibre length. The absorption gradient would decrease slowly over a great fibre length until reaching a flat gradient but here only the first gradient change is of interest in order to maintain this high absorption slope.

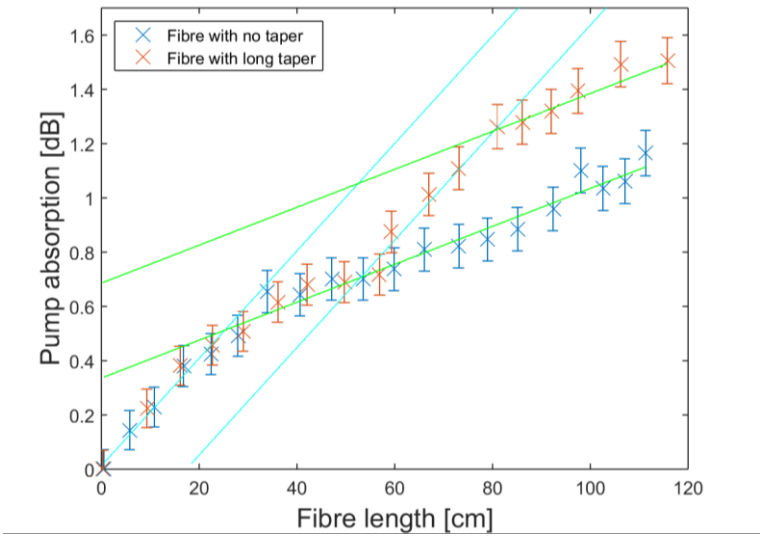

Figure 3.14 Comparison of pump absorption over 1m of fibre for processed and non-processed fibres

3.5.2 Multi-locations LMS

The fibre processed here was a one meter-long 10/200µm Tm-doped fibre. Three LMSs were created along its length, each separated by 20 to 30cm. The mode-scramblers realised here were made with a simpler method without translating the fibre to allow easier and more reliable processing at the expense of slightly shorter LMSs with higher losses. The mode scramblers had a depth of 20µm and a total length of 700µm. A cut-back measurement was conducted to measure absorption efficiency and losses. Figure 3.15 shows pump absorption over the fibre length for the processed fibre and its non-processed version. Absorption results shown here for the active fibre containing three LMSs takes into account the losses created by the LMSs which were evaluated through the use of a non-absorbed 940nm laser diode (see Figure 3.11). As the LMSs are positioned at suitable distance from each other (determined from Figure 3.2) the gradient of the processed fibre curve stays quite close to the one measured during the first 30 cm of a typical non-processed fibre. Improvement of the pump absorption from 1dB/m to 2dB/m was shown, taking propagation losses into account, corresponding to levels achieved with a classical octagonal version of this fibre. Due to the short transition length between circular and D-shape, the LMS were showing residual losses 0.1dB.

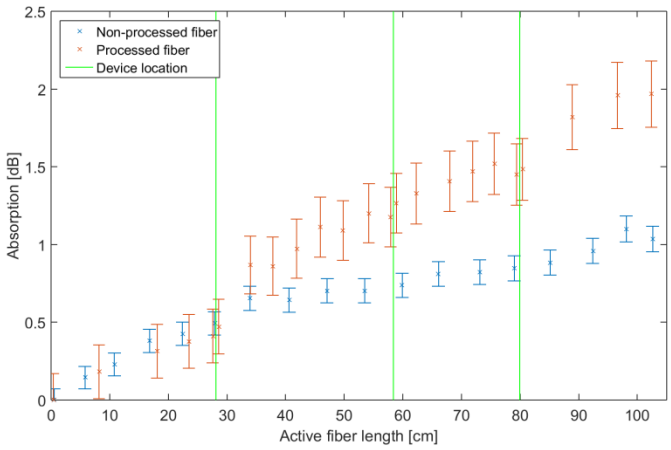

Figure 3.15 Comparison of pump absorption over 1m of fibre for a fibre processed 3 times and a non-processed one

3.6 Fabrication of mode scramblers on the draw tower

We demonstrated the possibility of fabricating low loss, highly efficient mode scramblers by laser processing a stripped section of a circular doped-fibre to improve pump absorption whilst keeping overall circular cladding shape for easy cleaving and splicing. However, the method used here requires localised stripping and processing of the fibre while avoiding contamination. Therefore, repeating the process over the entire length of an active fibre would be very challenging. Each LMS is currently created by a three-step process which is stripping/laser processing/protecting. Each step can lead to damage, additional losses or breakage of the fibre, e.g. breakage during stripping or due to tight bending to fit the fibre into the laser enclosure.

This technology could be implemented on a fibre draw tower as part of the drawing process, when the preform becomes fibre. This would allow for a much more reliable way of creating multiple LMSs in a fibre without any

risk of breakage or complications as the LMS would be created as the fibre is pulled. Moreover, as this would be done just after the furnace stage of the drawing tower, the fibre would still be uncoated at this point, avoiding the stripping step required through our method. Coating would then be done just after the fibre processing, where it is usually done in fibre drawing, solving the issue of protecting the LMSs from damage and contamination. Figure 3.16 shows a schematic of what could be the future method to implement LMSs on a circular active fibre.

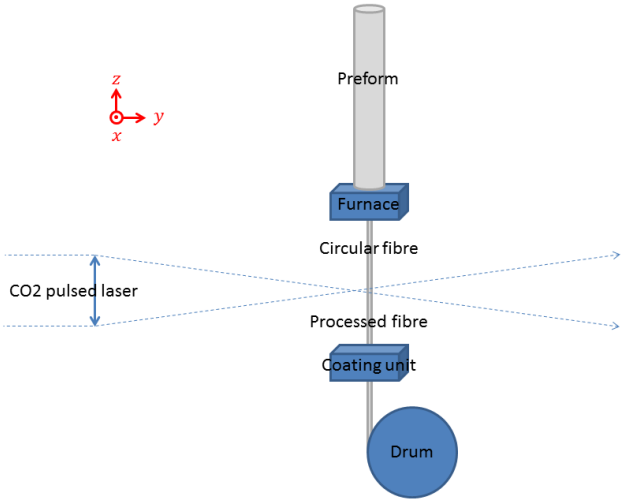

Figure 3.16 Suggested fabrication system integrated on a drawing tower

The fabrication process used previously to show a preliminary result is quite sensitive due to its many steps and can easily lead to breakage of the fibre. As a fibre used in laser configuration would possess many LMSs, breakage is inevitable. Thus, fibre processing during fibre drawing allows fabrication of long fibre lengths containing LMSs needed for laser operation.

The fabrication process used previously in Part 3.5 for a 7mm-long mode scrambler consisted of 4000 pulses every 2 microns over 8mm with a pulse energy varying from 4 to 6.5mJ and can be modified to suit fabrication during fibre drawing for fast and reliable LMS creation.

The CO_2 laser requirements to implement this on a drawing tower depend on the amount of fused silica removed, which in turn depends on the design of the LMS.

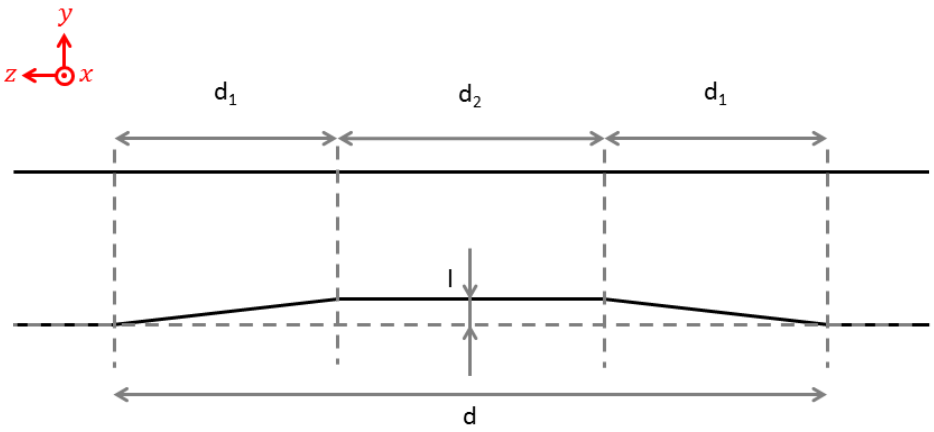

Figure 3.17 Schematic length of a LMS

If we call A(z) the removed area of the LMS at the position z (shown in Figure 3.17 and Figure 3.18), the volume of glass removed V is:

$$V = \int_0^d A(z)dz \tag{3.1}$$

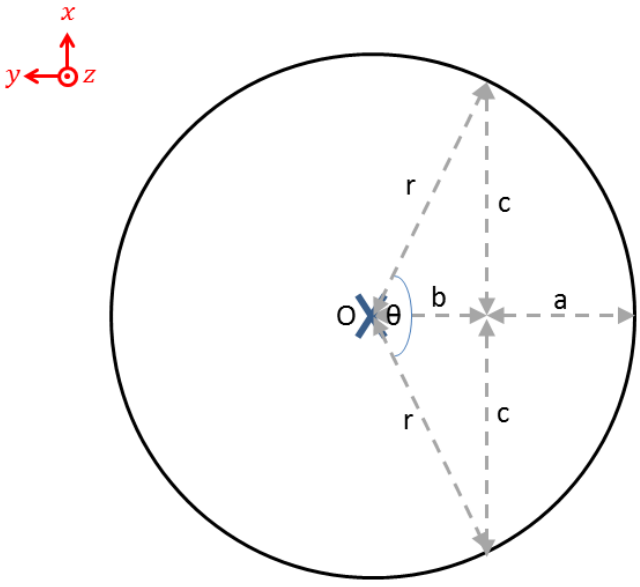

Figure 3.18 Cross-section schematic dimensions

With, according to Figure 3.18:

$$A(z) = \pi r^2 \frac{\theta}{2\pi} - b.c \tag{3.2}$$

The volume of glass removed in an LMS is then (see Appendix Section 1):

$$V = \frac{2r^3 d_1}{l}\left(\sqrt{1-\left(\frac{r-l}{r}\right)^2} - \frac{r-l}{r}\cos^{-1}\frac{r-l}{r}\right) - \frac{2d_1}{l}\frac{(2rl-l^2)^{3/2}}{3} + d_2\left[r^2\cos^{-1}\left(\frac{r-l}{r}\right) - (r-l).\sqrt{2rl-l^2}\right] \quad (3.3)$$

For the LMSs described here (7mm long including two 1.5mm transition zones and a maximal depth of 15µm), equation (**3.3**) gives a volume a glass removed of:

$$V = 5.57\ 10^{-6}\text{cm}^3$$

As pure silica has a volume density of 2.2g/cm^3 [3.8-10], the mass removed is:

$$X = 12.26\mu\text{g}$$

Fused silica has a specific heat capacity ρ between 680 and 740 J/kg/K [3.8-10]. To achieve ablation, a temperature rise of 3000K is required therefore the energy required to ablate the amount of glass required for a LMS would be for the maximal value of ρ:

$$E = X*\rho*\Delta T \quad (3.4)$$

$$E = 27.7\text{mJ}$$

A drawing tower has a typical drawing speed of 1m/s when fabricating active fibres. This corresponds to a window of 7ms to process each LMS with a non-moving pulsed CO_2 laser. CW lasers are not an option as high peak energy is required to reach the ablation threshold of the glass.

Using a CO_2 laser having a repetition rate of 10kHz, would lead to a processing over 70 pulses with a pulse every 100µm. If the pulse is focused on the exact zone, each pulse must contain up to 530µJ, with a ramping from 0 to this value in transition zones. For 10µs pulses, this would correspond to a peak power of 53W.

By scaling the peak energy from the experimental demonstration, starting just below the ablation threshold up to pulses of 10µs with a peak power of 53W we deduce that ramping of the power from 32 to 53W (peak power), followed by a plateau at 53W and a decrease down to 32W before turning off the laser would be the required process to create theses LMSs.

A more convenient way to do it would be by focusing the beam in the vertical dimension (Z axis) whilst keeping a large beam along the X axis. A beam having a size of 50µm by 1mm would be more convenient as the margins on the positioning of the fibre won't be as tight but would require a laser power going from 640 to 1040W peak power by scaling the laser power calculated previously. Figure 3.19 show the evolution of peak power required to process these LMSs on the draw tower with a CO_2 laser delivering 10µs pulses at a rate of 10 kHz for both cases (with and without margin tolerances). Such laser systems are commercially available.

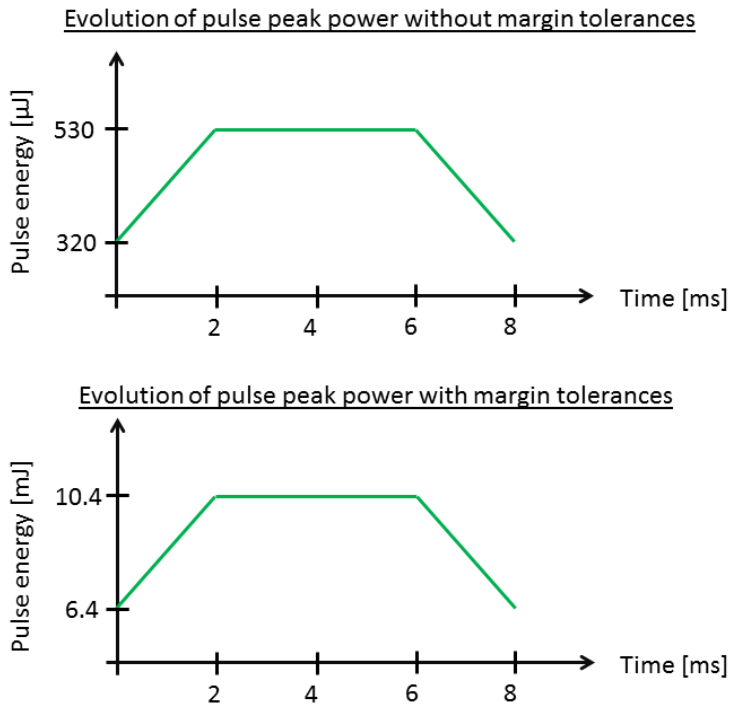

Figure 3.19 Laser energy evolution for processing on draw tower with and without tolerances

3.7 Conclusion

In conclusion, we showed a novel way of improving pump absorption in cladding-pumped fibres whilst conserving a circular cladding over most of the fibre length. A circular cladding shape is strongly beneficial for its use in industrial products where ease and reliability of cleaving and splicing are compulsory. This concept was based on the idea of creating localised D-shaped regions in a circular fibre in order to realise mode scrambling. This mode scrambling permitted energy transfer from pump modes poorly absorbed to strongly absorbed ones due to their high overlap with the doped core. First results showed a significant pump absorption improvement of more than 0.4dB/m by the addition of only one LMS in a one-metre long active fibre. Moreover, a preliminary study of the mode scrambler length influence on pump absorption was carried out showing that, for a 8% maximum D-shape, a total length of 7mm was improving pump absorption for 1dB to 1.4dB in a meter-long fibre.

A multi-LMSs fibre was then demonstrated containing 3 devices over 1m of active fibre and achieving 2dB pump absorption compared to 1dB when non-processed; the processed fibre achieved the same absorption compared to an equivalent octagonal fibre whilst maintaining its circular profile over more than 95% of its length.

Lastly, a fabrication concept was proposed to implement this setup on a drawing tower to carry out the LMS fabrication process whilst pulling the fibre and calculations were carried out to evaluate the laser system required to implement this technology on a pre-existing tower.

3.8 References

3.1. Javadimanesh, M., et al., *The effect of cladding geometry on the absorption efficiency of double-clad fiber lasers.* Optica Applicata, 2016. **46**(2): pp. 277-289.

3.2. Leproux, P., et al., *Modeling and optimization of double-clad fiber amplifiers using chaotic propagation of the pump.* Optical Fiber Technology, 2001. **7**(4): pp. 324-339.

3.3. Li, Y.H., S.D. Jackson, and S. Fleming, *High absorption and low splice loss properties of hexagonal double-clad fiber.* Ieee Photonics Technology Letters, 2004. **16**(11): pp. 2502-2504.

3.4. Liu, A.P. and K. Ueda, *The absorption characteristics of circular, offset, and rectangular double-clad fibers.* Optics Communications, 1996. **132**(5-6): pp. 511-518.

3.5. Narro-Garcia, R., et al., *Study of the pump absorption efficiency in D-shaped double clad optical fiber.* Optica Applicata, 2012. **42**(3): pp. 587-596.

3.6. Zhou, J., et al., *A new inner cladding shape for high-power double-clad fiber lasers.* High-Power Lasers and Applications Ii, 2002. **4914**: pp. 146-150.

3.7. Shardlow, P.C., et al., *Cladding shaping of optical fibre preforms via CO2 laser machining*, in 2015 European Conference on Lasers and Electro-Optics - European Quantum Electronics Conference, (Optical Society of America, 2015), paper CJ_P_29.

3.8. *https://www.azom.com/properties.aspx?ArticleID=1114*.

3.9. *http://accuratus.com/fused.html*.

3.10. *https://www.crystran.co.uk/optical-materials/silica-glass-sio2*.

Chapter 4. Misalignment insensitive feedback scheme for fibre lasers

4.1 Introduction

Dramatic advances in cladding-pumped fibre laser technology over the last two decades have allowed the development of highly efficient lasers with output powers reaching the multi-kW regime and excellent beam quality serving a wide range of applications [4.1-3]. The advantages of fibre lasers for scaling output power are derived from their thin and long geometry which allows simple thermal management and a high degree of immunity from thermal effects, such as thermal lensing, occurring inside the gain medium due to tight mode confinement compared to bulk lasers. However, these advantages come at the price of much tighter alignment tolerances when integrating fibre gain media with free-space optical arrangements. For a number of applications, the requirement for flexibility in mode of operation and/or operating wavelength often dictates the use of an external feedback cavity based on a collimating lens and a plane reflector with additional components (e.g. Q-switches, wavelength tuning elements, etc) to achieve the desired mode of operation [4.3-14]. However, such cavities are very prone to misalignment due to differential thermal expansion of the optical components and mechanical vibrations, particularly in demanding environments such as in aircraft and in space, making them unpopular for practical applications. Figure 4.1 shows the schematic of a free-space feedback arm utilised in a fibre laser. Unwanted movement of the fibre tip relative to the collimating lens, after accurate positioning, occurs in 3 directions: either as transverse movement in the focal plan along the x and y axes (laterally, vertically or a combination of both) or out of the focal plane along the optical axis (z axis).

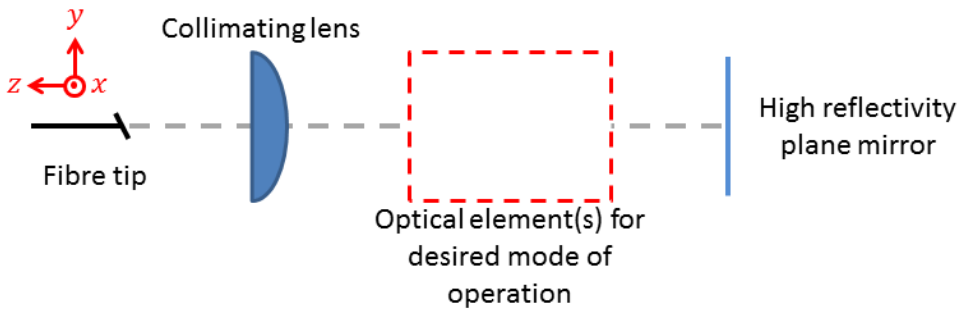

Figure 4.1 Schematic of a conventional free-space feedback arm in a fibre laser.

Any movement of the fibre along the z axis (see Figure 4.1) out of the focal plane will reduce feedback efficiency by degrading collimation and is dependent on the collimating lens used [4.15], reaching tolerances from 10s to 100s of microns. Transverse movement leads to an angular change of the collimated beam incident on the final high reflector and, consequently, in an increase of cavity loss yielding re-coupling efficiency of less than 50% for a movement of the fibre end by more than the fibre mode field diameter [4.15, 16]. Designing external cavities to maintain such tight alignment tolerances whilst simultaneously being compatible with high operating power is very challenging.

Here we report an alternative external feedback cavity arrangement that is compatible with high power operation and which has demonstrated dramatically improved alignment tolerances. Approximately two orders of magnitude improvement in transverse movement tolerance is demonstrated with the alternative feedback cavity proposed here compared to a conventional feedback cavity. The improved alignment sensitivity is achieved by simply replacing the plane mirror high reflector by a corner-cube retro-reflector. Corner-cubes are sometimes used in solid-state configurations for their ability to track a wandering gain medium but lead to many issues in solid-state polarisation sensitive systems due to the complex effect of a retro-reflector on the polarisation state. A corner-cube induces a position-dependent scrambling of polarisation hard to characterise [4.17-22], leading to unstable spatial beam profile [4.23, 24]. This work is, to the best of our knowledge, the first use of a retro-reflector as feedback element in a fibre laser leading to fibre tip movement improvement.

4.2 Novel concept

Free-space feedback arms in fibre lasers are often designed as described previously in Figure 4.1; containing two main components; first a collimating optic situated just after the fibre tip (either a lens or a curved mirror) and a reflective element, usually a plane mirror, at the end of the feedback arm with specific elements in between to achieve the desired mode of operation, from a saturable absorber, an acousto-optic modulator (AOM) or an electro-optic modulator (EOM) to achieve Q-switching or an acousto-optic tunable filter or an etalon to obtain wavelength selectivity. Feedback issues occur in such a free space arm particularly when the fibre tip is transversally moved [4.15, 16] as shown in Figure 4.2. The fibre tip is often secured in a fixed position, with a V-groove for example, but any thermal effect or vibrations can make the fibre tip position move relative to the collimating lens axis, leading to the incoming angle on the reflective element to change. Thus, when using a plane mirror at the end of the feedback arm, the reflected light will not be sent back parallel to the incoming collimated beam and subsequently will not be fully re-coupled back into the core.

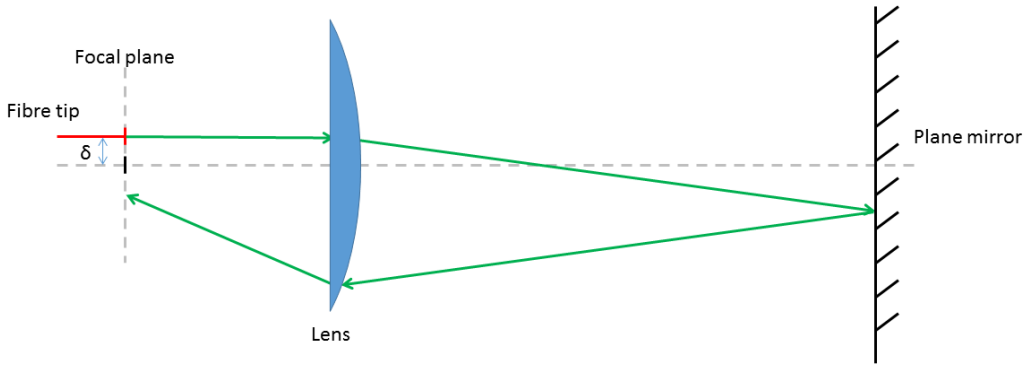

Figure 4.2 Ray tracing of an incoming beam on a plane mirror after fibre tip transverse displacement.

This issue can theoretically be solved by utilising a corner-cube instead of a plane mirror. Corner-cubes are retro-reflective elements, reflecting any collimated beam parallel and would thus avoid reflected light missing the fibre core, as shown in Figure 4.3 where the reflecting element at the end of the feedback arm is replaced by a

corner-cube. Such elements are often used for communication and position systems by reducing the need for receiver alignment, particularly useful when considering moving cars [4.25-27].

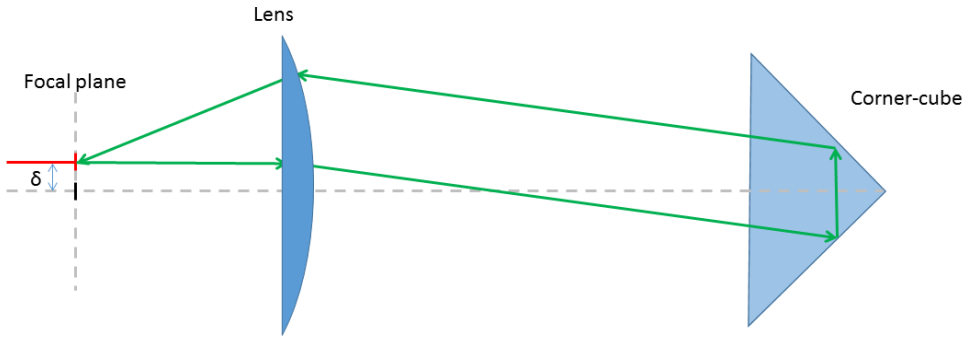

Figure 4.3 Ray tracing of an incoming beam on a corner-cube after fibre tip transverse displacement.

Figure 4.4 shows the basis of a new free-space feedback arm for fibre lasers which contains a collimating lens, followed by mode of operation selective optical components (AOM, etalon, AOTF…) and terminated by a corner-cube instead of a plane mirror as the reflective feedback element. This configuration could be used in fibre laser cavities with much higher insensitivity to transverse fibre tip movement relative to collimating lens and, hence, could be a solution to avoid feedback reduction due to vibrations, e.g. for airborne systems.

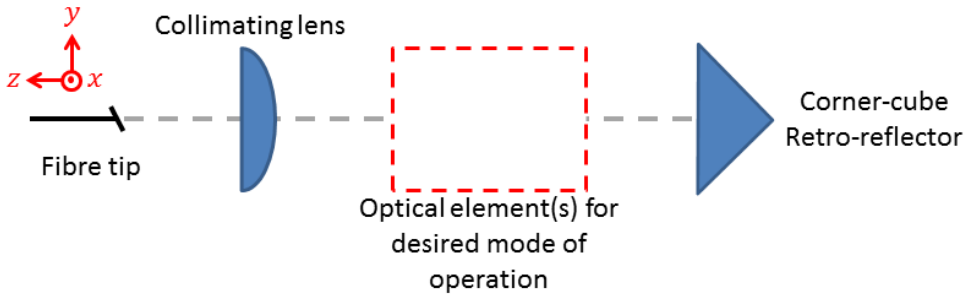

Figure 4.4 Free-space feedback arm concept tolerant to large transverse fibre tip movement

4.3 Theoretical sensitivity to transverse fibre tip movement in free-space feedback arms

4.3.1 Ray tracing approximation

The impact of lower feedback efficiency on laser performance depends on the type of laser and its design. Fibre lasers are generally more tolerant to a reduction in feedback efficiency than other types of lasers due to their high single-pass gain. Further discussion on the influence of feedback efficiency on overall laser efficiency will be considered later in section 4.4.4. For the purpose of the present discussion we simply consider the lower limit on 'acceptable' feedback efficiency as being when the central ray will either be imaged back just missing the core or have an incident angle into the core greater than the core NA, and hence not fulfilling the guiding criteria.

4.3.1.1 Plane mirror

Figure 4.5 shows the ray tracing for a ray exiting the fibre tip after a transverse displacement δ from its original position. Two different issues occur reducing the free-space feedback arm efficiency: light reflected back missing the core and light injected back into the core but unguided due to an angle greater than the fibre core NA.

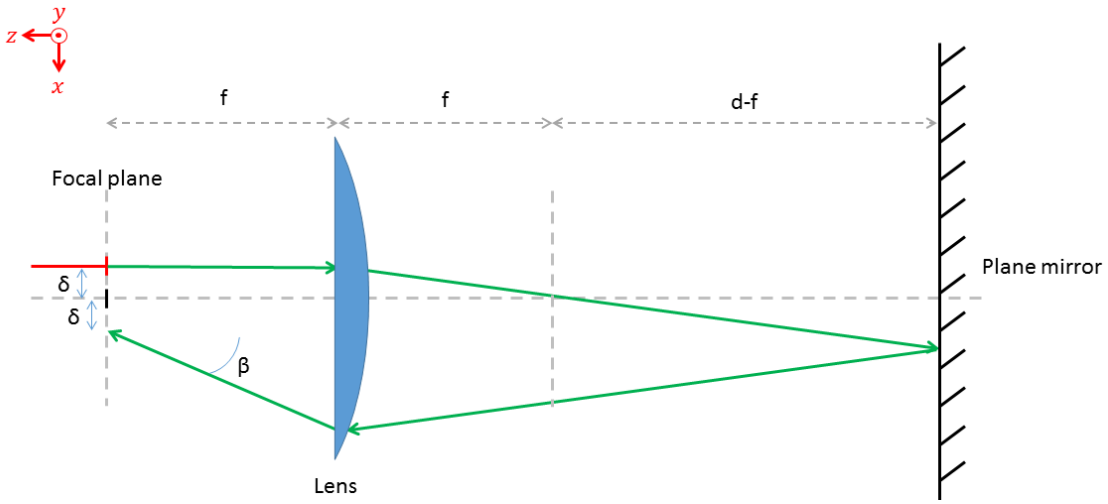

Figure 4.5 Ray tracing of an incoming beam on a plane mirror after fibre tip transverse displacement.

Figure 4.5 shows the ray tracing for the central ray exiting the fibre tip in the focal plane after a lateral movement δ from the optimal position with f the focal length and d the distance between the collimating lens and the corner-cube. Such a ray re-enters the fibre at a position 2δ from its origin with an entry angle β. Thus, for a fibre having a core diameter $\emptyset_{\text{core}}$, any movement of more than $\frac{\emptyset_{\text{core}}}{2}$ will lead to a 'low' feedback efficiency from the free-space arm as the light will not couple into the core. Therefore a distance δ_{max1} can be defined corresponding to the minimal transverse movement when the low feedback situation occurs:

$$\delta_{\text{max1}} = \frac{\emptyset_{\text{core}}}{2} \tag{4.1}$$

A single-mode fibre usually possesses a core diameter close to its MFD and the theoretical expectation agrees with previous work [4.15].

Assuming $\delta \ll f$, we can approximate $\beta \approx \tan\beta$ and therefore:

$$\beta \approx 2\delta\frac{\text{d-f}}{\text{f}^2} \tag{4.2}$$

To fulfil the core guiding criteria, one must have $\beta \leq \text{NA}$, leading to a maximal movement δ_{max2} before achieving 'unacceptable' feedback efficiency of:

$$\delta_{\text{max2}} = \frac{\text{f}^2\text{NA}}{2|\text{d-f}|} \tag{4.3}$$

Such a displacement would need to be in the order of hundreds of microns to lead to NA mismatch. Here we particularly focus on single-mode fibres compatible with SMF28e, i.e. having a core diameter of around 10µm with an NA around 0.15, which means that $\delta_{max1} \approx 5\mu m$.

Therefore, the main concern on feedback efficiency reduction due to fibre tip movement when using a plane mirror in the feedback arm is not NA mismatch but reflected light being imaged back offset from the core. As such the fibre tip cannot be moved by more than a fibre core radius before reaching high external feedback cavity losses.

4.3.1.2 Corner-cube

Figure 4.6 shows a free-space feedback arm comprising a corner-cube as reflective element utilised in a fibre laser and an example of ray tracing after a transverse movement δ of the fibre tip whilst remaining in the focal plane. The retro-reflecting property of the corner-cube ensures the reflected light is imaged back into the core for transverse movement of the fibre tip inside the focal plane. Thus, the previous problem when using plane mirrors of reflected light not reaching the core for movements greater than δ_{max} from equation (**4.1**) does not apply.

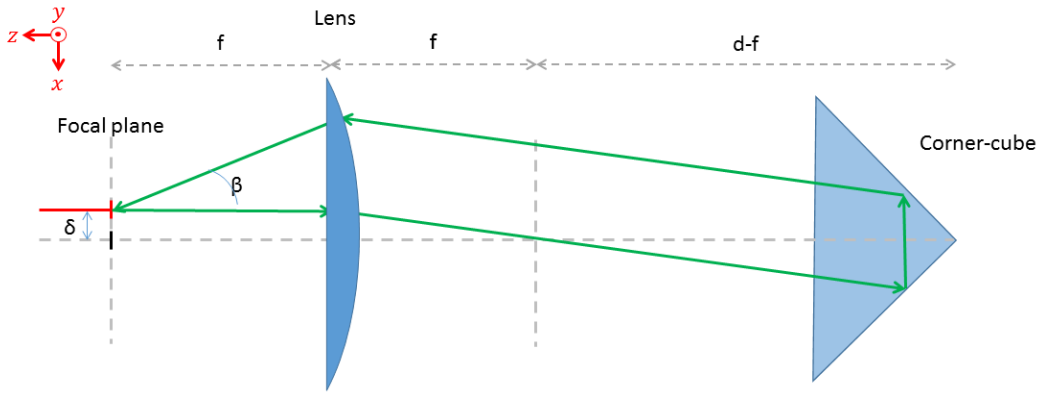

Figure 4.6 Ray tracing of an incoming beam on a corner-cube after fibre tip transverse displacement.

However, this new system does not fix possible NA mismatch of the reflected light; the reflected rays will have a different entry angle (see Figure 4.6) which is function of collimating lens focal length and the feedback arm length. Reflected light will reach the core but will only be kept in it through total internal reflection (TIR) if $\beta \leq \mathrm{NA}$. The maximum tolerated movement δ_{max2} was described in equation (**4.3**); for a single-mode fibre SMF28e having an NA of 0.15 and a collimating lens f=10mm, one can achieve a movement $\delta_{max2} = 750\mu m$ whilst still achieving high feedback efficiency.

Thus, by using a corner-cube instead of a plane mirror as reflective element in a feedback arm, feedback losses when transversally moving the fibre tip are only due to NA mismatch between the fed back light and the fibre core, allowing an insensitivity improvement by two orders of magnitude.

4.3.2 Theoretical reflectivity utilising a corner-cube based on NA mismatch

Any collimated beam hitting the corner cube will be submitted to a central symmetry centred on the apex of the corner cube before being sent back parallel to its incoming direction. Figure 4.7 shows such a symmetry.

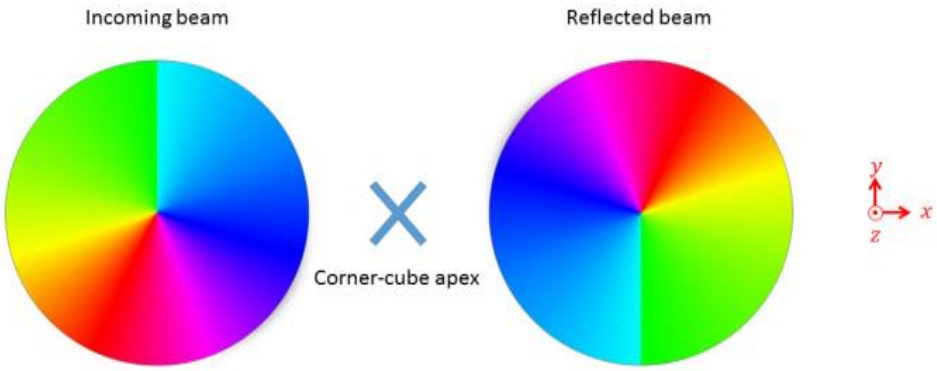

Figure 4.7 Example of collimated beam hitting a corner-cube, submitted to a central symmetry centred on the corner-cube's apex

One can then deduce that the only rays fed back into the fibre core with a NA satisfying the total internal reflectivity criteria would be the ones coming from the spatial overlap zone of the incoming and reflected beam. Figure 4.8 shows what the shape of this zone (in red) looks like after a fibre tip displacement along the x axis.

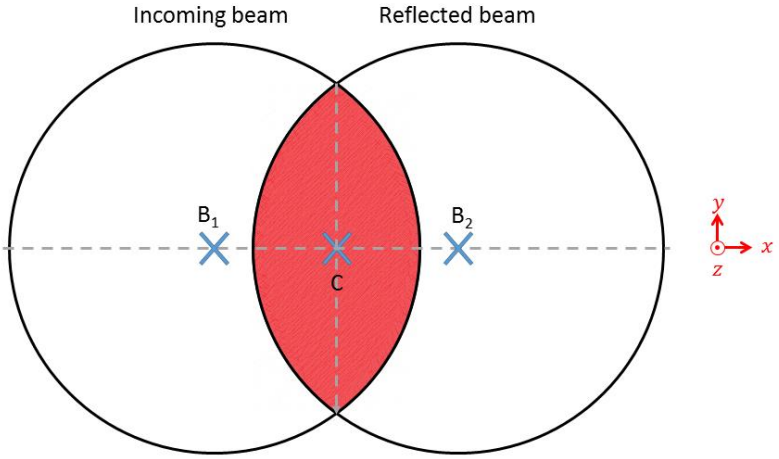

Figure 4.8 Overlap of incoming and reflected beam in a corner-cube

Where C is the apex of the corner cube, B_1 is the centre of the input beam and B_2 the centre of the output beam. Considering that the incoming beam has an area $S_{\text{incoming beam}}$ and the reflected one an area $S_{\text{reflected beam}}$, if C has for coordinates (0,0), the area S_1 corresponding to this overlap contains all the points P(x,y) such as:

$$P(x,y) \in S_{\text{incoming beam}} \ \& \ P(x,y) \in S_{\text{reflected beam}} \tag{4.4}$$

To be fed back into the fibre core without NA mismatch, a point P needs to adhere to the following distance criteria:

$$PB_1 \leq f.NA \;\&\; PB_2 \leq f.NA \tag{4.5}$$

For an input beam centred on $B_1(\frac{f-d}{f}\delta, 0)$ having an normalised intensity profile I(x,y) we can calculated the corner-cube reflectivity. Considering an incoming beam having an axial symmetry along the horizontal axis, we obtain (details in Appendix Section 2 Part 1):

$$R = 2\int_{x=-\left(f.NA\cdot\frac{|d-f|}{f}\delta\right)}^{x=f.NA\cdot\frac{|d-f|}{f}\delta}\int_{y=0}^{y=\sqrt{(f.NA)^2-\left(|x|+\frac{|d-f|}{f}\delta\right)^2}} I(x,y)dxdy \tag{4.6}$$

For a top hat beam, the ratio of this area to the collimated beam area gives the reflectivity of the corner (the latest being considered lossless here).

$$R = 1-\frac{4}{\pi(f.NA)^2}\left(\frac{|d-f|\delta\sqrt{(f.NA)^2-\left(\frac{|d-f|}{f}\delta\right)^2}}{2f} + \frac{(f.NA)^2}{2}\sin^{-1}\frac{|d-f|\delta}{f^2.NA}\right) \tag{4.7}$$

The part of the collimated beam not confined to the core due to NA mismatch corresponds one edge of the incoming beam (as seen on Figure 4.8). Thus, total reflectivity for a Gaussian beam should be less sensitive to displacement than for a top hat beam as most of the energy is concentrated into the central zone of the beam.

Figure 4.9 shows the evolution of reflectivity for a perfect corner-cube (i.e. offering a maximal reflectivity of 100%) as a function of lateral displacement from the optimal fibre tip position and of feedback arm length. Figure 4.9 particularly shows reflectivity evolution of such a feedback arm for two different beam profiles: a top-hat and a Gaussian beam as plotted from equation (**4.6**) and its simplified equation (**4.7**). Transverse displacement is expressed in number of collimated beam radii ($f.NA$) and the feedback arm length in number of focal length $\left(\frac{f+d}{f}\right)$. These scales are chosen as the feedback arm reflectivity R expressed previously in eq.(**4.6**) is dependent on the focal length, the NA and the distance d and such a representation is applicable to any triplet (f,NA,d). One can easily see for a selected system having a fixed triplet (f,NA,d) how the reflectivity R evolves as a function of displacement d.

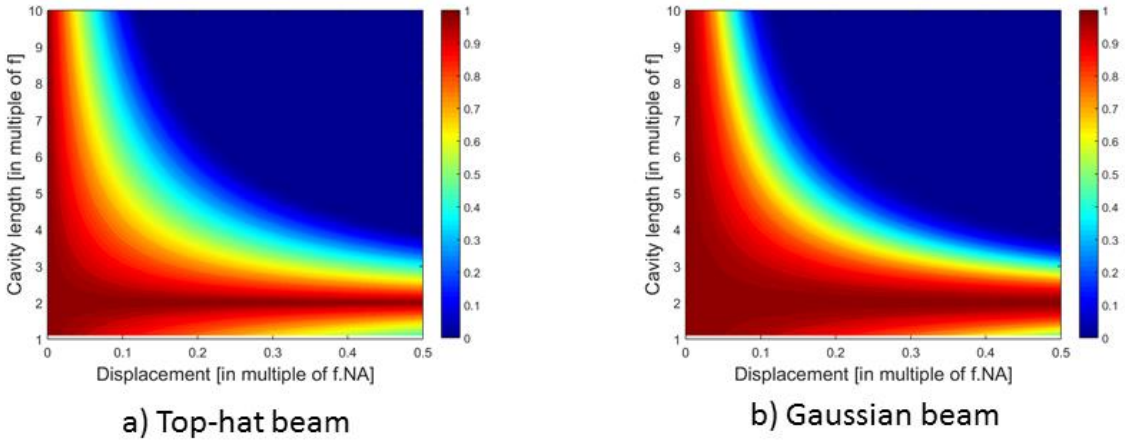

Figure 4.9 Simulation of a corner-cube reflectivity as a function of f,d and NA for a Gaussian beam and its top-hat approximation

Figure 4.9 shows that a feedback arm containing a corner-cube as reflective element offers a theoretical reflectivity of 100% for an arm length of twice the focal length for any transverse fibre tip displacement (within the assumption $\delta \ll f$). For a two focal lengths feedback arm, the input beam is centred on the apex of the retro-reflector independently of fibre tip displacement, leading to a theoretical full insensitivity to displacement. The calculated reflectivity simulation shown here does not take into account aberrations which occur when moving away from the collimating lens centre nor the fibre tip moving out of the focal plane for large displacements causing collimation issues. Moreover, the high reflectivity zone becomes narrower for large displacements and laser efficiency can drastically decrease when the assumption that $\delta \ll f$ is not valid anymore. Collimation adjustment is therefore required for high fibre displacement in order to maintain high external cavity feedback efficiency. However, for displacements lower than a twentieth of the beam radius $\left(\frac{f.NA}{20}\right)$, high reflectivity of the feedback arm can be achieved even for long lengths where $d > f$. This tolerance is particularly visible on Figure 4.9b showing the simulation for a Gaussian beam.

Gaussian beams offer much higher reflectivity on the corner-cube than when simplifying their profile into a top-hat beam; this is due to their intensity profile concentrating a high fraction of the power near the centre of the beam. An improvement of reflectivity by more than 10% can be observed for the Gaussian beam profile compared to a top-hat beam profile in specific areas, particularly for a typical displacement of a tenth of the beam radius or lower combined with long feedback arms.

4.4 Experimental verification of misalignment insensitivity improvement

4.4.1 Experimental setup

This feedback arm arrangement for transverse fibre tip movement insensitivity improvement was tested for a simple cladding-pumped Tm-doped silica fibre laser. The experimental set-up (shown in Figure 4.10) is a linear cavity containing a free-space feedback arm. The cavity comprises a 3m long double-clad non-circular Tm-doped

gain fibre fabricated in-house with 2wt% Tm concentration, 0.15NA and a 10.5µm core diameter. A 20W pump diode at 793 nm with a NA of 0.15 was free-space coupled into the fibre's 0.46NA 130µm diameter octagonal inner-cladding. The pump end of the active fibre was perpendicularly-cleaved to act as the output coupler with a Fresnel reflectivity of ~3.5%. The opposite end of the active fibre was spliced onto an angle-polished connector (APC) to suppress unwanted feedback via Fresnel reflection and avoid parasitic lasing. The APC was followed by an external feedback cavity which consisted of an anti-reflection coated collimating lens followed by a dichroic mirror to remove the unabsorbed pump light and a one-inch corner-cube retro-reflector, following the configuration described previously in Figure 4.4. The retro-reflector was a glass type corner-cube based on total internal reflection fabricated from high-grade fused silica (EdmundOptics) to avoid absorption at 2µm.

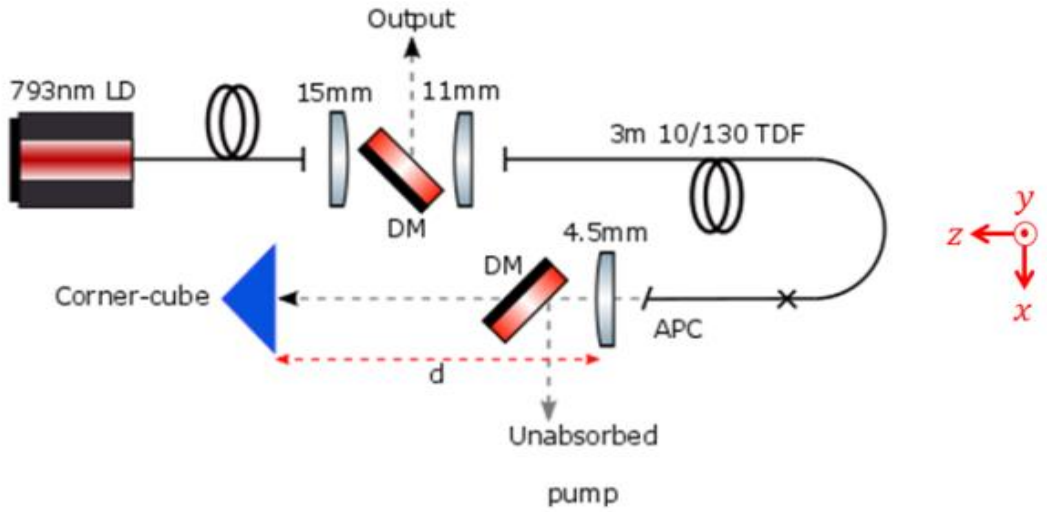

Figure 4.10 Experimental laser setup for corner-cube based external feedback cavity.

The faces were uncoated and hence produced an additional resonator loss of ~7% due to two Fresnel reflections at the front surface on the way in and out. For the purpose of comparison, the corner-cube could easily be replaced by a plane mirror with high reflectivity (>99.8%) at the lasing wavelength (~2 µm) whilst maintaining the same free-space arm length and the collimating lens could also be easily changed as, from equation (**4.3**), movement tolerances are dependent on the focal length and the lens-to-reflector distance. The collimating lens used at the output coupler was an 11mm aspheric lens anti-reflection coated at pump and signal wavelengths. The intra-cavity dichroic mirror had coatings on one face achieving high transmission at signal wavelength high reflectivity at pump wavelength whilst the other face's coating was design for high signal transmission only. The dichroic mirror next to the output coupler, however, was coated on both faces to obtain high pump transmission with one of the coatings designed to achieve high signal reflectivity. Both dichroics were plane and specified to operate at 45°.

As vertical and horizontal movements of an equal specified value lead to the same the same effect on angular change of the collimated beam exiting the collimating lens, we only study the influence of lateral movement (in the x-direction) on the external feedback arm efficiency in order to keep the collimated in the horizontal plane for safety reasons.

4.4.2 Fibre tip transverse movement tolerances using a plane mirror and corner-cube

Three different lenses were used to investigate variation of beam radii. The collimating lenses used here in the feedback arm were an 11mm aspheric or a 20mm plano-convex or a 40mm plano-convex. The pump coupling setup does not change as the collimating lenses used for the pump and the output coupler were kept fixed. Only the collimating lens contained in the free-space feedback arm was changes and the APC was repositioned for maximum output power (i.e. optimal collimation) after each lens type. The collimated beam diameters, for a fibre core NA of 0.15, were approximately 3.2mm, 6mm and 12mm respectively. The feedback arm total length (f+d) was kept at 240mm with $d \gg f$, allowing the approximation :

$$\delta \leq \frac{NA.\, f^2}{2d} \tag{4.8}$$

Figure 4.11 shows the evolution of output power when laterally translating the fibre tip from its original optimal position for the three different collimated beam radii. The output power shown here was normalised to facilitate comparison between curves, as maximum output power between each setup (with a different collimating lens) was varied slightly from 4.2 to 4.4W, attributed to lens aberrations and coating losses.

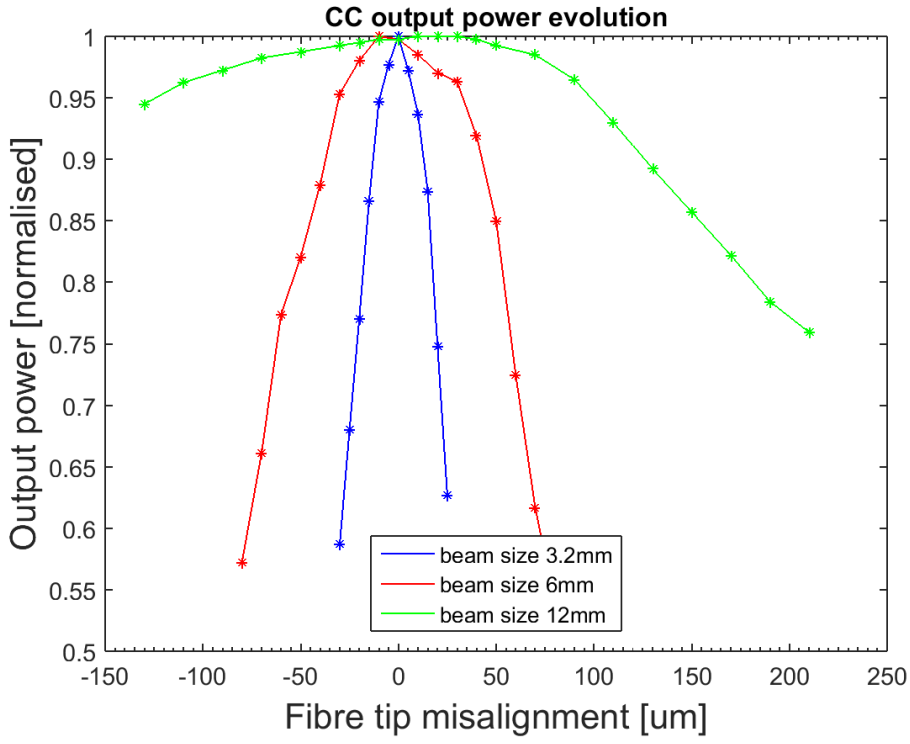

Figure 4.11 Output power evolution as a function of fibre tip displacement with a corner-cube for three focal lengths of 11,20 and 40mm

One can observe that a longer focal length leads to greater transverse misalignment tolerances; this evolution fits with equation (**4.3**) that showed a dependency in $f^2/_{d-f}$ for the maximum acceptable transverse movement.

Here, for a beam diameter of 3.2mm (f=11mm), a movement of $\pm 30\mu m$ leads to an output power decrease of 50% whilst for a beam diameter of 6mm (f=20mm), a movement of $\pm 70\mu m$ is required to achieve similar output power loss. For a 12mm beam diameter (f=40mm), output power decrease when translating the fibre tip is even lower, so much so that the translation stage used here didn't allow movements large enough to reach a 50% output power decrease. The curves presented here show a trend where tolerances increase quickly with focal length/beam radius as it was expected from equation **(4.8)**.

The same experiment was carried out with a high-reflective plane mirror as feedback element. According to equation(**4.1**), the lateral sensitivity is independent of focal length when using a plane mirror. Figure 4.12 shows the evolution of output power when moving the fibre tip with the three different lenses. It was observed that the tolerances increase slightly when using the longest focal length. For the 11 and 20mm lenses, a movement of $\sim \pm 8\mu m$ lead to an output power reduction of more than 50%. This distance is close to the fibre core radius as calculated theoretically in equation (**4.1**). However, when using the 40mm lens, a movement of $\pm 15\mu m$ was required to obtain an equivalent output power loss. This slight discrepancy is due to the use of a plano-convex lens which suffers from spherical aberration with consequent beam distortion. The longer the focal length, the more significant the impact of these aberrations, leading to overall lower output power but higher movement insensitivity. A slight dip is also observed in the middle which is only due to the uncertainty measurement from the power meter used (±3%).

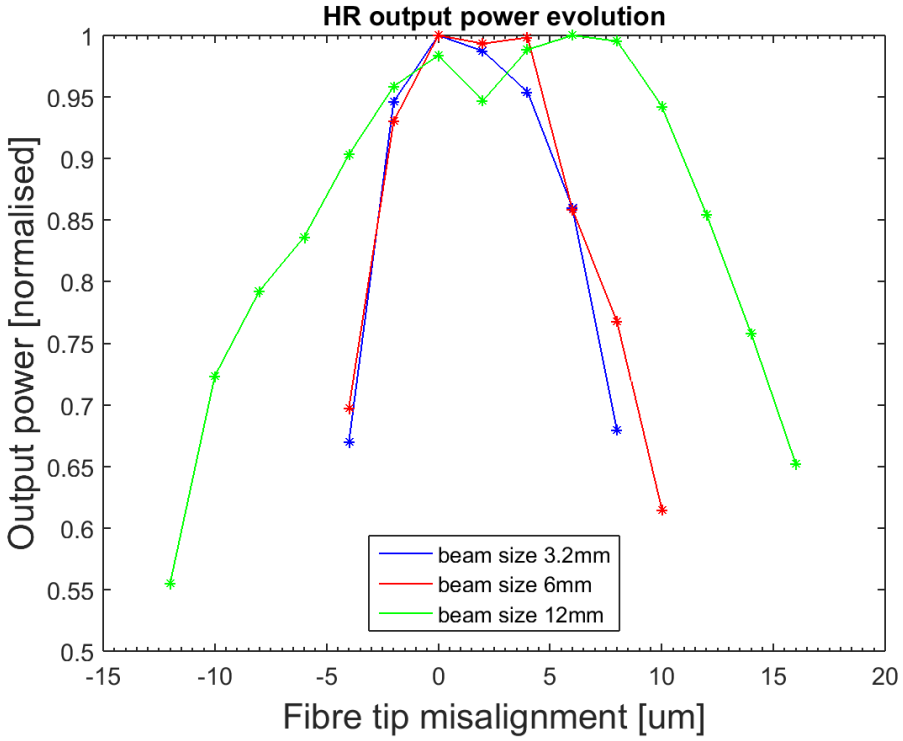

Figure 4.12 Output power evolution as a function of displacement with a mirror for three focal lengths of 11,20 and 40mm.

According to theoretical calculations, for a chosen fibre the tolerances on fibre tip movement depend only on the collimating lens used and feedback arm length. From equation(**4.3**), when conserving a fixed feedback arm length $\mathrm{l} = \mathrm{d} + \mathrm{f} = 240\mathrm{mm}$ as was the case for the experimental results in Figure 4.11 and Figure 4.12 we obtain:

$$\frac{\delta_2}{\delta_1} = \frac{f_2^2|d_1\text{-}f_1|}{f_1^2|d_2\text{-}f_2|} = \frac{f_2^2|l\text{-}2f_1|}{f_1^2|l\text{-}2f_2|} \tag{4.9}$$

From Figure 4.11, it was observed that by moving from a focal length of 11 to 20mm, the tolerance increases by a factor of 3 which fits with the expectation of 3.44 obtained from equation (**4.9**). Accordingly, a difference factor of 15 would be expected between the tolerances corresponding to the 3.2mm and the 12mm beam diameters. Even though the 12mm beam diameter corresponding curve doesn't allow full comparison, a factor of at least 10 seems to fit with the data. The ratios calculated here are smaller than the theoretical ones as aberrations and collimating issues are more prominent for larger fibre tip movement. The lenses are designed for a beam propagation on axis, thus by fibre tip movement the beam is off-axis and leads to some aberration-induced distortion.

According to equation(**4.3**) when using a corner-cube the movement tolerances are dependent on fibre NA, the collimating lens and on the overall free-space feedback arm length. Figure 4.13 shows the evolution of output power as a function of lateral movement for three different feedback arm lengths of 80, 240 and 350mm when using a 40mm focal length collimating lens, corresponding to d=f, 5f and 7.75f. From the previous equations movement insensitivity increases by shortening the feedback arm distance, reaching a totally reflective zone for any fibre tip movement when $\mathrm{f} = \mathrm{d}$. In this experiment the first configuration fulfilled the $\mathrm{f} = \mathrm{d}$ condition.

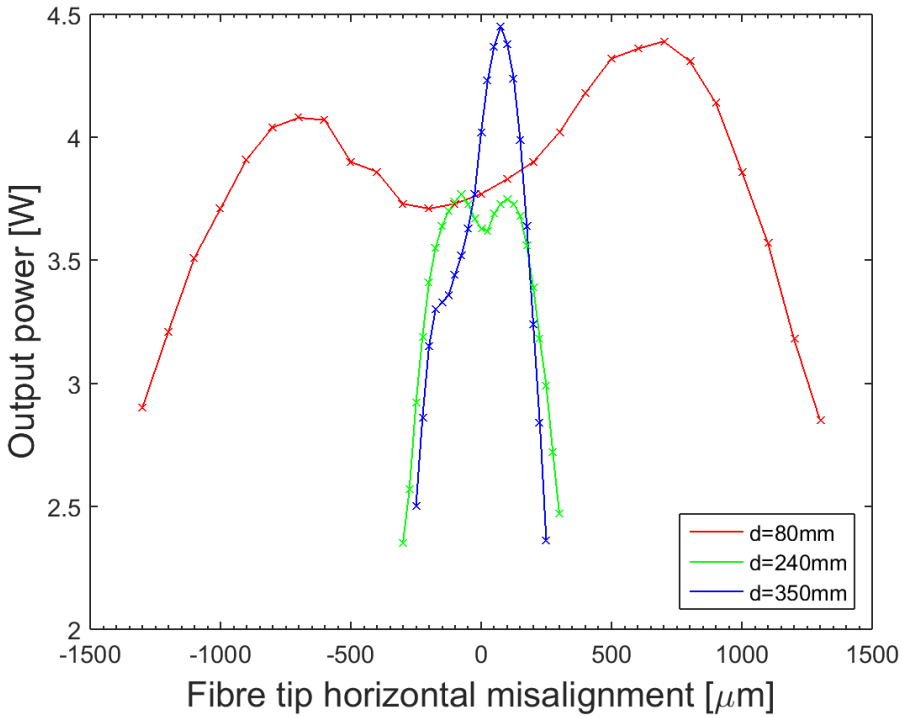

Figure 4.13 Output power evolution as a function of displacement with a corner-cube for three arm lengths

As expected from equation (**4.3**), when decreasing the feedback arm length, the tolerance increases, moving from a tolerance of $\pm 200\mu m$ for a free-space distance of 350mm to up to $\pm 1200\mu m$ for a distance of 80mm. For each distance d, a dip is observed in the middle of the curve; this was due to the overlap of the incoming beam with the corner-cube apex and edges. Counter-intuitively, the position where the beam is perfectly centred on the apex of the corner-cube corresponds to a position of high losses as the edges are not perfectly polished, leading to scattering. Indeed, the corner-cube used here is an uncoated off-the-shelf fused silica one where the cube itself is manufactured through a polishing process. A corner-cube is commonly used for its retro-reflective property in configurations where the beam is quite small compared to the corner-cube diameter and for applications requiring the input and output beams to be spatially separated, therefore avoiding the apex and edges. Thus, imperfect polishing at the edges is often acceptable, resulting here in losses as scattering on the edges and at the apex where the 3 edges meet. Accordingly, when the beam greatly overlaps with these edges (e.g. when perfectly centred), high losses appear leading to a drop of output power.

Comparison of the output power curves in Figure 4.13 with equation (**4.3**) (for a configuration where $f = 40mm$) can be made to demonstrate the influence of feedback arm length on fibre tip movement insensitivity. Careful examination of the data must be done as theoretical calculations were based on a drop of feedback arm efficiency by 50% whilst experimental results correspond to a drop of output power of 30% compared to the maximum output power. Results are summarised in the table below:

d [mm]	δ theoretical [µm]	δ experimental [µm]
40	±∞	±1200
200	±750	±350
310	±444	±200

Table 4-1 Comparison of theoretical and experimental transverse movement tolerances when utilising a corner-cube a feedback element in fibre laser

Experimental values are lower than theoretically predicted values as the latter correspond to a decrease in reflectivity of 50% whilst the experimental values relate to a drop in power by 30%. Laser architectures based on an active fibre as gain medium benefit from the advantage of a long gain region, leading to a high small signal gain, allowing high slope efficiency operation in relatively high loss configurations (as detailed later in Part 4.4.4). Thus, results described in the previous table can only be used to confirm the trend evolution of δ as a function of d instead of comparing theoretical and experimental values. However, measured values yield the same trend as the calculated values, particularly the evolution observed for d=200 and 310mm. The experimental value obtained for d=40mm is of 1.2mm whilst theoretical expectations suggest that any fibre tip movement in this configuration would still yield a reflectivity of 100%. This discrepancy is due to aberrations and focal length changes appearing when the incoming beam is not centred on the lens coupled with collimation issues. A lateral displacement δ of 1.2mm leads the fibre tip to move out from the centre of the optic and thus having a different focal length along the x and y axis which corresponds to moving slightly out of focus.

Movements along the z axis are quite rare for bare fibre tips placed in V-grooves; the fibre tip is usually protruding by few millimetres from the V-groove trench in which it is stuck (usually by taping or clamping). Collimation tolerances are often higher than transverse tolerances which are in the order of a core radius as seen previously. Moreover, vibrations will create a random movement of the hanging part of fibre tip whilst maintaining a quasi-constant distance between the fibre end and the V-groove edge. However, when utilising a corner-cube, transverse tolerances are heavily improved and might lead to collimation issues for large transverse movement out of the optical axis.

4.4.3 Depth movement tolerances out of the focal plane

Movements Δz along the z axis lead the fibre tip to go out of the focal plane and therefore reduce feedback efficiency. By using ABCD matrices, we calculate the evolution of the reflected beam entering the fibre tip as a function of Δz. Figure 4.14 shows a schematic of the feedback arm used where the system is unfolded and the ABCD matrix associated to each part of the setup (either a lens of free-space path).

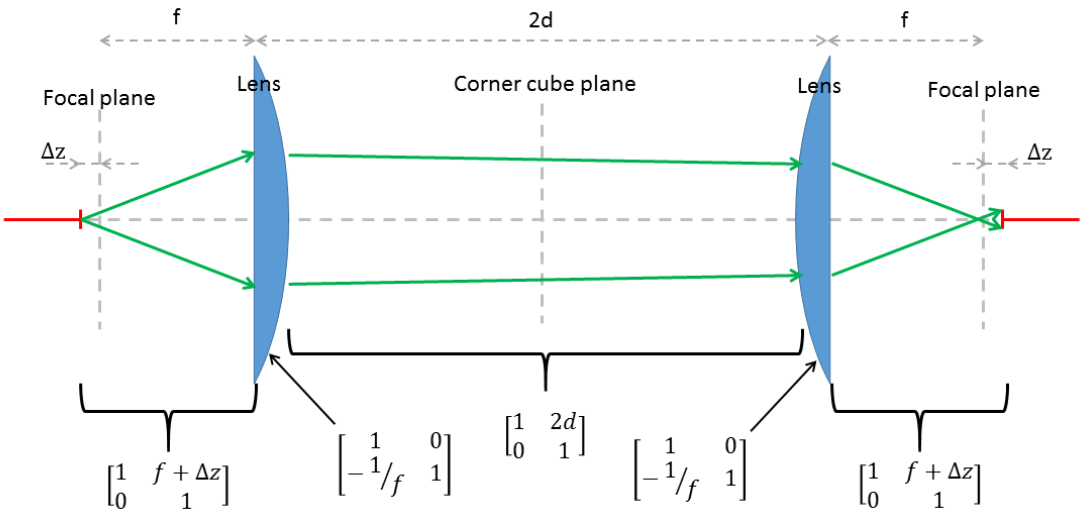

Figure 4.14 Schematic of the feedback unfolded when moving out of the focal plane and the ABCD matrices associated

The full ABCD matrix associated to the system is then (CF Appendix Section 2 Part 2):

$$\begin{bmatrix}A & B\\ C & D\end{bmatrix} = \begin{bmatrix}-1+2\Delta z/f\left(d/f-1\right) & -2\Delta z\left(1+d\Delta z/f^2-\Delta z/f\right)\\ 2/f\left(d/f-1\right) & -1-2\Delta z/f\left(d/f+1\right)\end{bmatrix} \tag{4.10}$$

If we define the complex curvature q(z) at any position z as:

$$\frac{1}{q(z)} = \frac{1}{R(z)} - \frac{i\lambda}{\pi\omega^2(z)} \tag{4.11}$$

With R(z) its curvature and $\omega(z)$ its radius at a position z. Assuming the beam exits the fibre tip at a waist with a complex curvature q_0, then R_0=0, and thus:

$$q_0 = \frac{i\pi\omega_0^2}{\lambda} \tag{4.12}$$

The reflected beam entering the fibre has a value q_1 such as:

$$q_1 = \frac{Aq_1 + B}{Cq_1 + D} \tag{4.13}$$

Combining equations (**4.10**), (**4.11**), (**4.12**) and(**4.13**), and identifying the complex part, we obtain (CF Appendix Section 2 Part 3):

$$\omega_1 = \frac{\lambda}{\pi\omega_0}\sqrt{\frac{B^2 + A\left(\frac{\pi\omega_0^2}{\lambda}\right)^2}{(AD\text{-}BC)}} \tag{4.14}$$

Using a criteria for 'acceptable' feedback defined such as only half of the reflective reaches the core, i.e. $\omega_1 = \sqrt{2}\omega_0$, we obtain for the previous experiments a maximum movement $\Delta z_{max} \approx 20\mu m$ for the three lenses used and for the different free-space feedback arm lengths studied.

Therefore, on the proposed novel feedback arms with increased transverse sensitivity, collimation sensitivity stays quite tight. Moreover, collimation issues will occur when laterally moving the fibre tip as incoming light will not hit the centre of the optic and thus, the lens will have a different focal length along the x and y axis. If is focal length difference exceeds the Δz_{max} value calculated previously from equation (**4.13**), low coupling efficiency will occur.

4.4.4 Corner-cube reflectivity

A drop of output power was previously showed in Figure 4.13 when the input beam was perfectly centred on the apex of the retro-reflector. This power drop is symptomatic of losses occurring along the edges and the apex as unwanted scattering due to a non-perfectly polished corner-cube and leads to a lower overall reflectivity than a plane mirror. This decrease of reflectivity in a feedback arm can be the source of critical issues in a laser cavity, particularly in solid-state configurations but fibre laser cavities are quite flexible and allow high intra-cavity losses whilst still behaving with high slope efficiency. A linear fibre laser comprising a free-space feedback arm can be summarised as the following schematic (Figure 4.15):

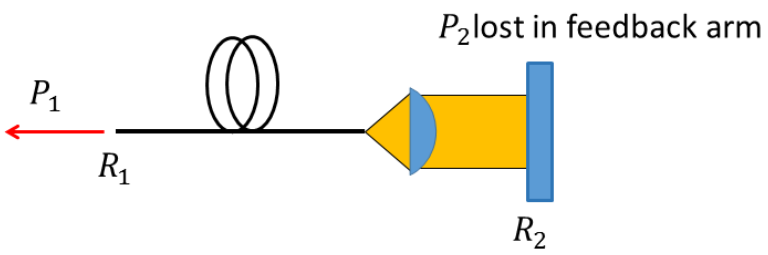

Figure 4.15 Schematic of a fibre laser comprising a free-space feedback arm

In such a configuration, high efficiency is achieved for $P_1 \gg P_2$. The ratio P_1/P_2 is here only dependent on the output coupler's and mirror's reflectivity, assuming other losses negligible and that the feedback arm losses are included in R_2, equalling to:

$$\frac{P_1}{P_2} = \frac{1\text{-}R_1}{1\text{-}R_2}\sqrt{\frac{R_2}{R_1}} \tag{4.15}$$

Reflectivity of the corner-cube can be evaluated by comparing maximum output power of the laser containing the retro-reflector to the same cavity using a high reflectivity plane mirror. This was done for the laser setup comprising a 40mm focal length collimating lens in the feedback arm as this configuration achieved the lowest losses due to unwanted scattering on the edges of the retro-reflector. During this experiment the overall free-space length was kept at a constant length of 240mm. In the configuration explained previously, equation (**4.15**) is always valid with total power generated ($P_1 + P_2$) being approximately constant for a fixed pump power and depends only on the details of the active fibre used and the lasing wavelength. Equation (**4.15**) can be written as:

$${R_2}^2\text{-}\left(2 + \frac{{P_2}^2(1\text{-}R_1)^2}{{P_1}^2 R_1}\right) R_2 + 1 = 0 \tag{4.16}$$

Far from threshold, one can relate P_2 to P_1 with:

$$P_1 + P_2 = P_{tot} \tag{4.17}$$

One can then replace P_2 in equation (**4.16**), leading to a polynomial function having the form:

$${R_2}^2\text{-}\alpha\, R_2 + 1 = 0 \tag{4.18}$$

Where

$$\alpha = 2 + \frac{(P_{tot}\text{-}P_1)^2(1\text{-}R_1)^2}{{P_1}^2 R_1} \tag{4.19}$$

As the reflectivity is comprised between 0 and 1, only the second solution is possible:

$$R_2 = \frac{\alpha\text{-}\sqrt{\alpha^2\text{-}4}}{2} \tag{4.20}$$

For an absorbed pump power of 17.5W, corresponding to more than ten times the laser threshold in each configuration, up to 5.5W of light was generated when butt-coupling a mirror at one end of the fibre. 4.67W was generated by using a plane mirror compared to 4.29W when utilising a corner-cube as reflective element. By applying equation (**4.20**), reflectivity for the plane mirror and the corner-cube configurations can be calculated and compared. Reflectivity of plane mirror configuration was calculated to be of 41% which is quite a

low value but is explained by the problematic feedback into an angle cleaved bare fibre end. The corner-cube is calculated to be of 26%, which when compared to the high-reflectivity mirror, corresponds to reflectivity of 63%. This reflectivity takes into account two Fresnel reflections occurring at the input surface and can be corrected by the following formula:

$$R_{CC} = \frac{R_{2,CC}}{(1\text{-}R_{Fresnel})^2} = \frac{R_{2,CC}}{(1\text{-}0.035)^2} \qquad (4.21)$$

$$R_{CC} = 1.07{*}R_{2,CC}$$

Thus the corner-cube reflectivity (Fresnel reflections not included) is of 67% for a focal length of 40mm, a feedback arm length of 240mm and a fibre NA of 0.15.

For an output coupler made from a Fresnel reflection obtained from a flat cleave (i.e. $R_1 = 3.5\%$), Figure 4.16 shows the evolution of the power ratio obtained from equation (**4.15**) as a function of R_2 and values corresponding to the plane mirror and the corner cube are indicated.78%(resp. 85%) of the generated power exited the cavity through the output coupler in the corner-cube configuration (resp. plane mirror configuration).

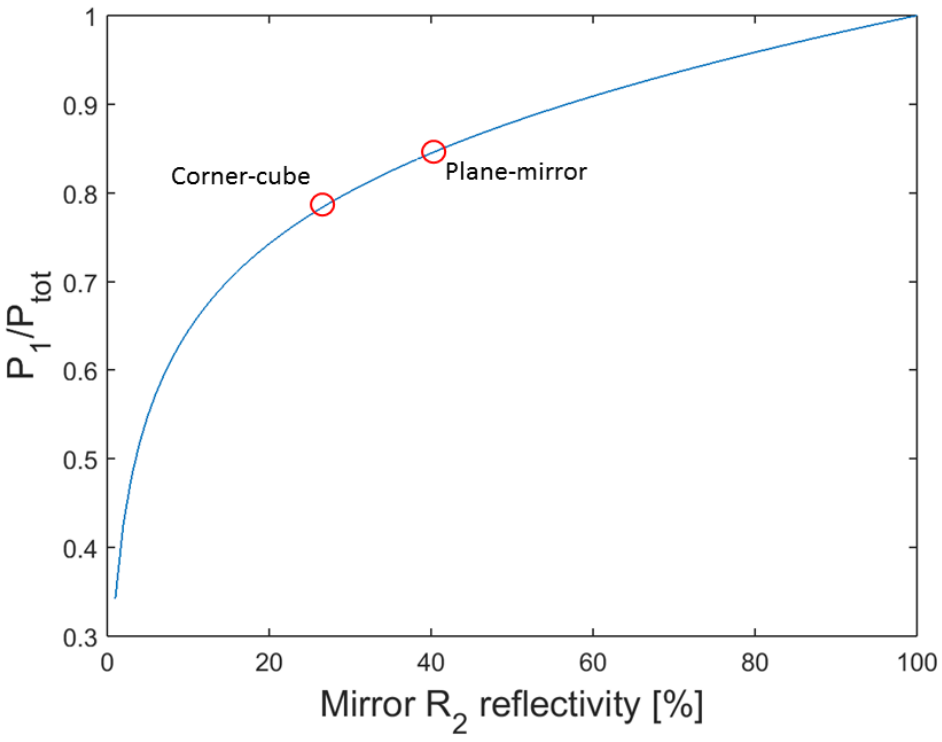

Figure 4.16 Evolution of power exiting through the output coupler as a function of feedback arm reflectivity

4.5 Narrow-band wavelength-tunable thulium fibre ring laser

4.5.1 Introduction

Laser sources with flexibility in operating wavelength have applications in a number of areas including: remote sensing and monitoring, spectroscopy and metrology [4.3-14]. For many of these applications the requirements for wavelength flexibility and good beam quality are very often accompanied by the need for a relatively narrow bandwidth and, in some cases, also by the need for rapid wavelength scanning. Rare-earth doped fibre lasers offer versatility in operating wavelength due to the broad linewidths associated with glass hosts, but simultaneously achieving wavelength agility and a narrow lasing bandwidth is rather challenging.

In a linear cavity, counter-propagating light waves overlap, creating a standing-wave interference pattern with a periodicity of half the lasing wavelength. This creates localised gain saturation at the antinodes of this pattern and hence unused gain at the nodes. Other longitudinal modes that overlap with the undepleted inversion at the modes may then reach lasing threshold broadening the emission linewidth. As a consequence of this spatial hole burning, it is quite challenging to reduce the emission spectrum to one or just a few longitudinal modes, especially in lasers (such as this one) with long cavity lengths. In a unidirectional ring laser, where unidirectional operation is achieved by the use of an isolator no standing-wave interference pattern is created in the gain medium, thus forbidding spatial hole burning to occur. Therefore, single-frequency (or narrow band) operation is more easily achieved in a ring laser by the use of a wavelength-selective element [4.28-31].

4.5.2 Wavelength tuning via fibre tip lateral positioning

Here we combine the idea of a tunable ring laser based on the use of a Fabry-Perot etalon with the alignment insensitivity advantages provided by the use of a corner-cube as reflective element (as previously demonstrated in Section 4.4). Such a fibre laser would yield a relatively narrow wavelength output due to the ring laser configuration whilst the Fabry-Perot etalon combined with the corner-cube as retro-reflector offers the possibility of rapid wavelength scanning. Tuning for this configuration is commonly achieved by rotation of the Fabry-Perot etalon, modifying its round-trip distance [4.29, 30]. Similar round-trip distance modification can be achieved by in an external cavity configuration containing a corner-cube by lateral translation of the fibre tip which in turn changes the angle of the collimated light passing through the etalon, modifying its transmission spectrum. This usually leads to high losses when moving the fibre tip by more than the core radius (see Figure 4.12). The use of a corner-cube allows us to avoid of this limitation, permitting accurate and rapid tuning by fibre translation whilst conserving high feedback efficiency.

4.5.3 Experimental setup

Figure 4.17 shows the laser set-up employed comprising a 2.5m length of single-mode Tm-doped alumino-silicate fibre as the gain medium. The fibre, fabricated in-house, had a 10 μm diameter core with a numerical

aperture of 0.15 and 0.2wt% Tm concentration. Pump light was provided by a 1565 nm Er,Yb fibre laser coupled directly into the Tm fibre core via a 1565/1900nm WDM. Unidirectional lasing was achieved using a circulator and an isolator with wavelength discrimination provided by the external cavity. A 3dB tap-coupler followed by an angle polished connector was used as the output coupler. Wavelength tuning was achieved by simply adjusting the lateral position of the angled fibre end facet adjacent to the feedback cavity collimating lens; this lens was a 40mm plano-convex anti-reflection coated at 2µm. This movement adjusts the angle of incidence of the beam on the etalon and hence the wavelength of its transmission peak (see Chapter 2). The laser operates on the transmitted wavelength closest to the gain peak for the Tm fibre. The beam is automatically fed back by the corner-cube retro-reflector at precisely the same angle without the need of adjustment, ensuring excellent re-coupling of the light transmitted by the etalon into the fibre. Thus, the tuning mechanism is equivalent to adjusting the angle of the etalon, but is achieved in a much more straightforward manner with complete immunity to misalignment.

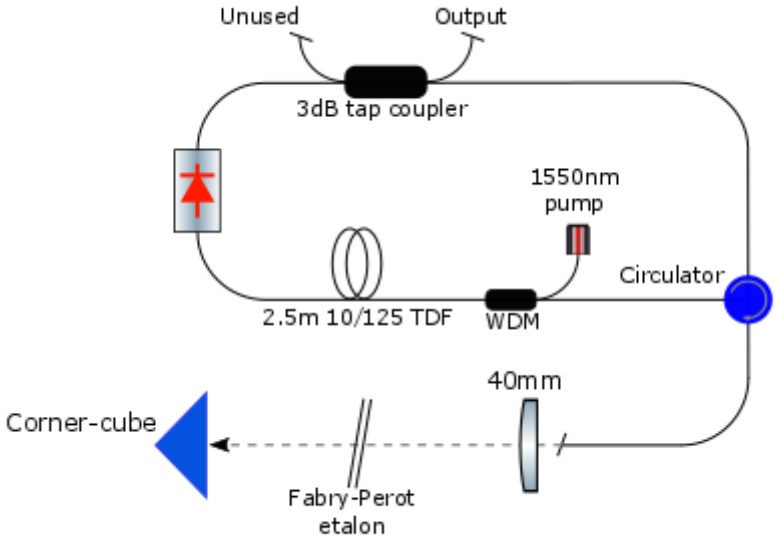

Figure 4.17 Ring laser setup containing a Fabry-Perot etalon with a corner-cube for wavelength-tuning.

4.5.4 Theoretical expectations on wavelength tuning

Calculations on the tuning rate of this configuration as a function of lateral fibre tip movement was carried out. The system comprised a 40mm focal collimating lens in the feedback arm, yielding a beam radius of f.NA=12mm. Tolerances on fibre tip movement are also a function of the distance between the corner-cube and the collimating lens as explained previously. However, for a chosen collimating lens, a fixed lateral movement of the fibre tip in the focal plane will lead to a particular angular change of the beam path, thus leading to wavelength-tuning of the laser. Figure 4.18 illustrates the wavelength selection arm utilised in this setup. Here the feedback arm length was kept to a minimum to avoid high reflectivity drops when transversally moving the fibre tip.

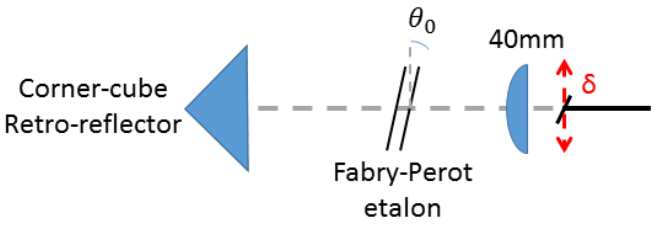

Figure 4.18 Schematic of the wavelength-tuning arrangement.

For an etalon at an angle θ_0 compared to the input beam with a spacing d, the round-trip distance L is:

$$L = \frac{2d}{\cos\theta_0} \tag{4.22}$$

There is high transmission for wavelengths where the phase difference is:

$$\frac{2\pi L}{\lambda} = 2q\pi \tag{4.23}$$

With q an integer, leading to

$$\lambda = \frac{L}{q} = \frac{2d}{q\cos\theta_0} \tag{4.24}$$

Here, the beam hitting the Fabry-Perot will arrive with an angle θ_δ dependent on θ_0, f and δ:

$$\theta_\delta = \theta_0 + \frac{\delta}{f} \tag{4.25}$$

This changes the round-trip distance L which will modify the output wavelength (CF 2.5.5):

$$\lambda_\delta = \frac{L}{q} = \frac{2d}{q\cos\theta_\delta} \tag{4.26}$$

After measurement of the output wavelength for δ=0, we obtain:

$$\lambda_\delta = \lambda_0 \frac{\cos(\theta_0)}{\cos\left(\theta_0 + \frac{\delta}{f}\right)} \tag{4.27}$$

Wavelength tuning ratio as a function of fibre tip movement is then

$$\frac{d\lambda}{d\delta} = \frac{\lambda_0\cos(\theta_0)}{f} \cdot \frac{\sin\left(\theta_0 + \frac{\delta}{f}\right)}{\cos^2\left(\theta_0 + \frac{\delta}{f}\right)} = \frac{\lambda_0\cos(\theta_0)}{f} \cdot \frac{\tan\left(\theta_0 + \frac{\delta}{f}\right)}{\cos\left(\theta_0 + \frac{\delta}{f}\right)} \tag{4.28}$$

As the fibre tip movement is quite small compared to the focal length of the collimating lens used here and θ_0 is a small angle, one can approximate:

$$\tan\left(\theta_0+\frac{\delta}{f}\right)\approx\left(\theta_0+\frac{\delta}{f}\right)\ \&\cos\left(\theta_0+\frac{\delta}{f}\right)\approx 1+\frac{\left(\theta_0-\frac{\delta}{f}\right)^2}{2}$$

Therefore equation (**4.28**) becomes

$$\frac{d\lambda}{d\delta}\approx\frac{\lambda_0}{f}.\left(1+\frac{\theta_0}{2}\right).\frac{\theta_0+\frac{\delta}{f}}{1-\frac{\left(\theta_0+\frac{\delta}{f}\right)^2}{2}} \tag{4.29}$$

And can be approximated further to

$$\frac{d\lambda}{d\delta}\approx\frac{\lambda_0}{f}.\left(\theta_0+\frac{\delta}{f}\right) \tag{4.30}$$

Figure 4.19 shows the evolution of $\frac{d\lambda}{d\delta}$ for a starting angle of 10 degrees and a central wavelength of 1870nm for both equations (**4.28**) and (**4.30**). $\frac{d\lambda}{d\delta}$ has a quasi-linear evolution due to $\theta_0+\frac{\delta}{f}$ being quite a small value for typical lateral movement tolerances. It was previously demonstrated that in this configuration the fibre tip can be moved by ±1mm, corresponding to an angle change of ±1.4°, leading to a maximum input angle of 11.4°, allowing small angle approximations.

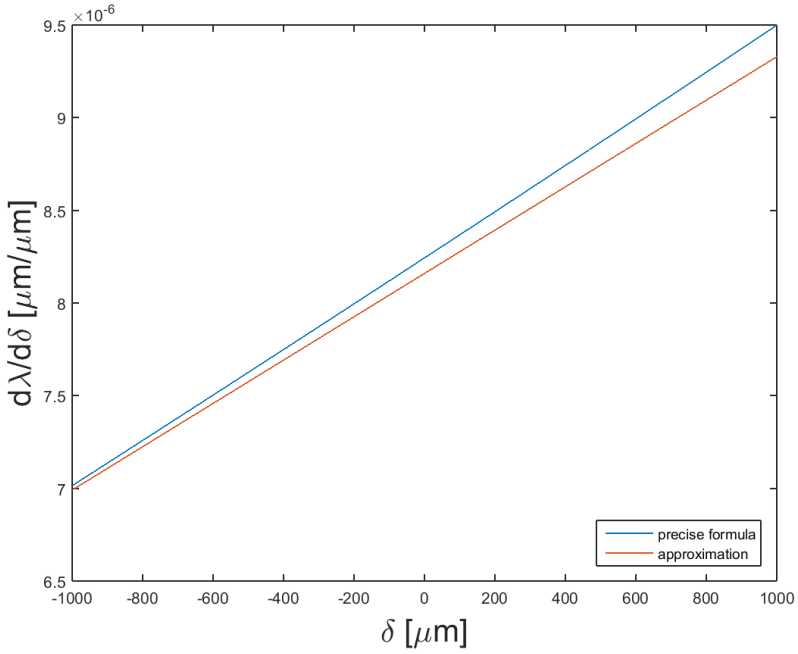

Figure 4.19 Theoretical evolution of $\frac{d\lambda}{d\delta}$ in a tunable ring laser

Figure 4.20 shows the evolution of λ as a function of fibre tip movement for both equations for an output wavelength of 1870nm when δ=0. From both equations (**4.28**) and (**4.30**) similar results are obtained, confirming the assumptions made in equation (**4.29**) and leading to:

$$\lambda(\delta) \approx \frac{\lambda_0 \delta}{f}.\left(\theta_0 + \frac{\delta}{2f}\right) + \lambda_0 \qquad (4.31)$$

The wavelength evolution therefore depends on the initial input angle and the angle change applied $\frac{\delta}{f}$ by moving the fibre tip. This corresponds, for a starting Fabry-Perot angle of 10°, to a tuning of 8pm/µm (0.7GHz/µm) around the central point for a starting output wavelength of 1870nm. As we demonstrated earlier lateral fibre tip movement of ±1mm whilst keeping high feedback efficiency, up to ±8nm of tuning can theoretically be achieved.

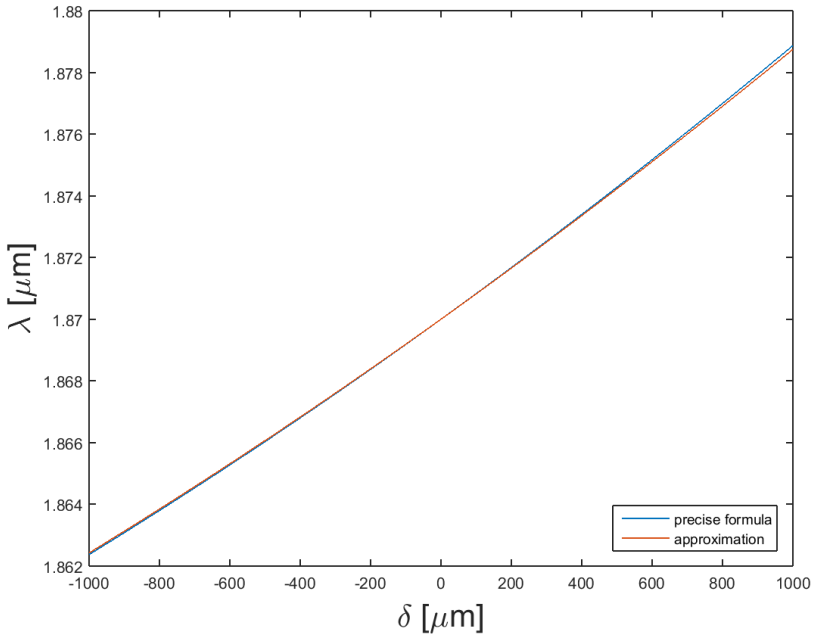

Figure 4.20 Theoretical evolution of λ in the tunable ring laser as a function of transverse fibre tip movement

4.5.5 Experimental results

Tuning is shown in Figure 4.21 where output wavelength is plotted as a function of fibre tip position. Movement of ±500µm was achieved during tuning whilst maintaining similar output power. Tuning was performed for two different Fabry-Perot spacings, corresponding to two different free spectral ranges. Continuous linear tuning over zones of 1.5nm was achieved, separated by wavelength jumps of tens of nanometers.

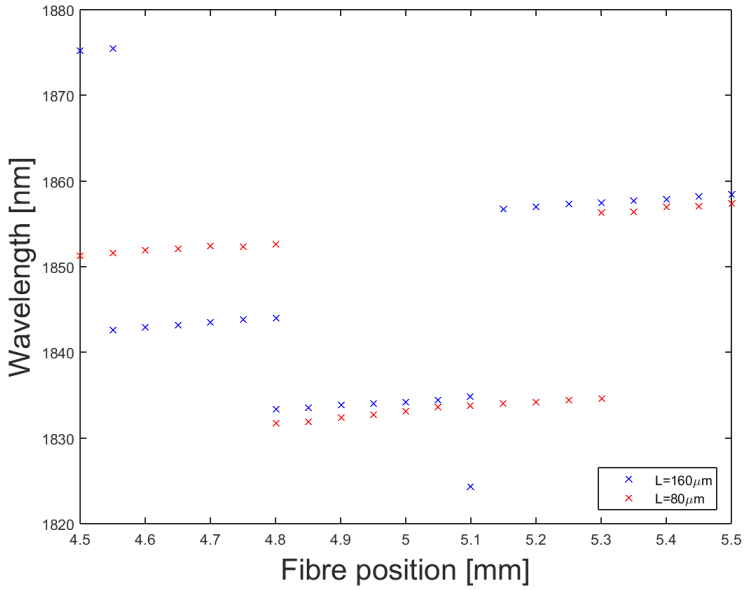

Figure 4.21 First result of wavelength-tuning by fibre tip translation with two etalon spacings of 80 and 160µm

These jumps were attributed to mode hopping of the laser with the wavelength jumps corresponding to a spacing of one or more FSRs. The FSR Δν is dependent on the spacing of the two mirrors of the etalon L:

$$\Delta\nu = \frac{c}{2L} \tag{4.32}$$

For two neighbouring longitudinal modes of wavelengths λ_1 &λ_2, each has a frequency ν_1 &ν_2 with:

$$\nu = \frac{c}{\lambda} \tag{4.33}$$

Therefore

$$\Delta\lambda \approx \frac{\lambda_2^2}{2L} \tag{4.34}$$

The table below shows the FSR value in nm for different etalon spacings:

Etalon spacing [µm]	Δλ [nm]
10	171.1
20	85.6
40	42.8
80	21.4
160	10.7

Table 4-2 Free-spectral range evolution [nm] as a function of Fabry-Perot etalon spacing

Jumping of multiples of 10nm (resp. 20nm) were observed for an etalon of 160µm (resp. 80µm) and fit perfectly with the corresponding FSR values. In this system, as the active fibre has a broad gain region, when wavelength-tuning reaches a wavelength having higher losses than usual (due to water vapour absorption or losses in the

circulator for example), the cavity jumps onto a neighbouring mode which has higher overall round trip gain. For a really short FSR in wavelength, this jump can be of more than one free-spectral range at a time.

To avoid this mode-hopping, one has to ensure the neighbouring modes are spectrally far enough to have a much lower gain even when crossing a wavelength having higher loss than usual. Two different approaches are available: either increasing the FSR (in wavelength) so that neighbouring modes are far enough from the lasing wavelength and have low gain or artificially increasing losses of the neighbouring modes, even when close to the lasing wavelength by using narrow-band filters with a transmission bandwidth smaller than the free-spectral range. Here we decided to achieve this is by increasing the free spectral range (FSR) of the Fabry-Perot etalon through reduction of the etalon spacing.

Figure 4.22 shows tuning for an etalon spacing of 20µm corresponding to a FSR of more than 80nm. Tuning is achieved over more than 2.5nm without mode-hopping compared to previously when mode-hopping occurred after less than 1.5nm of tuning. This tuning was achieved from 1874.8 to 1877.5nm, a zone where mode-hopping was previously occurred according to the results shown in Figure 4.21. This proves that no mode-hopping occurs in this cavity as tuning was obtained in a previously unavailable wavelength zone. A tuning of 2.7nm over a 400µm movement corresponds to a tuning of 6.5pm/µm, which here gives a θ_0 of 7.9 degrees.

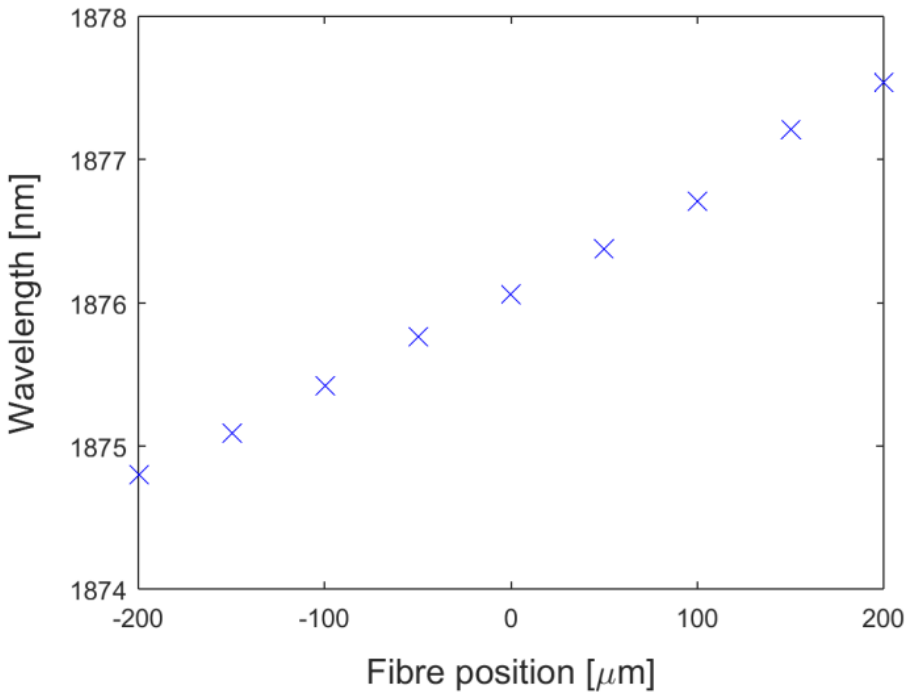

Figure 4.22 Final result showing quasi-continuous tuning by fibre tip movement

Linewidth of the output was studied by the use of a scanning Fabry-Perot interferometer which consists in a Fabry-Perot etalon with one of the mirrors mounted on a piezo-actuator to scan the output modes. The piezo-actuator was chosen to have a movement amplitude of more than half a wavelength, to ensure modulation of the round-trip distance in the scanning Fabry-Perot etalon of more than one wavelength. The etalon was adjusted to have a large spacing, decreasing the FSR and therefore improving resolution. Figure 4.23 shows such

a measurement; the red curve shows the piezo voltage (i.e. the piezo movement) whilst the cyan one represents the laser output obtained by a high-speed photodiode and the green one is the transmission of the scanning Fabry-Perot. Here the scanning Fabry-Perot spacing was of 15mm leading to an FSR Δν of:

$$\Delta\nu = \frac{c}{2L} = 10\text{GHz} \tag{4.35}$$

As the piezo-actuator has a movement of 1.5µm, the round-trip distance is modulated by ±1.5µm. Thus each transmission peak can have a repetition when scanning due to the round-trip distance being modulated by more than one wavelength. This allows us to calibrate the measurement obtained knowing that the distance between a transmission peak and its repetition is one FSR. From the width of the peaks the maximum linewidth of the output spectrum can be determined. Here the linewidth seems to be lower than 1.5GHz. The actual linewidth is probably much lower than reported here we believe are resolution-limited by the finesse of the scanning FP. The etalon finesse depends on alignment and reflectivity of the mirrors, which here was of 90%. From the measurement carried out on Figure 4.23, a finesse of 8 was calculated.

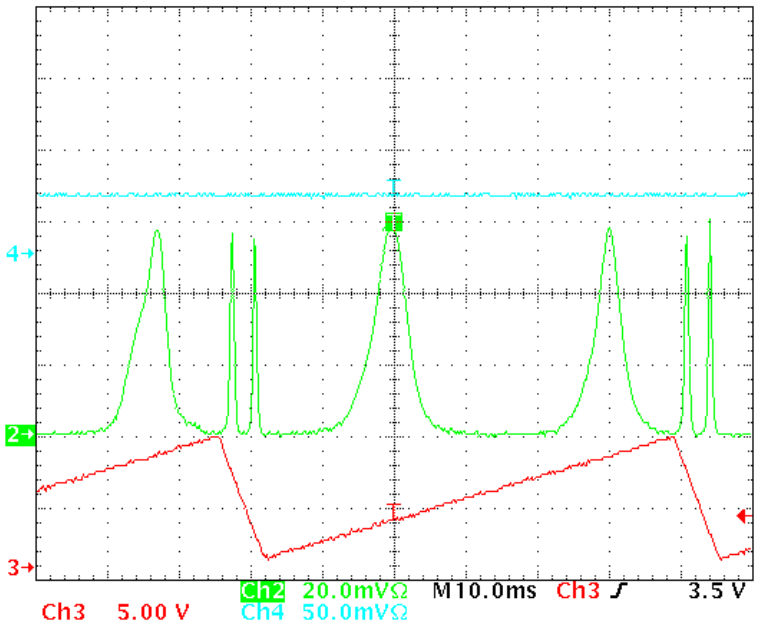

Figure 4.23 Linewidth measurement by the use of a scanning Fabry-Perot interferometer.

4.5.6 Limitations on continuous wavelength tuning

One of the main issues of this system is random mode-hopping forbidding continuous tuning which required a high FSR (i.e. Fabry-Perot spacing of tens of microns maximum). Such a problem can be avoided by the addition of a narrow-bandpass filter to forbid neighbouring modes from co-lasing. Avoiding mode-hopping can be realised by having a bandpass filter with a broader transmission band than the desired tuning and an etalon free-spectral range higher than the filter transmission band. Considering a maximal fibre tip movement of ±1mm, a maximal wavelength tuning of 15nm can be achieved at 1900nm. An appropriate bandpass filter would have a bandwidth slightly wider than the tuning range of around 20nm coupled with an etalon FSR higher in

wavelength than this value. From equation (**4.34**) a quick calculation shows that an etalon spacing shorter than 85µm is sufficient to forbid mode-hopping inside the bandwidth of the bandpass filter.

Moreover, slight variations from theoretical expectations were observed when achieving wide tuning. Even though mode hopping does not occur, slight discrepancies can happen when the selected wavelength corresponds to a high loss, e.g. from an atmospheric absorption line. Figure 4.24 shows broader tuning over 5.1nm ,obtained by using the setup previously described in Figure 4.17, compared to a simulation obtained from equation (**4.27**) for a starting wavelength and angle of 1877nm and 10 degrees respectively. A slight jump was observed between 1877.5 and 1878.5nm. This does not correspond to mode-hopping as the etalon spacing used here was of 20µm corresponding to an 80nm value for mode-hopping. We believe that during tuning, when reaching a wavelength having a higher loss than usual, the system will tend to mode hop in order to operate at the highest gain wavelength and, by forbidding it, the system will slightly shift the output wavelength while remaining inside the transmission peak of the Fabry-Perot to maximise overall gain. The transmission linewidth of the etalon is a function of the mirrors reflectivity, increasing when the reflectivity decreases. Here, the mirrors have a reflectivity lower than 85% at the operating wavelength, leading to broader transmission peaks as detailed in Section 2.5.5 and shown in Figure 2.12, promoting significant wavelengths shifts in order to avoid low gain wavelengths as observed in Figure 4.24. From a comparison of experimental and theoretical curves, it can be deduced that a nanometre-wide absorption peak (either due to a particular gas in the atmosphere or from one of the components used) is situated around 1878nm.

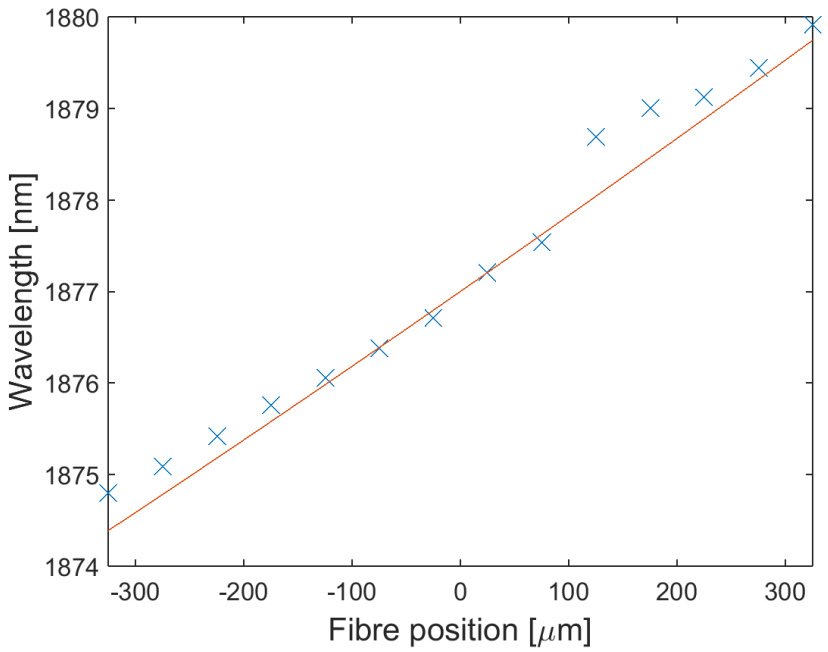

Figure 4.24 Broad tuning of a ring laser over more than 5nm by fibre tip lateral movement showing nanometre broad jump

4.6 Conclusion

We have investigated a novel way of improving insensitivity to misalignment in a fibre laser external feedback cavity, exploiting the advantages of a corner-cube over a plane mirror as reflective element. Improvement of transverse fibre tip misalignment insensitivity was increased from 10µm up to more than a millimetre in some of the resonator configurations described in this chapter.

Theoretical calculations were carried out to characterise external cavity feedback efficiency as a function of focal lens and feedback arm length, showing a wide stability zone for a feedback arm length of 2f. Two situations can be defined from equation (**4.3**): for long feedback arms, transverse misalignment tolerances increase heavily by changing the focal length, with $\delta_{\max} \propto f^2$ and for short ones $\delta_{\max} \propto f$ for short ones.

Simulations showing the feedback efficiency as a function of feedback arm length and displacement for two kinds of beam profiles (top-hat and Gaussian) were presented with explanations of the differences between each beam profile, the first one corresponding to a first approximation whilst the second one corresponding to accurate calculation. A discrepancy of up to 10% higher feedback efficiency for the Gaussian profile when laterally translating the fibre tip was showed between both simulations.

Experimental verification showed the dependence of the movement tolerances to collimating lens and free-space path length. By changing the reflective element, tolerances were increased from a typical fibre core diameter distance (here 10µm) to millimetre level, showing improvement by more than two orders of magnitude. Improvement becomes particularly significant for long focal length and short feedback arm lengths as summarised in Figure 4.11 and Figure 4.13. Results were compared with theoretical expectations from equations (**4.3**) and (**4.8**) and good match between experiment and theory was obtained, validating the simulations. A maximum experimental tolerances of 1.2mm was demonstrated for a configuration d=f=40mm and this setup's maximum fibre tip transverse movement $\delta_{\max}$ is only limited by the translation stage used movement out of the focal plane. Any transverse movement of the fibre tip in front of the collimating lens leads to a variation of focal length along both axis x and y and thus movement out of the focal plane. Maximal acceptable movement in the focal plane was calculated by using ABCD matrices and showed a tolerance of 20µm which might be the limiting factor for transverse movement tolerances.

A calculation of the corner-cube experimental reflectivity was done from output power comparison between two configurations comprising either a plane mirror or a corner-cube, resulting in an effective reflectivity of more than 70% (including the loss due to two Fresnel reflections). Corner-cube reflectivity is quite low because of unwanted scattering occurring at the edges and the apex of the retro-reflector but can be minimised by using a higher quality element. High slope efficiency can still easily be achieved in fibre laser whilst using a corner-cube as fibre lasers are quite forgiving of intra-cavity losses due to their high gain. Therefore, more complicated systems with non-negligible intra-cavity loss can be considered while still operating with high slope efficiency by utilising a high quality anti-reflection coated corner-cube.

We demonstrate wavelength tuning by fibre tip positioning by utilising this new feedback arm architecture coupled with a Fabry-Perot etalon in a ring laser configuration. A simulation was carried out, showing a tuning expectation of around 8pm/µm for an initial Fabry-Perot angle of incidence of 10 degrees. Coupled with the tolerances on fibre tip movement described earlier of at least ±1mm, overall tuning of ±8nm was expected.

Tuning was experimentally performed over 5nm centred at 1870nm with a linewidth lower than 1.5GHz. Mode-hopping was suppressed through reduction of the etalon free spectral range to achieve continuous tuning but slight discrepancies between theoretical and experimental measurements still remained (up to 0.5nm). These wavelength shifts corresponded to self-adjustment of the output wavelength inside the transmission peak of the Fabry-Perot etalon to operate at the wavelength achieving the highest gain. High reflectivity mirrors can be used to increase finesse and reduce transmission linewidth of the etalon in order to achieve quasi-linear tuning following equation (**4.27**). This system offered accurate tuning based on fibre tip movement and had the capability for more than 15nm tuning around 1870nm. A trade-off can be made to improve tuning range by changing feedback arm length and collimating lens, therefore allowing broader fibre tip lateral movement. This system has the capability for rapid accurate tuning of the laser due to the lightweight of the moving element compared to rotation of the Fabry-Perot etalon; this allows for fast wavelength-scanning required in specific applications such as OCT or LIDAR.

4.7 References

4.1. T. Ehrenreich, et al., *1-kW, all-glass Tm:fiber laser*, in Fiber Lasers VII: Technology, Systems, and Applications (2010) (Session 16: Late breaking news). 2010.

4.2. Richardson, D.J., J. Nilsson, and W.A. Clarkson, *High power fiber lasers: current status and future perspectives*. Journal of the Optical Society of America B-Optical Physics, 2010. **27**(11): pp. B63-B92.

4.3. Mingareev, I., et al., *Welding of polymers using a 2µm thulium fiber laser*. Optics and Laser Technology, 2012. **44**(7): pp. 2095-2099.

4.4. Kadwani, P., et al., *Atmospheric absorption spectroscopy using Tm: fiber sources around 2 microns*. Atmospheric and Oceanic Propagation of Electromagnetic Waves V, 2011. **7924**.

4.5. Kadwani, P., et al., *Atmospheric gas detection using broadband mid-IR thulium fiber-based sources*. Laser Technology for Defense and Security Vii, 2011. **8039**.

4.6. Theisen, D., et al., *Cw high power IR-laser at 2µm for minimally invasive surgery*. Therapeutic Laser Applications and Laser-Tissue Interactions, 2003. **5142**: pp. 96-100.

4.7. Jelinkova, H., et al., *Diode-pumped Tm : YAP laser for eye microsurgery* - art. no. 68712N. Solid State Lasers Xvii: Technology and Devices, 2008. **6871**: pp. N8712-N8712.

4.8. Shi, W., et al., *Fiber lasers and their applications [Invited]*. Applied Optics, 2014. **53**(28): pp. 6554-6568.

4.9. Gagliardi, G., et al., *High-precision determination of the (CO2)-C-13/(CO2)-C-12 isotope ratio using a portable 2.008μm diode-laser spectrometer*. Applied Physics B-Lasers and Optics, 2003. **77**(1): pp. 119-124.

4.10. Alexander, V.V., et al., *Photothermolysis of Sebaceous Glands in Human Skin Ex Vivo with a 1,708 nm Raman Fiber Laser and Contact Cooling*. Lasers in Surgery and Medicine, 2011. **43**(6): pp. 470-480.

4.11. De Young, R.J. and N.P. Barnes, *Profiling atmospheric water vapor using a fiber laser lidar system*. Applied Optics, 2010. **49**(4): pp. 562-567.

4.12. Scott, N.J., et al., *Thulium Fiber Laser Ablation of Urinary Stones Through Small-Core Optical Fibers*. Ieee Journal of Selected Topics in Quantum Electronics, 2009. **15**(2): pp. 435-440.

4.13. Li, Z., et al., *Thulium-doped fiber amplifier for optical communications at 2μm*. Optics Express, 2013. **21**(8): pp. 9289-9297.

4.14. Barnes, N.P., et al., *Tm:fiber lasers for remote sensing*. Optical Materials, 2009. **31**(7): pp. 1061-1064.

4.15. Blomqvist, M., et al., *Fundamental-mode fiber-to-fiber coupling at high-power*. Solid State Lasers Xviii: Technology and Devices, 2009. **7193**.

4.16. Wallner, et al., *Alignment tolerances for plane-wave to single-mode fiber coupling and their mitigation by use of pigtailed collimators*. Applied Optics, 2002. **41**(4): pp. 637-643.

4.17. Wang, H.S., et al., *Coherent Properties of Corner Cube Resonator Laser.* 2010 International Conference on Display and Photonics, 2010. **7749**.

4.18. Shih, C.C., *Depolarization effect in a resonator with corner-cube reflectors*. Journal of the Optical Society of America a-Optics Image Science and Vision, 1996. **13**(7): pp. 1378-1384.

4.19. Mayer, J.R.R., *Polarization Optics Design for a Laser Tracking Triangulation Instrument Based on Dual-Axis Scanning and a Retroreflective Target*. Optical Engineering, 1993. **32**(12): pp. 3316-3326.

4.20. Player, M.A., *Polarization Properties of a Cube-Corner Reflector*. Journal of Modern Optics, 1988. **35**(11): pp. 1813-1820.

4.21. Peck, E.R., *Polarization Properties of Corner Reflectors and Cavities**. Journal of the Optical Society of America, 1962. **52**(3): pp. 253-257.

4.22. Hege, G. and K. Leonhardt, *POLARIZATION PROPERTIES OF CUBE-CORNERS - PRESENTATION OF EXPERIMENTALLY VERIFIED MATRICES*. Optik, 1977. **47**(2): pp. 167-184.

4.23. Shen, M.X., et al., *Mode properties produced by a corner-cube cavity*. Applied Optics, 2004. **43**(20): pp. 4091-4094.

4.24. Zhou, G., A.J. Alfrey, and L.W. Casperson, *Modes of a Laser Resonator with a Retro-Reflecting Corner Cube Mirror*. Applied Optics, 1982. **21**(9): pp. 1670-1674.

4.25. Tsumura, T., H. Okubo, and N. Komatsu, *A 3-D Position and Attitude Measurement System Using Laser Scanners and Corner Cubes*. Iros 93 : Proceedings of the 1993 Ieee/Rsj International Conference on Intelligent Robots and Systems, Vol 1-3, 1993: pp. 604-611.

4.26. Tsumura, T., *Optical two-way vehicle-to-vehicle communication by the use of laser and corner cube*. Robotics and Autonomous Systems, 1996. **17**(1-2): pp. 81-86.

4.27. Komatsu, N., *Positioning and guidance of highway vehicle by series of corner-cube set on guard rail.* Ieee Conference on Intelligent Transportation Systems, 1997: pp. 769-774.

4.28. Liem, A., et al., *100-W single-frequency master-oscillator fiber power amplifier*. Optics Letters, 2003. **28**(17): pp. 1537-1539.

4.29. Park, N., et al., *All Fiber, Low Threshold, Widely Tunable Single-Frequency, Erbium-Doped Fiber Ring Laser with a Tandem Fiber Fabry-Perot Filter*. Applied Physics Letters, 1991. **59**(19): pp. 2369-2371.

4.30. Vahala, K.J., et al., *Tunable, Single-Frequency, Erbium Fiber Ring Lasers*. Leos '93 Conference Proceedings, 1993: pp. 708-709.

4.31. Iwatsuki, K., H. Okamura, and M. Saruwatari, *Wavelength-Tunable Single-Frequency and Single-Polarization Er-Doped Fiber-Ring Laser with 1.4 Khz Linewidth*. Electronics Letters, 1990. **26**(24): pp. 2033-2035.

Chapter 5. Digital Micro-mirror Device-controlled wavelength tunable thulium laser

5.1 Introduction

Over the last decade there has been increasing interest in two-micron fibre lasers motivated by the needs of a growing number of applications. The most popular gain medium is thulium (Tm) doped silica glass which offers access to a wide range of operating wavelengths, due to its very broad emission spectrum, spanning the range from <1.7 µm to >2.1 µm. This spectral regime overlaps with an atmospheric transmission window, water vapour and carbon dioxide absorption lines (Figure 5.1), a strong liquid water absorption band and a C-H bond overtone. Thus two-micron lasers have applications in areas such as free-space communications [5.1], LIDAR and differential absorption LIDAR [5.2-4], spectroscopy [5.5], laser surgery [5.6-8], laser processing of plastics [5.9], and so on.

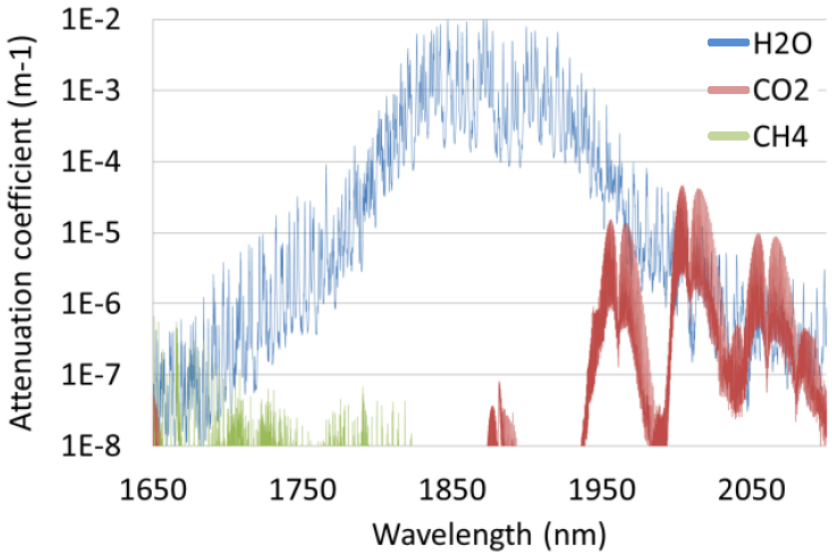

Figure 5.1 Atmospheric absorption bands of several gas species in concentrations typically found in the atmosphere, data from: [5.10].

For many of these applications, the requirement for high laser power can be met by employing a cladding-pumped fibre laser architecture based on Tm-doped silica. One advantage of operating fibre lasers in the two-micron band is that a larger core size can be employed whilst still maintaining robust single-mode operation compared to the situation with near-infrared Yb-doped fibre lasers operating in the one-micron band. This increases the threshold for deleterious nonlinear loss processes (e.g. stimulated Raman scattering (SRS) and stimulated Brillouin scattering (SBS)) and increases the core damage threshold, opening up the possibility of higher average powers. A further attraction of operating in the two-micron band, owing to the strong water absorption, is that the maximum permissible exposure limit (i.e. before the onset of eye damage) are dramatically high than at one-micron, easing deployment of two-micron lasers in demanding environments.

Different operating wavelengths are needed depending on the application targeted thus wavelength flexibility and, in some cases, rapid wavelength tuning are key pre-requisites for the laser design to further develop these applications.

Different methods are available to realise wavelength selection and tuning in Tm fibre lasers. A diffraction grating as an external feedback element provides a wide tuning range with a relatively narrow lasing line but requires mechanical adjustment of the grating's angle [5.11], leading to relatively slow tuning rates. Wavelength tuning can also be achieved using on an acousto-optic tunable filter (AOTF). This offers high speed tunability and a large wavelength range [5.12-14], but AOTFs are generally polarisation sensitive devices, therefore requiring polarization maintaining (PM) fibres to achieve good feedback efficiency. Additionally, narrow-band wavelength selection cannot be achieved with commercially available AOTFs as they offer a transmission bandwidth in the order of few nanometers at full-width at half maximum (FWHM). Lastly, they require a constant radio frequency (RF) signal and hence a continuous supply of electrical power.

However, wide wavelength tunability and high speed can be achieved by the using MEMS combined with a fixed diffraction grating as feedback element. This configuration was recently reported using a wavelength dependent feedback arrangement based on a digital micromirror device (DMD) in a ring cavity with a core-pumped Tm-doped fibre laser [5.15] yielding wavelength switching times as short as 75 µs, a maximum output power of 160mW and a tuning range of 74 nm.

In this chapter, we described a wavelength-tunable Tm-doped fibre laser with a linear cavity and feedback provided by a DMD and diffraction grating with up to 8.5 W of output power and a much wider tuning range of 131 nm. Our scheme also offers access to multiple wavelengths with control of relative powers.

5.2 Design of a DMD-controlled wavelength-tunable Tm-doped single mode fibre laser

5.2.1 Introduction

Rapid accurate wavelength-tuning is often required for many applications utilising fibre lasers. Such tuning can easily be achieved by inserting a diffraction grating in the laser cavity feedback arm, providing wavelength-selective feedback either in a Littrow or Littman-Metcalf configuration (see Chapter 2). However, tuning via a diffraction grating is based on grating rotation which is quite slow or fibre tip transverse movement (see Chapter 4) which is not easily controlled at high speed. Thus, a component allowing to create an adjustable reflective pattern, combined with a diffraction grating, would permit quick, reliable wavelength-tuning, easily switching from one wavelength to another by only modifying a reflection pattern. Figure 5.2 shows a feedback arm design combining an imaging with a diffraction grating along the y axis and DMD consisting in a matrix a micro-mirrors. As a consequence, wavelengths are angularly distributed in the xz plane and are focused by the second lens onto

the DMD, imaging the fibre core with a spatial wavelength chirp. The DMD offers computer-controlled mirror positioning, allowing to select which wavelengths to feedback into the cavity.

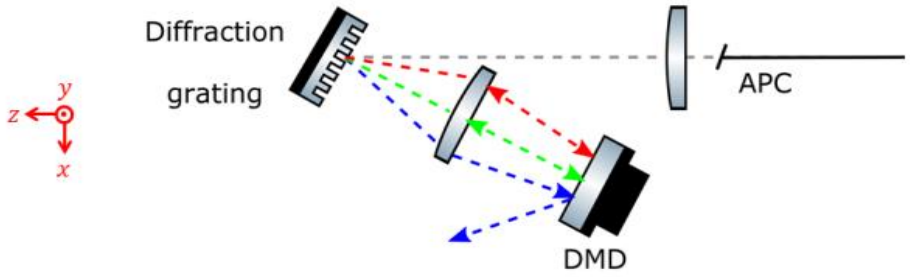

Figure 5.2 Feedback arm design composed of a diffraction grating and a DMD offering wavelength-selective feedback

5.2.2 Experimental setup

Figure 5.3 shows the schematic of the laser set-up. The cavity was formed by a perpendicular fibre facet cleave acting as the output coupler providing a 3.5% reflectivity from a Fresnel reflection and by an external feedback arm. Pump power was free space-coupled from a 35W laser diode with a core (resp. cladding) diameter of 105µm (resp. 125µm) and a core NA of 0.22 emitting at 793 nm into the gain medium which was a Tm-doped fibre with a 2 wt% concentration, 0.15 NA, a 10.5µm core diameter (d_{core}) and a D-shaped 125µm inner-cladding fabricated in-house.

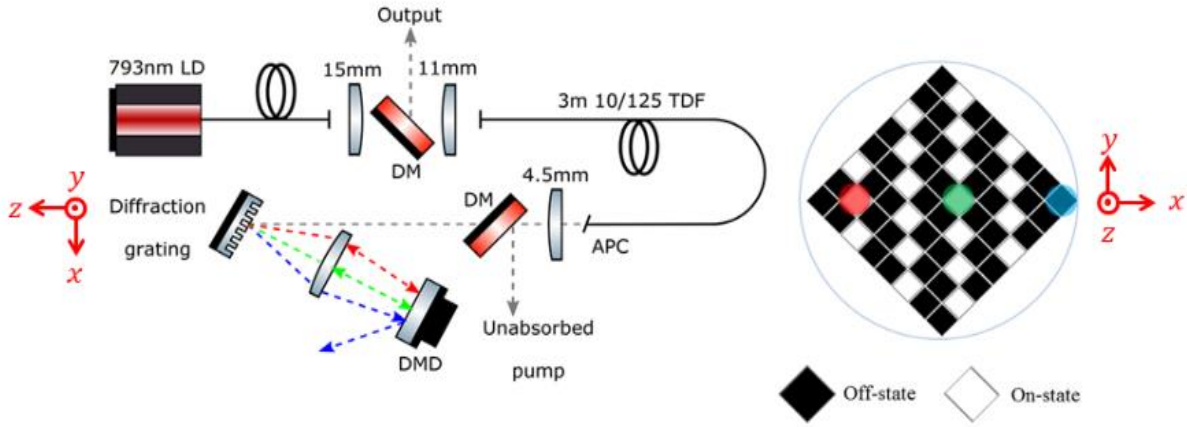

Figure 5.3 Schematic of a the tunable Tm-doped fibre laser with a DMD-tuned extended feedback arm.

The external feedback cavity contained a diffraction grating along the y axis (600lines/mm) blazed at 35°, a DMD and two anti-reflection coated lenses imaging the fibre core onto the DMD. Exiting the active fibre through an 8° angle-cleave, the beam is collimated by the first lens and diffracted by the grating, spatially chirping it along the x axis.

The DMD (Texas Instruments DLP 4000) is utilised in conjunction with a diffraction grating to provide wavelength-selective feedback. The DMD consists of a matrix of 1024 by 768 addressable square silver mirrors

with a size of 13.68µm (corresponding to a diagonal dimension $d_m = 19.35\mu m$) and a protective glass window coated for near infrared wavelengths. The DMD mirrors reflectivity around 2µm is ≈70%, taking into account the protective window transmission, the fill-factor and mirror reflectivity. Each mirror offers two stable angular positions shown in Figure 5.4 at +12° and -12° (here called "on-state" and "off-state" respectively) through two actuators which determine the direction of the reflected light. As the actuators on each mirror are positioned on two opposite corners, the device needs to be tilted by 45° to obtain the y axis as axis of rotation (see Figure 5.4). One position will be used to feed the light back into the cavity (“on-state”) whilst the other will reject the beam (“off-state”). The DMD reflectivity pattern can be controlled by assigning an "on-state" to the desired pixels which define a wavelength-dependent reflectivity spectrum for the external feedback cavity.

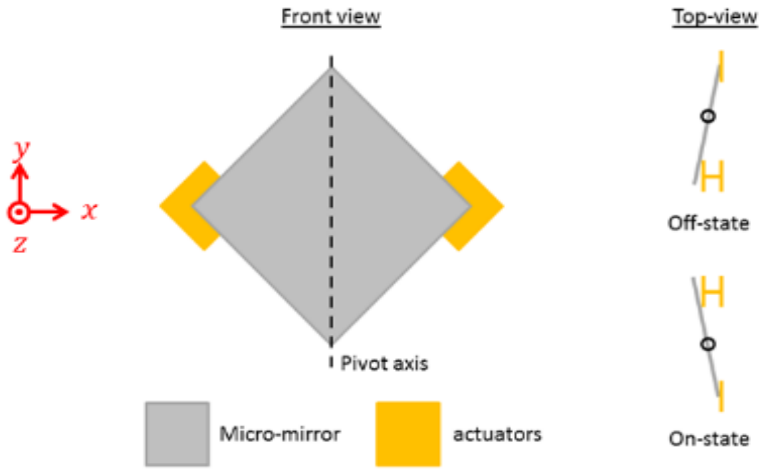

Figure 5.4 ON and OFF positions of the pixels on the DMD

5.2.3 Theory

The horizontal width D of the DMD in a diamond-shape configuration is dependent on the number of mirrors and the mirror’s diameter with here a value D of 14.86mm.

The beam is imaged onto the DMD and, for a single wavelength assuming the focal lengths are independent of wavelength, has a diameter $d_i$corresponding to:

$$d_i = \frac{f_2}{f_1} d_{core} \tag{5.1}$$

Where $f_1 = 4.5\text{mm}$ and $f_2 = 150\text{mm}$, giving $d_i = 350\mu m \approx 36\text{pixels}$.

Each wavelength is diffracted by the grating at a different angle according to:

$$\theta_{out} = \sin^{-1}\left(\frac{m\lambda}{\delta} - \sin\theta_{in}\right) \tag{5.2}$$

Where m is the diffracted order, θ_{in} and θ_{out} the incident and diffracted angles (with respect to the grating's normal as a reference), and δ the spatial period (pitch) of the grating. Accordingly, each wavelength is imaged at a different position x_λ on the DMD by the second lens. The system was aligned such that λ_c is imaged on the middle of the DMD (called pixel "0" and with $\lambda_c = 1980\text{nm}$), yielding:

$$x_\lambda = f_2 \tan(\theta_\lambda - \theta_{\lambda_c}) \approx f_2(\theta_\lambda - \theta_{\lambda_c}) \tag{5.3}$$

With x_λ the position along the x axis of a wavelength λ on the DMD, with θ_λ (resp. θ_{λ_c}) the diffracted of the wavelength λ (resp. λ_c) after the diffraction grating.

Applying the diffraction grating equation (**5.2**) leads to:

$$x_\lambda \approx f_2\left(\sin^{-1}\left(\frac{m\lambda}{\delta} - \sin\theta_{in}\right) - \theta_{\lambda_c}\right) \tag{5.4}$$

The tuning range Δλ for this system is:

$$\Delta\lambda = \lambda_{max} - \lambda_{min} \tag{5.5}$$

With

$$\begin{cases} x_{\lambda_{max}} = \dfrac{D - d_i}{2} \\ x_{\lambda_{min}} = -\dfrac{D - d_i}{2} \end{cases} \tag{5.6}$$

These positions correspond to the beam reaching the left and right extremities of the DMD whilst not clipping on the edges.

$$\begin{cases} x_{\lambda_{max}} = f_2\left(\sin^{-1}\left(\dfrac{m\lambda_{max}}{\delta} - \sin\theta_{in}\right) - \theta_{\lambda_c}\right) \\ x_{\lambda_{min}} = f_2\left(\sin^{-1}\left(\dfrac{m\lambda_{min}}{\delta} - \sin\theta_{in}\right) - \theta_{\lambda_c}\right) \end{cases} \tag{5.7}$$

With

$$\theta_{\lambda_c} = \sin^{-1}\left(\frac{m\lambda_c}{\delta} - \sin\theta_{in}\right) \tag{5.8}$$

Combining the previous equations:

$$\Delta\lambda = \frac{2\delta}{m}\left[\cos\left(\sin^{-1}\left(\frac{m\lambda_c}{\delta} - \sin\theta_{in}\right)\right) \sin\left(\frac{D - d_i}{2f_2}\right)\right] \tag{5.9}$$

Assuming that the DMD diagonal size is much smaller than the focal length of the second lens used to focus the beam onto the DMD we have

$$\frac{D - d_i}{2} \ll f_2 \tag{5.10}$$

$$\Delta\lambda \approx \frac{2\delta}{m}\left[\sqrt{1-\left(\sin^{-1}\left(\frac{m\lambda_c}{\delta}-\sin\theta_{in}\right)\right)^2}\,\frac{D-d_i}{2f_2}\right] \tag{5.11}$$

Which for this implementation with $m = 1$, $\theta_{in} = 45.4°$ and $\frac{1}{\delta} = 600\text{lines/mm}$, yields a tuning range $\Delta\lambda$ of 141nm.

The minimum increment in λ_{res} corresponds to the wavelength shift obtained by moving the DMD reflective area by one pixel along the x axis. This can be defined as:

$$\lambda_{res} \approx \Delta\lambda\frac{d_m}{2(D-d_i)} \tag{5.12}$$
$$\lambda_{res} \approx 0.094\text{nm}$$

Subsequently, the minimum bandwidth Δs is dependent on the reflective column width *k*:

$$\Delta s(k) = \begin{cases} \lambda_{res} & \text{if } k \leq d_i \\ \lambda_{res}\left(1+\frac{k-d_i}{d_m/2}\right) & \text{if } k > d_i \end{cases} \tag{5.13}$$

By increasing the DMD size or decreasing the second lens focal length used in the feedback arm, a wider tuning range can be achieved at the detriment of wavelength accuracy and bandwidth.

5.3 Experimental results

The system described allows tuning of the output spectrum by simple adjustment of the DMD reflective pattern. A reflective pattern consisting in a reflective column along the y axis would give a single-wavelength output spectrum. By changing the reflective area position along the x axis, wavelength tuning is achieved as the fed back wavelength is modified. The DMD allows the creation of more than one reflective area at the same time, offering capability for multi-wavelength behaviour. Moreover, by adjusting each reflective area size in y, modification of their respective reflectivity is achieved, leading to control over the spectral power density.

Alignment of the DMD in the current setup was performed to maximise output power at λ_c.

5.3.1 Wavelength control

As a spatial wavelength chirp is created by the diffraction grating, changing the position of a reflective area of the DMD adjusts the wavelength being fed back into the fibre, thus leading to tuning of the lasing wavelength. Figure 5.5 shows different output spectra obtained by moving a column of 25 "on-state" pixels across the DMD. Linear tuning from 1913.3 nm to 2044.4 nm is demonstrated, giving a $\Delta\lambda_{exp}$=131 nm, matching well with the theoretical tuning range calculated from eq. (**5.11**). The shortest and longest wavelengths obtained during this experiment were achieved just before clipping of the input beam onto the DMD edges.

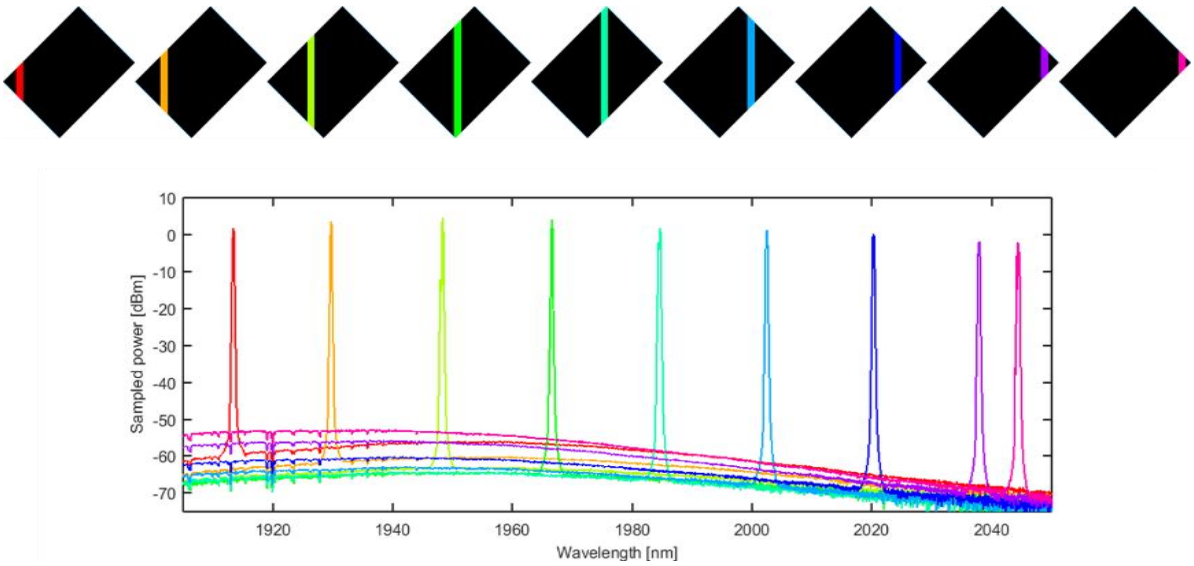

Figure 5.5 Example of spectra obtained utilising different reflective bands of 25 pixels width across the DMD.

The further the lasing wavelength from λ_c (which is the wavelength yielding the maximum output power) is, the stronger the ASE spectral component; calculations showed more than 98% of the output power was contained in the lasing wavelength across the entire tuning range. By moving away from the central wavelength λ_c, alignment of the feedback arm decreases, leading to lower output power and higher threshold, and hence the ASE part of the output spectrum increases. This evolution of feedback efficiency with wavelength is discussed in more detail later on (see Part 5.3.2) and its influence on laser performance is described.

The measured peak wavelength as a function of the reflective band position on the DMD is compared with theory in Figure 5.6. The theoretical values are obtained from equation (**5.4**) and match well with the experimental ones with a slight discrepancy which can be explained by the effect of spherical aberration created by the plano-convex lens used to focus the beam on the DMD.

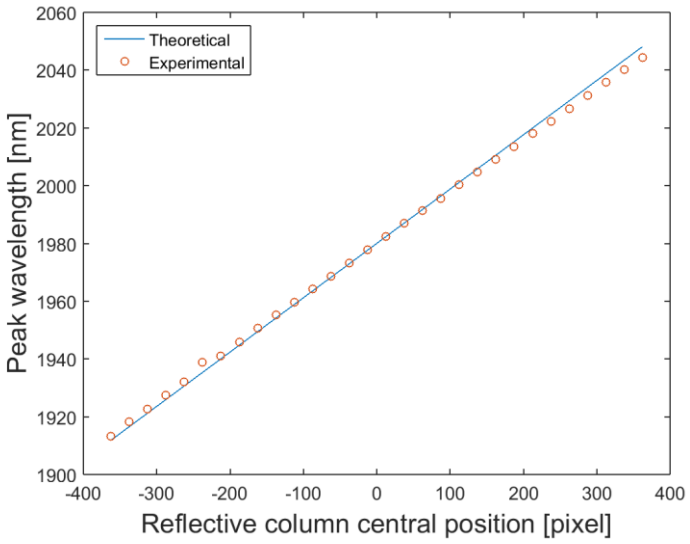

Figure 5.6 Lasing wavelength as a function of pixel band position

5.3.2 Wavelength dependence of laser performance

The slope efficiency obtained for this cavity design was up to 35% at 1980 nm. This fibre core composition has shown up to 39% slope efficiency in simple cavity arrangements with 793 nm pumping. In the current setup the slope efficiency is wavelength-dependent, decreasing down to 24% for an output at 2044 nm. Figure 5.7 shows the output power for 29W of injected power and lasing threshold as a function of wavelength. The reflective area on the DMD was a column of 25 "on-state" pixels that was moved by 25 pixels each time. The laser had its lowest threshold of 1.95W of absorbed pump power for a lasing wavelength at 1980 nm. increasing to 3.1W at 1913 nm which was the shortest wavelength achievable with this setup (see Figure 5.5). Maximum output is achieved at 1980nm with more than 8.5W, decreasing down to 5.5W at 2043nm.

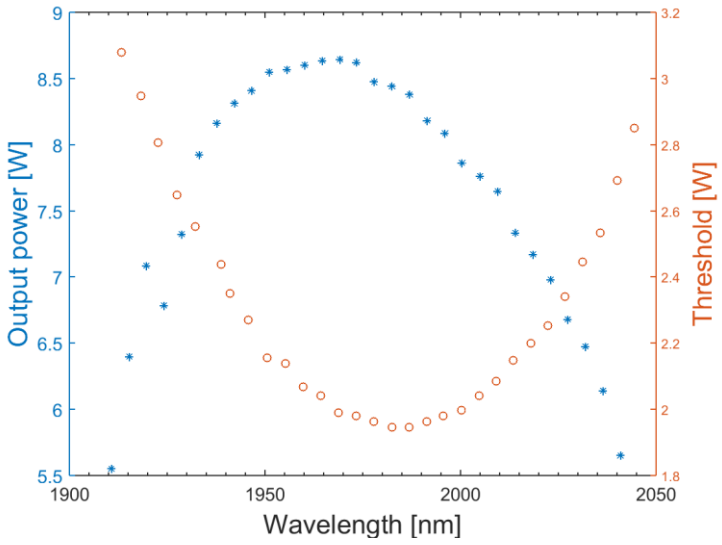

Figure 5.7 Output power and threshold as a function of lasing wavelength

The maximum output power and lowest threshold are obtained at the optimised alignment wavelength λ_c. This is partly explained by different mechanisms inherent to Tm-doped fibre lasers. An increase of the absorption cross section occurs for shorter wavelengths leading to higher reabsorption losses whilst a decrease of the emission cross section towards longer wavelengths occurs [5.16]. The quantum efficiency also decreases with longer wavelengths.

However, the main cause of the increase in threshold and reduction in output power as the wavelength is tuned from the optimum value is the wavelength-dependent misalignment induced by the DMD in this configuration. The micro-mirrors possess two stable positions shown earlier in Figure 5.4. As these positions are at + and -12°, the DMD is tilted by a ±12° angle to compensate and to allow feedback of the light into the fibre by the pixels in an "on-state". As a consequence, the reflective surface of the DMD is actually at an angle to the focal plane of the second lens as shown in Figure 5.8. This second lens also possesses a chromatic aberration and therefore creates a wavelength-dependent focal plane position. These two effects create an inherent wavelength dependence of the DMD feedback efficiency which is partly responsible for the threshold and output power evolution when moving away for the central wavelength λ_c. In silica, the refractive index decreases with

increasing wavelength leading to a longer focal length. The DMD was therefore tilted at +12°clockwise so that the DMD area corresponding to long wavelengths is placed after the focal plane in order to take advantage of the focal length variation with wavelength and thus mitigate feedback efficiency decrease with wavelength change. Decrease in feedback efficiency on the edges of the tuning range stills occurs and will create an increase in power of the ASE part in the output spectrum as shown previously in Figure 5.5.

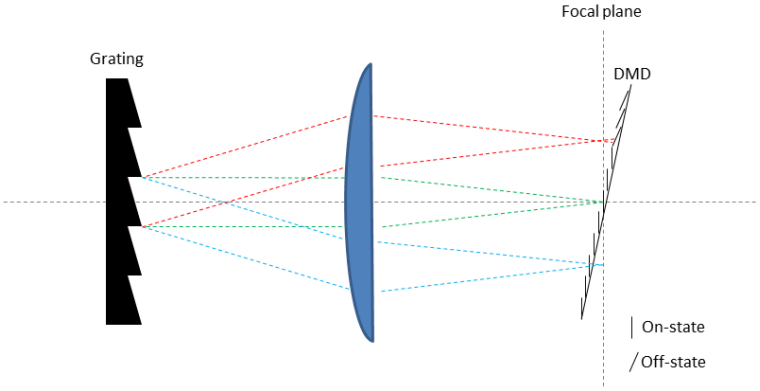

Figure 5.8 Beam focus position on the DMD as a function of wavelength.

The maximum output power achieved was more than 8.5W and was pump-power limited. The DMD was also reaching its damage threshold for the corresponding amount of incident power as some parts were showing damage in the form of pixels locked in their "on-state". Damage was mostly observed on the extremities of the tuning range as poor feedback efficiency lead to self-pulsing that degraded the pixels. After inspection of the faulty areas, it is suspected that the damage occurred as burnt or impaired electronics and actuators behind the micro-mirrors whilst the mirrors themselves remained intact.

5.3.3 Beam quality

An M^2 measurement was performed using a Nanoscan beam profiler from Photon inc. for a lasing wavelength at 1980 nm and an output power of 5W. The results are shown in Figure 5.9; an M_x^2 of 1.1 and a M_y^2 of 1 were deduced. Figure 5.9 shows near and far-field beam profiles with the near-field profile obtained with the Nanoscan beam profiler and the far-field one with a Spiricon Pyrocam 3. The M_x^2 and M_y^2 were also calculated for two other operating wavelengths: 1930 nm and 2030 nm. The values for M_x^2 observed were found to be 1.2 and 1.14 respectively, whilst the M_y^2 values were was 1.12 and 1 respectively. This fibre possesses a V-number of 2.64 at 1930 nm and 2.51 at 2030 nm thus allowing the LP_{11} to propagate in it with a cut-off wavelength of 2.1µm. The active fibre was coiled with a beam radius of 75 mm, creating a calculated bend loss for this mode of 132 dB/m (and 316 dB/m at 1930 nm and 2030 nm respectively. Therefore, the output beam was robustly single mode across the entire wavelength range.

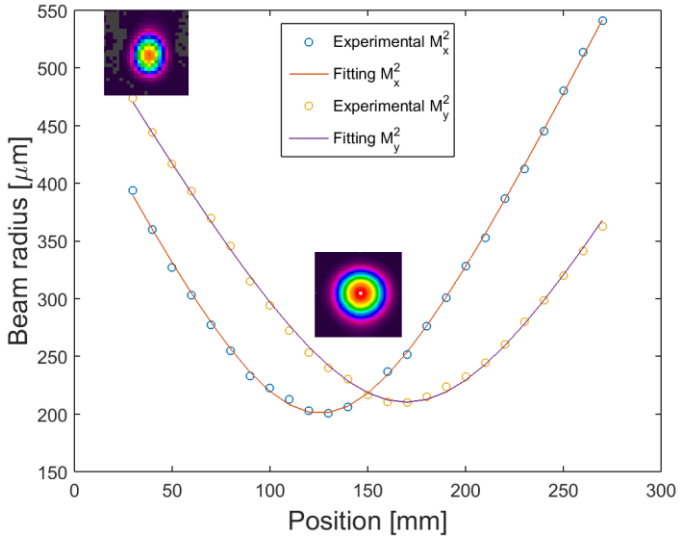

Figure 5.9 M^2 measurement of 1 and 1.1 from a Nanoscan beam profiler at 1980nm and 8.5W of output power

5.3.4 Bandwidth control

As the wavelengths are linearly chirped across the DMD, the bandwidth of the output spectrum can be adjusted by modifying the width of the reflective area of the DMD. The theoretical bandwidth was described in eq.(**5.13**) as a function of the "on-state" area width of the DMD. A flat section is expected for a column width of less than the beam size on the DMD d_i whilst a linear increase of the bandwidth with a slope corresponding to the system minimal wavelength accuracy λ_{res} should be seen for $k > d_i$. Bandwidth increase only occurs for narrow reflective areas on the DMD as laser operation leads to spectral narrowing, limiting the output spectrum maximal linewidth, whatever the reflective area width along the x axis.

To compare theoretical and experimental values, actual beam size on the DMD is needed. The beam size was measured in the y dimension by switching horizontal lines on the DMD to their "on-state" and measuring the evolution of output power. Increase in power by the addition of a specific horizontal line into its "on-state" mode indicates that part of the beam is reaching this position and is fed back into the active fibre. A beam diameter d_i of 460 µm was measured. This value fits with the theoretical beam size of 350µm calculated previously from equation (**5.1**). The theoretical slope of the bandwidth evolution for $k > d_i$ is calculated from eq.(**5.11**) by using the experimental values obtained for the tuning range and beam size and gives:

$$\lambda_{res} \approx 0.88\text{nm/pixel}$$

Figure 5.10 shows the evolution of the bandwidth of the output spectrum as a function of the width of the reflective column in pixels. A minimum can be observed for any column width smaller than 25 pixels (i.e. 480µm) which fits with what could be expected from the measured beam size of 460µm and equation (**5.13**). A linear trend then appears for wider reflective zones.

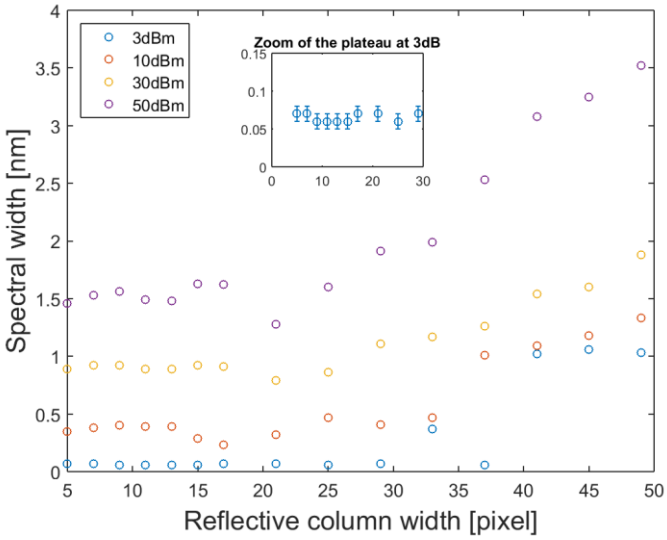

Figure 5.10 Laser bandwidth evolution as a function of the DMD reflective area width

5.3.5 Multi-wavelength behaviour

Multi-wavelength behaviour can easily be obtained in solid-state lasers by using an AOTF [5.13] or by multiple wavelengths being fed back into the gain medium by diverse mechanisms such as two gratings in a row of two feedback arms [5.17-21]. Such demonstrated configurations would create a dual-wavelength output spectrum. More simultaneous output wavelengths can be achieved by dividing the feedback arm into more than two separate arms, each arm feeding back a different wavelength. Multiple wavelengths reflected into the gain medium would not inevitably lead to a multi-wavelength spectrum as gain competition will occur and a slight difference in feedback efficiency between the wavelengths can cause gain saturation by one wavelength, forbidding the others to lase. Therefore, careful control of the targeted wavelengths respective reflectivity is needed to avoid one from dominating. Moreover, adjustment of the reflectivities causes a change of the quality factor for each wavelength which then modifies the power distribution between the lasing wavelengths [5.17].

Here we can apply the same principle by increasing the number of independent reflective areas from one to many on the DMD. It was shown previously that the lasing wavelength can be changed by altering the position of a reflective column on the DMD, thus each reflective area would feed back a different wavelength, generating a multi-wavelength output spectrum. In Figure 5.11, a reflective pattern made of three reflective columns was utilised, giving a tri-wavelength output spectrum. Lasing at these three different wavelengths was possible due to their proximity; each wavelength had almost the same reflectivity and gain (from emission/absorption cross-sections), making it easier to avoid gain competition and forcing all of them to lase.

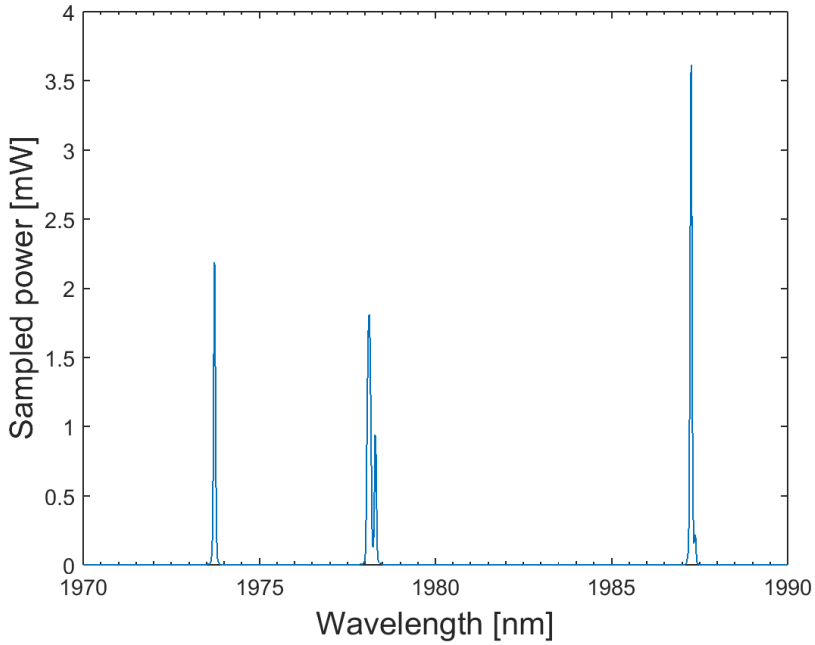

Figure 5.11 Spectrum showing three-wavelength output

The position along the x axis and width of an "on-state" column of pixels determine a lasing wavelength and its bandwidth. In the same way, its width along the y axis determines the feedback efficiency at this particular wavelength. Thus, by adjusting the vertical width of each reflective column, the power distribution between the selected wavelengths can be controlled. Such a feat was performed with a dual-wavelength output spectrum generated from two independent reflective areas on the DMD, demonstrating crude control over the Spectral Power Density (SPD). Figure 5.12 shows these two spectra with two output wavelengths at 1920nm and 2020nm. In the first case, each wavelength contains the same amount of power whilst in the second case; the 2020nm wavelength contains most of the power, with a power distribution ratio of 10 to 1.

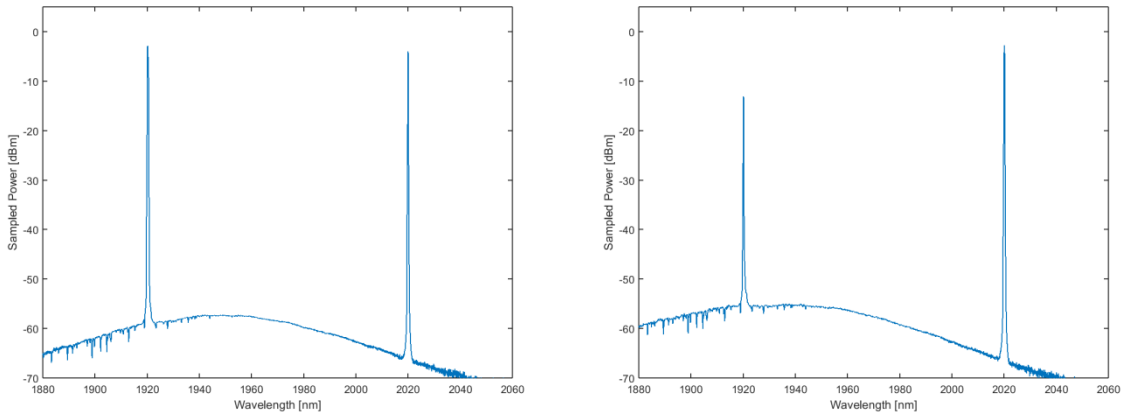

Figure 5.12 Spectrum showing two bi-wavelength outputs with different SPD

This solution offers the advantage of using a single feedback arm instead of as many arms as the numbers of desired simultaneous wavelengths. Moreover, a single readily available component (DMD) is used to shape the

spectrum instead of needing specific components such as suitable dichroic mirrors. Only crude control over the SPD is demonstrated due to the small number of pixels available to adjust feedback; each wavelength has a corresponding spot on the DMD with a vertical size of less than 20 pixels.

Fine control can be achieved by increasing the number pixels covered by the beam, either by expanding the beam or by upgrading to a newer DMD chip, offering higher resolution and smaller pixels (e.g. Texas Instruments DLP9000 with a resolution of 2560x1600 and a micro-mirror pitch of 7.6 µm). The implementation of cylindrical lenses would allow vertical expansion to achieve better spectral power density control whilst keeping small horizontal dimension of the beam needed for broad tuning range.

5.4 Discussion

This system offers fast reliable tuning of the output spectrum. The tuning speed is determined by the actuators and the control electronics; the actuators have a refreshing speed reaching up to 75 µs [5.15]. This is comparable to the tuning speed of an AOTF tuned laser whose switching time is of the order of tens of µs. However, a typical commercial AOTF working at 2µm has a minimal bandwidth of at least 1.5 nm at FWHM (e.g. Gooch & Housego TF2000-1000-2-6-GH78) and up to 10's of nm for some devices, them whilst the present configuration utilising a DMD can reach a FWHM of 0.08nm.

AOTFs are polarization-sensitive devices leading to low feedback efficiency for non-PM fibre based systems and can achieve, when coupled with a high reflectivity mirror, up to 25% feedback efficiency due to a double-pass into the AOTF in linear laser cavities. The configuration described here uses a diffraction grating that is also polarization-sensitive to a certain extent, but only generating losses of few percent, allowing a potential feedback efficiency of up to 70%. This difference would lead to much better slope efficiencies for DMD based configurations compared to AOTF-based feedback arrangements with non-PM fibres even though AOTF systems would be preferred for configurations containing PM-fibres. However, slope efficiencies reported in the literature with Tm-doped PM-fibres are lower than for non-PM ones with around 55% [5.22] and therefore their use is avoided for many of the targeted applications. An AOTF also requires a constant RF signal to be sent to it, thus a constantly running RF generator with a dedicated power supply consuming energy whilst a DMD configuration offers the advantage of necessitating a standard 0/5V power supply and consuming energy only when switching the mirrors i.e. when modifying the spectrum. DMD control boards also offer the ability to alternate between different reflective patterns at a speed up to 32kHz (e.g. Texas Instruments DLP7000) directly from a computer or a dedicated system.

5.5 Conclusion

We demonstrated wavelength-tuning from a linear cavity design Tm-doped fibre laser with a DMD combined with a diffraction grating as a tuning element. More than 8.5W of output power with a slope efficiency of 35% was obtained at the central wavelength of 1980 nm (pump-limited) and tuning from 1913 nm to 2044 nm was

performed, limited by the DMD horizontal size D for the set of imaging lenses chosen here. The wavelength-control of this system by displacement of the reflective area position on the DMD was described and compared to theoretical expectations; the tuning range achieved of 131nm fitted with the theoretical value of 141nm. Bandwidth-control of the output spectrum was performed by adjustment of the reflective area width on the DMD. Results were analysed and matched with theoretical simulations, showing a minimal bandwidth at 3dB of 0.1nm for any reflective area narrower than 25 pixels (image size of the fibre tip onto the DMD) whilst calculations from the experimental tuning range were giving a minimal linewidth of 0.088nm. Slope efficiency and threshold behaviour according to output wavelength were shown with increase in threshold from 1.85W to 3.1W when moving away from the central wavelength. Accordingly, a decrease of slope efficiency from 35% to 24% occurred.

A three-wavelength output spectrum was reported with an explanation to replicate the process for multi-wavelength spectra through adjustment of the DMD reflectivity pattern. A way to modify the power distribution in a multi-wavelength configuration was explored through adjustment of the DMD reflectivity pattern corresponding to each wavelength, leading to versatile wavelength-dependent feedback efficiency. A demonstration of this process was given with a dual-wavelength output spectrum where the power ratios between both wavelengths were changed from 1-to-1 to a ratio of 10-to-1 and a route to full control of the SPD was detailed.

5.6 References

5.1. Li, Z., et al., *Thulium-doped fiber amplifier for optical communications at 2μm.* Optics Express, 2013. **21**(8): pp. 9289-9297.

5.2. Sonnenfroh, D.M. and M.G. Allen, *Absorption measurements of the second overtone band of NO in ambient and combustion gases with a 1.8μm room-temperature diode laser.* Applied Optics, 1997. **36**(30): pp. 7970-7977.

5.3. Cariou, J.P., B. Augere, and M. Valla, *Laser source requirements for coherent lidars based on fiber technology.* Comptes Rendus Physique, 2006. **7**(2): pp. 213-223.

5.4. De Young, R.J. and N.P. Barnes, *Profiling atmospheric water vapor using a fiber laser lidar system.* Applied Optics, 2010. **49**(4): pp. 562-567.

5.5. Kadwani, P., et al., *Atmospheric absorption spectroscopy using Tm: fiber sources around 2 microns.* Atmospheric and Oceanic Propagation of Electromagnetic Waves V, 2011. **7924**.

5.6. Jelinkova, H., et al., *Diode-pumped Tm : YAP laser for eye microsurgery - art. no. 68712N.* Solid State Lasers Xvii: Technology and Devices, 2008. **6871**: p. N8712.

5.7. Alexander, V.V., et al., *Photothermolysis of Sebaceous Glands in Human Skin Ex Vivo with a 1,708 nm Raman Fiber Laser and Contact Cooling.* Lasers in Surgery and Medicine, 2011. **43**(6): pp. 470-480.

5.8. Scott, N.J., C.M. Cilip, and N.M. Fried, *Thulium Fiber Laser Ablation of Urinary Stones Through Small-Core Optical Fibers.* Ieee Journal of Selected Topics in Quantum Electronics, 2009. **15**(2): pp. 435-440.

5.9. Mingareev, I., et al., *Welding of polymers using a 2µm thulium fiber laser.* Optics and Laser Technology, 2012. **44**(7): pp. 2095-2099.

5.10. J. Flaud, A.B., and N. Husson, *REFERENCES and SOURCES for HITRAN.* 2013(0, 4058–4097).

5.11. Shen, D.Y., J.K. Sahu, and W.A. Clarkson, *High-power widely tunable Tm: fibre lasers pumped by an Er, Yb co-doped fibre laser at 1.6µm.* Optics Express, 2006. **14**(13): pp. 6084-6090.

5.12. Takabayashi, K., et al., *Widely (132 nm) wavelength tunable laser using a semiconductor optical amplifier and an acousto-optic tunable filter.* Electronics Letters, 2004. **40**(19): pp. 1187-1188.

5.13. Yumoto, M., et al., *Electronic Wavelength Tuning of Tunable Laser with Acousto-Optic Tunable Filter.* Japanese Journal of Applied Physics, 2008. **47**(11): pp. 8411-8415.

5.14. Yun, S.H., I.K. Hwang, and B.Y. Kim, *All-fiber tunable filter and laser based on two-mode fiber.* Optics Letters, 1996. **21**(1): pp. 27-29.

5.15. Shin, W., et al., *Wavelength-tunable thulium-doped single mode fiber laser based on the digitally programmable micro-mirror array.* Optical Fiber Technology, 2013. **19**(4): pp. 304-308.

5.16. Agger, S.D. and J.H. Povlsen, *Emission and absorption cross section of thulium doped silica fibers.* Optics Express, 2006. **14**(1): pp. 50-57.

5.17. Alvarez-Tamayo, R.I., et al., *Investigation of cavity loss adjustment between two wavelengths required for dual-wavelength laser generation.* Fiber Lasers Ix: Technology, Systems, and Applications, 2012. **8237**.

5.18. Evans, J.M., et al., *Dual-Wavelength Self-Mode-Locked Ti Sapphire Laser.* Optics Letters, 1993. **18**(13): pp. 1074-1076.

5.19. Khare, R., et al., *A Tunable 3-Wavelength Copper-Vapor Laser-Pumped Dye-Laser with Collinear Output.* Optics Communications, 1995. **114**(3-4): pp. 275-279.

5.20. Liu, D.F. and C.H. Wang, *Single linearly polarized, widely and freely tunable two wavelengths Y-b(3+)-doped fiber laser.* Optics Communications, 2010. **283**(1): pp. 98-103.

5.21. Liu, X.M., et al., *Stable and uniform dual-wavelength erbium-doped fiber laser based on fiber Bragg gratings and photonic crystal fiber.* Optics Express, 2005. **13**(1): pp. 142-147.

5.22. Liu, J., et al., *210 W single-frequency, single-polarization, thulium-doped all-fiber MOPA.* Optics Express, 2014. **22**(11): pp. 13572-13578.

Chapter 6. Tunable two-micron fibre-based amplified spontaneous emission sources

6.1 Introduction

Amplified spontaneous emission (ASE) sources offer broad output bandwidths with low temporal coherence but can still possess high brightness and spatial coherence. These sources are of great interest for many applications such as the optical coherence tomography (OCT) and other low-coherence interferometry applications [6.1-3] where they have been widely adopted thanks to their high temporal stability and broad wavelength coverage. In this chapter we present different novel ASE source designs for broad and spectrum-controllable ASE generation, focusing on generation of pulsed ASE output in fibre sources via the use of an AOM. These sources are intended, following amplification with the aid of a fibre power amplifier, for pumping an optical parametric oscillator (OPO) in order to generate output in the mid-IR wavelength regime.

ASE sources also offer many benefits compared to lasers for high power operation due to their absence of longitudinal modes. One of the main limitations of fibre laser sources in the context of power scaling is non-linear effects such as SRS and SBS, which are detrimental to high power operation. This can be somewhat overcome by increasing the fibre core diameter, increasing the non-linear thresholds often at the detriment of their single-mode operation. By expanding the core area, the fibre's V-number increases up to a point where the fibre does not operate single-mode anymore and in a multi-mode fibre many modes can propagate with up to m modes allowed for a selected fibre, with $m \approx \frac{V^2}{2}$.

However, the guided modes interfere with each other, leading to an unstable spatial output profile [6.4-6] which manifest as beam pointing instability as well as variation of intensity profile and M^2. This interference pattern is a function of the phase difference between each mode which randomly and continuously changes due to fibre movement, internal temperature changes or stress, making active correction through computer-controlled elements such as galvo-mirrors extremely challenging. A straightforward way to average-out this temporal variation in interference patterns and accordingly beam pointing issues, is to reduce the temporal coherence length of the seed source used to a value shorter than the modal beat length of the modes available in the multi-mode fibre. The output profile is then an overlap of many interference patterns leading to a smooth symmetrical output beam with high pointing stability [6.7, 8]. ASE sources are therefore of great interest for multimode fibres systems thanks to the absence of longitudinal modes leading to short temporal coherence length whilst still achieving high spatial coherence, allowing good focussing of the beam. The absence of longitudinal modes coupled to the short temporal coherence length permits the use of multi-mode fibres in amplifier stages whilst avoiding beam pointing instabilities. Moreover, increase of the output linewidth by generating ASE instead of laser light in a fibre also decreases the risk of SBS by increasing its threshold as SBS thresholds depends on the signal bandwidth (see Section 2.6.2.1).

6.2 Background

ASE sources are generally constructed by suppressing feedback into the gain medium, leading to a round-trip gain lower than unity. This avoids longitudinal modes building up due to the absence of a cavity and the output is a broadband ASE. Commonly, a fibre gain medium with both ends modified in order to suppress feedback into the core [6.9] is a simple design for an ASE source, as shown in Figure 6.1. When pumped, temporally incoherent light is generated with a broad spectrum defined by the spontaneous emission spectrum of the gain medium. This classic scheme has the advantage of being easily constructed but leads to emission at both ends of the fibre and can still lead to parasitic lasing at high power due to slight unwanted reflections and needs careful preparation to avoid it [6.10]. Parasitic lasing leads to power stability issues as the cavity is based on small unwanted reflections which can vary and spectral narrowing due to gain competition. Adjustment of the reflectivity of both fibre ends by adjusting the cleave angle can also lead to single-output end behaviour [6.11, 12]. This scheme is however highly prone to parasitic lasing as any feedback from the output cleave, or from any element after it such as a collimating lens, leads to the formation of a cavity and thus of an oscillator with a laser output. In most unidirectional ASE sources, an isolator is added after the end facet to avoid unwanted feedback into the fibre. Single stage configurations can lead to 10s of Watt up to more than 100W of output power [6.9, 10, 12-15] and seed/amplifier configurations can then be used to amplify the ASE created and allow high output powers in the 1kW regime [6.16].

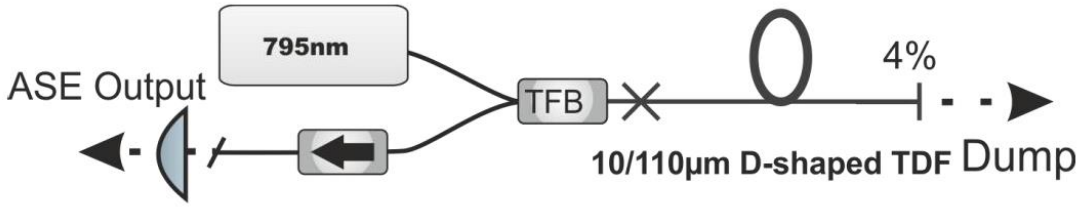

Figure 6.1 Schematic of a classical fibre-based ASE source by forbidding feedback [6.8]

All these systems, bi or unidirectional, are built on the principle of suppressing feedback. These techniques work well at low power but, when at high power, require efficient high power isolators to suppress parasitic lasing. This is especially challenging as undesired optical feedback is inevitable from any downstream equipment utilising these sources. Moreover, the optics and components used must have good anti-reflection coatings to avoid unwanted feedback into the fibre.

For some applications, wavelength coverage or shaping of specific spectral regions at the detriment of others is required [6.17, 18]. This can be achieved by a wavelength selective feedback approach inside the ASE source. A trade-off must be made between the need for feedback and the need to maintain feedback levels low enough to avoid parasitic lasing. Tailoring of the output spectrum is therefore often achieved post generation outside of the cavity by removing the undesired parts of the ASE spectrum [6.19]. This process is quite inefficient particularly when aiming for relatively narrow-band ASE as only a fraction of the generated power is utilised.

6.2.1 Feedback tolerant ASE sources utilising an AOM

In fibre systems, Acousto-Optic Modulators (AOMs) are often used for Q-switched mode of operation. In such configurations, the AOM alternates between its 'on' and 'off' states. In one state, light is going through without modification and feedback is provided into the cavity. When in the other state light is diffracted and dumped and accordingly no feedback is provided. In this way, switching of the cavity Q is realised and a pulsed output results. Figure 6.2 shows the effect of an AOM on the input beam, angularly separating the diffracted and transmitted beam. The light frequency intra-cavity (and accordingly its wavelength) increases or decreases depending on the diffracted order (±1) of the AOM aligned with the cavity and follows the equation

$$F_{n+1} = F_n \pm 2F_{RF} \tag{6.1}$$

$$\lambda_{n+1} = \frac{\lambda_n . c}{c \pm \lambda_n 2F_{RF}} \tag{6.2}$$

Where c is the speed of light in air, F_n (resp. λ_n) the frequency (resp. wavelength) after the n^{th} round-trip

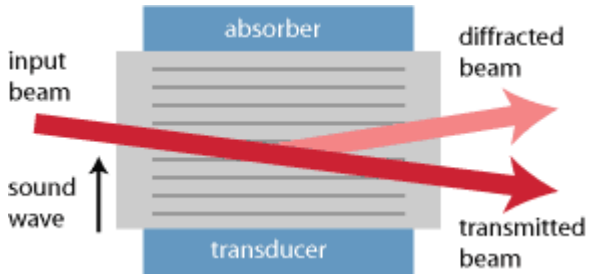

Figure 6.2 Effect of an AOM on an incoming beam [6.20]

For example an AO modulator driven at a frequency of around 100MHz with an incident wavelength of 2µm leads to a wavelength shift of less than 3pm on each cavity round trip, according to equation (**6.2**).

The AOM can also be used to create a Q-switched fibre source with dynamics fast enough to generate ASE light instead of laser behaviour by utilising it for feedback during its 'on' state. The AOM is configured to dumped the light when in its 'off' state, ensuring no feedback is provided into the cavity. The AOM is then switched into its 'on' state for a time too short to allow establishment of longitudinal modes but long enough to permit the generation of a pulse thanks to the high small signal gain provided by the active fibre. This pulse consists in the fed back ASE light which amplified over few round-trips before the pulse energy is extracted from the fibre.

However, after hundreds of round-trips, mode-locking occurs as result of the round trip frequency shift created by the AOM [6.21], thus the AOM state must be switched back after extraction of the first pulse to avoid lasing to occur. This technique is only possible in fibre-based sources due to their high small-signal gain which results in quick pulse build-up. This specific technique for ASE generation has the benefit of being based on cavity dynamics rather than feedback suppression. Thus this allows higher feedback level tolerances making it more robust and offers possibility of high spectral control whilst still achieving high output power efficiency compared to previous strategies.

Figure 6.3 shows a conceptual schematic of a pulsed ASE source based on an AOM and tolerating high feedback. An active fibre with one end perpendicularly cleaved acting as output coupler and the other is angle-cleaved at 8°. The fibre is pumped through a WDM. The cavity comprises a free-space feedback arm in which the light is collimated before going through the AOM. This cavity is aligned such that feedback is provided from a plane mirror when light is diffracted, and hence frequency shifted, by the AOM.

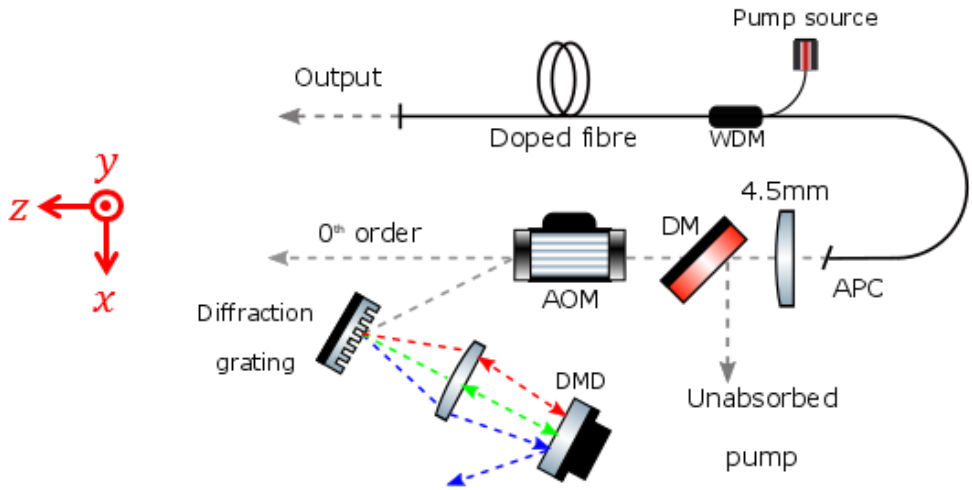

Figure 6.3 Free-space Q-switched fibre source for ASE generation based on an AOM

When the AOM is in its 'off'-state, no feedback is provided into the fibre and inversion builds-up into the gain medium. This high inversion leads to ASE inside the cavity which is then dumped through the AOM. Due to feedback suppression and the short time window, the cavity behaves like a classical feedback suppressed ASE system. Once the AOM is switched into its 'on'-state, feedback of the previously dumped ASE is provided into the cavity and is heavily amplified intra-cavity through multiple round-trips thanks to the high levels of inversion and a pulse is extracted.

6.2.2 First demonstration of AOM-based ASE source by Jae Daniel

This setup utilising an AOM for amplified spontaneous emission whilst tolerating high feedback efficiency was previously demonstrated by Jae Daniel at the Optoelectronics Research Centre (University of Southampton, UK) [6.8]. The output spectra observed did not show the characteristics of a laser such a spectral narrowing. However, longitudinal modes in fibre lasers are so close to each other that their observation is extremely difficult, therefore we can only deduce that this source behaves like an ASE source and will here be called ASE source. A wavelength-controllable ASE source was described based on a wavelength-selective feedback allowing bandwidth control. Figure 6.4 shows the setup used which consisted of a meter-long Tm-fibre with a core diameter of 10µm and a cladding diameter of 100µm with a doping concentration of 0.2wt% core-pumped at 1565nm. One end of the active fibre was perpendicularly cleaved acting as an output coupler whilst the other end was angle-cleaved to avoid feedback. This angle-cleave was followed by a collimating lens, an acousto-optic modulator and a diffraction grating followed by a high reflectivity plane mirror for wavelength-selectivity.

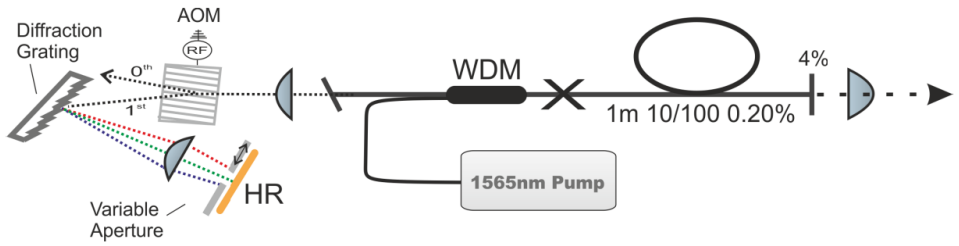

Figure 6.4 Experimental arrangement used by Jae Daniel for generation of wavelength-controlled pulsed ASE [6.8]

A second lens was placed between the grating and the plane mirror, imaging the fibre core onto the mirror and a slit was positioned in front of the reflector. This slit width allowed control of the ASE bandwidth and the position of the slit controls the central wavelength. Figure 6.5 shows control over the ASE bandwidth through reduction of the slit aperture.

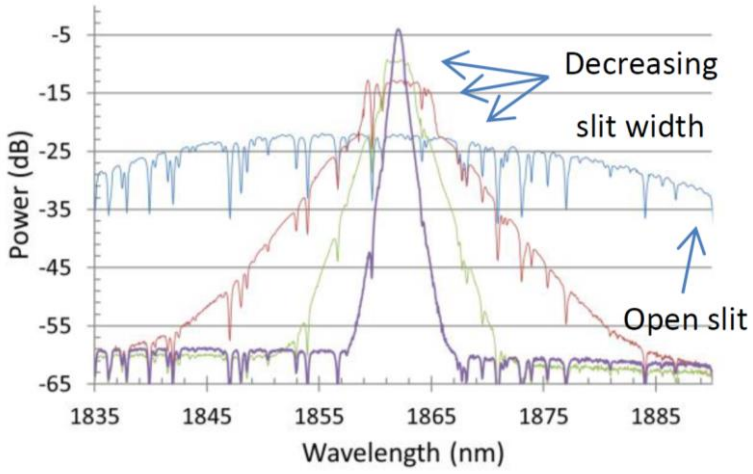

Figure 6.5 Control over ASE bandwidth by adjusting feedback through a slit/mirror combination [6.8]

6.3 Core-pumped ASE source

6.3.1 Experimental setup

Figure 6.6 shows an ASE source set-up based on a simple linear cavity containing a doped fibre gain medium: it consisted of a 0.2wt% Tm-doped silica host fibre with a 10/125µm core/cladding diameter core-pumped at 1550nm. Pump power was supplied from a 20W Er,Yb fibre laser delivered by a 10/125µm and injected into the Tm-fibre through a 1500/1900nm WDM. The active fibre was terminated by a perpendicular cleave at one end, which operates as the output coupler, and by an angle-polished 8° cleave at the other end with a free-space feedback arm. The feedback arm comprised a 4.5mm uncoated collimating lens, an AOM to avoid laser behaviour and promote pulsed ASE output and a wavelength-selective feedback system. The AOM used here is a Gooch & Housego M111-2J-AV1 AOM, anti-reflection coated from 1520 to 1630 with a rise time in the order of 100ns, depending on the collimated beam diameter which still offered low reflection and high diffraction

efficiency at 2µm. It has a driving frequency of 111MHz (F_{RF}) and is alternating 'on' and 'off' states at a frequency of 150kHz with a duty cycle of 20%. The duty cycle was reduced to maximise pulse energy and avoid mode-locking to occur, switching the AOM back in its 'off' configuration just after extraction of the first pulse. By reducing the AOM 'on' time, this forbids mode-locking to occur as such a phenomenon in this configuration occurs when the cavity experiences many round-trips. Here the cavity is switched back to a low feedback configuration following the ASE pulse extraction. The DMD was aligned to maximise reflectivity, ensuring high slope efficiency and the grating was angularly aligned to maximise output power for the central area of the DMD. This ensures that the tuning range available through the DMD control is centered on the emission spectrum providing maximum gain. The AOM aligned to diffract to the first order thus modifying the path of the beam and creating a frequency shift of the optical wave by 111MHz.

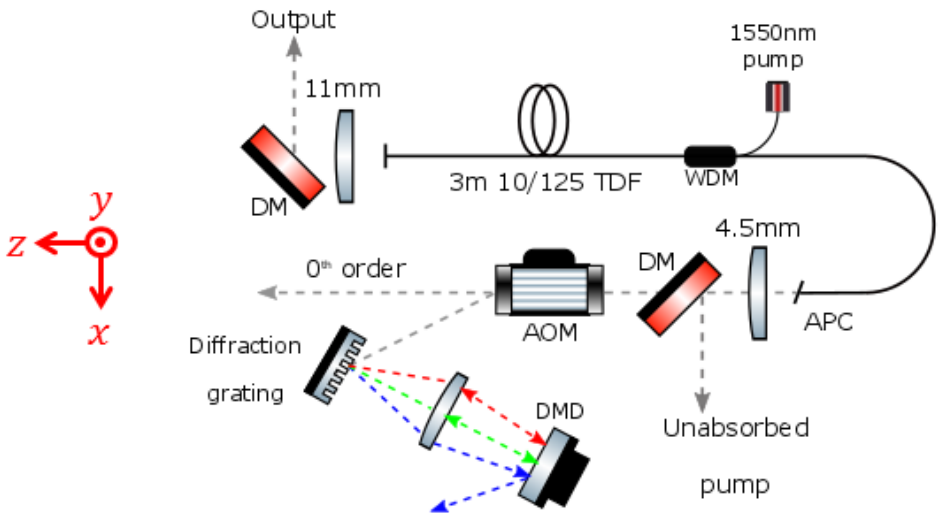

Figure 6.6 Core-pumped tailored ASE setup for emission centred at 1880nm

This wavelength-selection system is based on the tunable laser controlled by a DMD demonstrated previously in Chapter 5 and comprises a diffraction grating along the y axis (600lines/mm) blazed at 35° spatially chirping the beam in wavelength followed by a second lens to image the fibre core onto a DMD. The focusing lens is anti-reflection coated at 2µm and has a focal length of 150mm. The DMD used here is a DLP4100 from Texas Instruments composed of 1024 by 768 mirrors with a pitch of 13.68µm The DMD can then be configured to reflect different wavelengths according on the zone active on the DMD. Such a system has the same mechanics and variables as the tunable laser utilising a DMD previously demonstrated (Chapter 5). By having multiple reflective areas on the DMD, multiple wavebands are fed back into the cavity. Selecting the position and width of each waveband allows control of their respective central wavelength and bandwidth. Adjustment of the spectral power density of the output spectrum is realised intra-cavity by modifying the reflectivity of each 'on' area of the DMD and is described later on in Section 6.3.2.2. Easier power control of the different spectral sections of the output spectrum is achieved as less spectral narrowing occurs in an ASE source compared to a laser.

6.3.2 Results

6.3.2.1 Broad ASE spectrum generation and wavelength tuning

By using a fully reflective pattern on the DMD, feedback over the entire emission spectrum was provided, leading to generation of a pulsed broad ASE spectrum. Figure 6.7 shows the output spectrum obtained from the ASE source core-pumped at 1550nm from Figure 6.6 with emission centred at 1885nm. A non-continuous spectrum is achieved with many dips; these sharp pits are mostly water vapour absorption features present in the free-space feedback arm whilst some are due to other gas lines such as CO_2. This source can therefore be used to probe the gas contained in the feedback arm, deducing from the output spectrum the gas contents and their concentration. The spectrum showed here was obtained for at a repetition rate of 150kHz and average power was of 350mW. As explained previously in Chapter 2, a core-pumped system utilising a low-dopant concentration fibre should achieve short wavelength emission between 1800 and 1950nm. Here the spectrum displayed in Figure 6.7 is centred in the expected wavelength range with a FWTM of 25nm, reducing when scaling output power as for any ASE source.

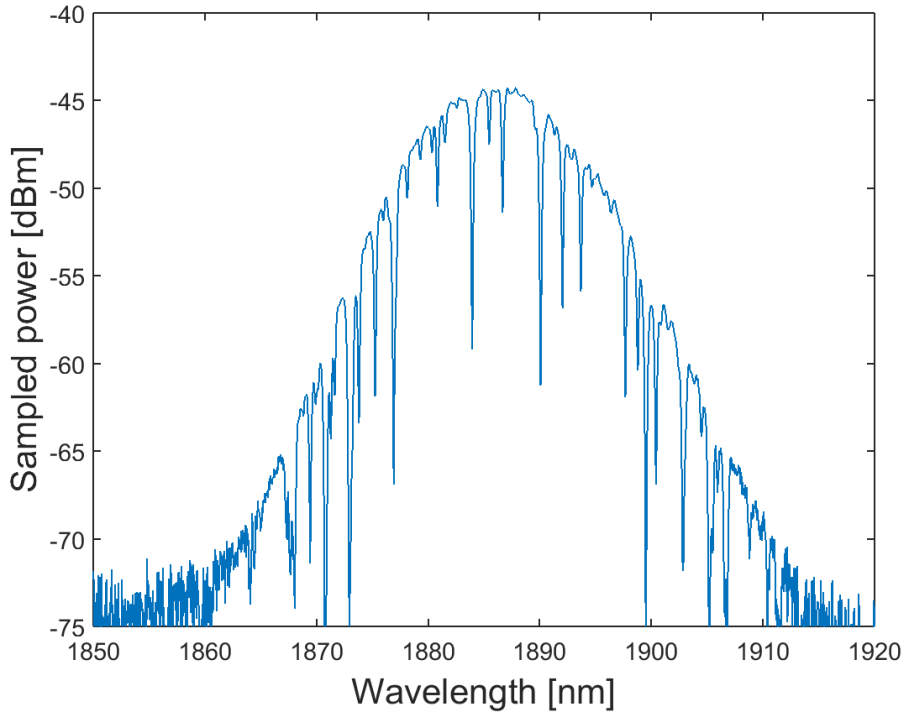

Figure 6.7 ASE generated around 1890nm with water vapour absorption features

A smoother spectrum can be achieved by suppressing these absorptions lines via the use of a sealed dry nitrogen box containing the feedback arm, removing the unwanted gases responsible for these dips because of their absorption lines. Figure 6.8 shows the output spectrum obtained from the same ASE source rebuilt in a dry nitrogen box. This spectrum differs from the previous one showed in Figure 6.7 as the system was not optimised but this experiment demonstrates that purging the feedback from most of its water vapour by injecting dry nitrogen removes the dips. Slight features are still observed as the purging is not perfect and some water vapour still subsists in the feedback arm but these dips are on the much lower scale than previously observed.

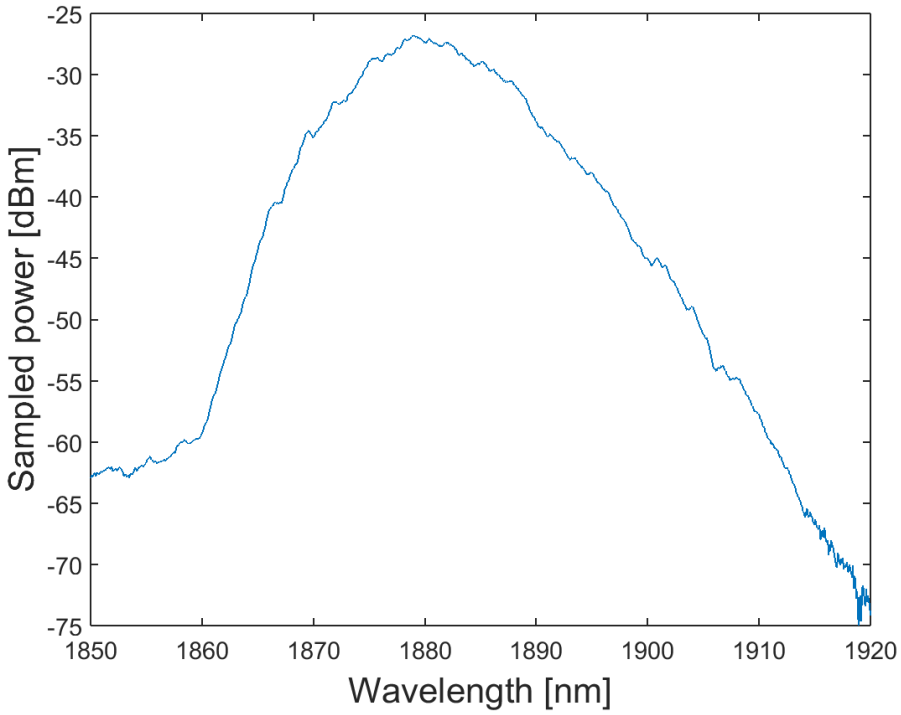

Figure 6.8 ASE generated around 1890nm purged with dry nitrogen to remove water vapour absorption features

Figure 6.9 shows narrowing of the output spectrum whilst conserving an ASE output where no fine structures associated to laser longitudinal modes is observed. Linewidth could be controlled with a FWHM down to 0.15nm and a FWTM of 0.3nm. No drop of power was observed when reducing the spectral width. However, when further reducing the reflective area width from 13 to 9 pixels along the x axis, a drop of power from 358mW to 311mW occurred but without modification of the linewidth.. This minimal linewidth can be compared to the minimal linewidth offered by the system and described previously in Chapter 5, following equation X that gave a minimal linewidth of 0.1nm in laser behaviour. The value obtained here of 0.15nm is quite close to the theoretical one.

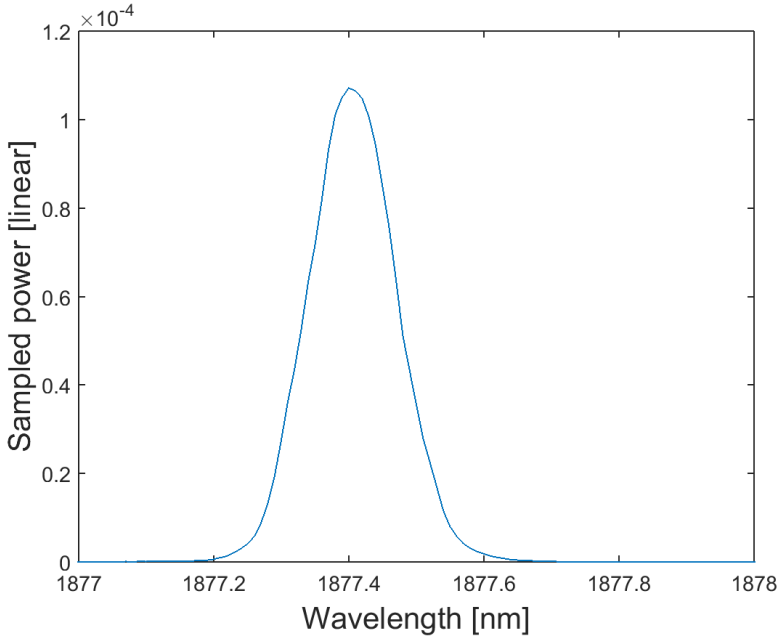

Figure 6.9 Spectral narrowing of the ASE source down to 0.15nm FWHM

Figure 6.10 shows wavelength-tuning by modifying the reflective pattern on the DMD. A reflective band with a width of 50pixels is translated over the DMD, feeding back different spectral bands and tuning from 1835 to 1935nm is achieved. Output power is decreasing towards the long wavelength range with overall power moving from 350 to 250mW and the CW ASE background increases significantly.

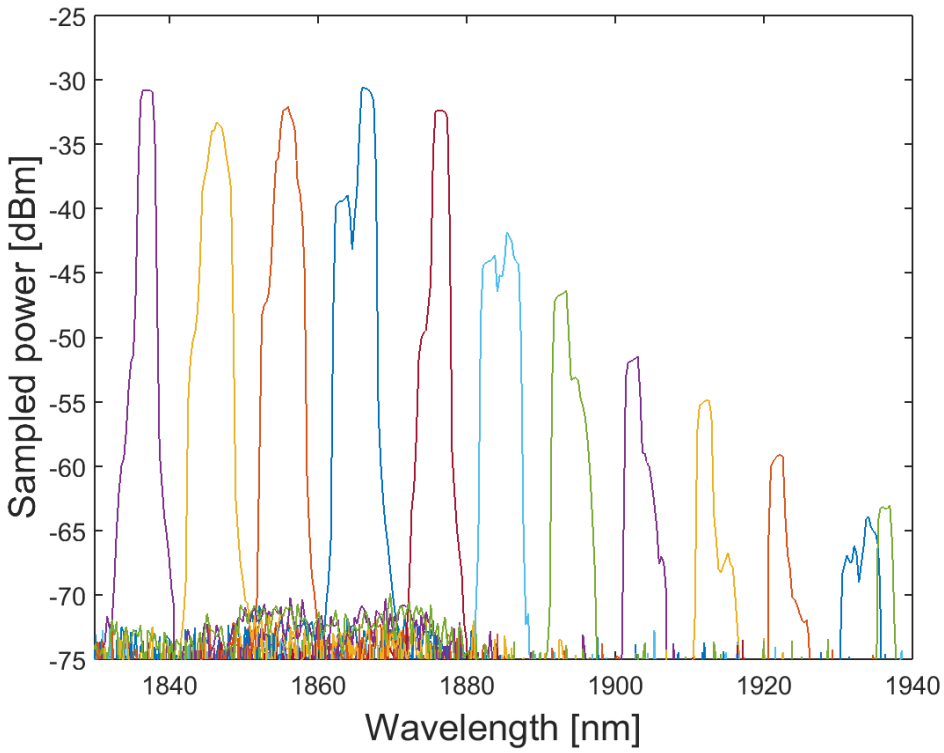

Figure 6.10 Example of ASE spectra obtained in a core-pumping architecture utilising different reflective band of 50 pixels width across the DMD

6.3.2.2 Spectral shaping

This configuration offers the possibility of multi-wavelength behaviour as well as control of the spectral power density (SPD) by modifying the 2-dimensional reflectivity pattern on the DMD. Such intra-cavity shaping is interesting for applications requiring particular spectra and for good wall-plug efficiency. By avoiding extra-cavity spectral filtering, the most of generated power is used instead of dumping unnecessary parts of the generated spectrum as it is often the case in conventional ASE systems. Here, due to the ASE behaviour of this source compared to a laser, gain saturation and gain competition are present at a lower level, allowing better control of the spectral power density. In a laser configuration, slight modification of the reflectivity ratio for two different wavelengths could lead to significant changes of the output power ratio of these wavelengths, but in an ASE configuration, power ratio evolution should be less sensitive and more controllable, allowing easier adjustment of the output spectral shape.

Therefore, through picture shaping on the DMD pattern, it is theoretically possible to shape the output spectrum or achieve flatness. Here, picture shaping principle is demonstrated through three different pictures (shown in Figure 6.11) corresponding to three different reflectivity patterns where white pixels correspond to “on-state”

and black ones to “off-state” sent to the DMD in order to increase spectrum flatness for a DMD reflective area corresponding to a window of 8 nm centred at 1947nm.

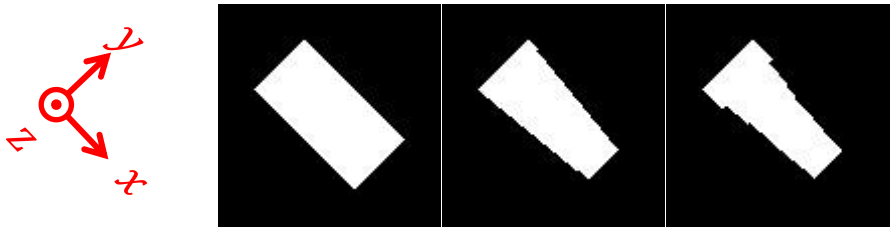

Figure 6.11 Picture shaping modification for flattening of the output spectrum

Figure 6.12 shows spectrum evolution for the three different pictures with flatness of the output spectrum as a target. The blue curve corresponds to the first reflective pattern in Figure 6.11 whilst the green curve corresponds to the second pattern and the red curve to the last pattern. Flatness improvement over the three pictures was achieved, moving from a 10dB peak-to-peak difference over 5nm to less than 2dB even though periodic modulations of the spectrum were present. During this optimisation, output power was of XW and no difference of power was seen despite the fact that the spectral power density was decreased for shorter wavelengths and increased for longer wavelengths, the latter having a smaller gain than the first and the pump power was unchanged.

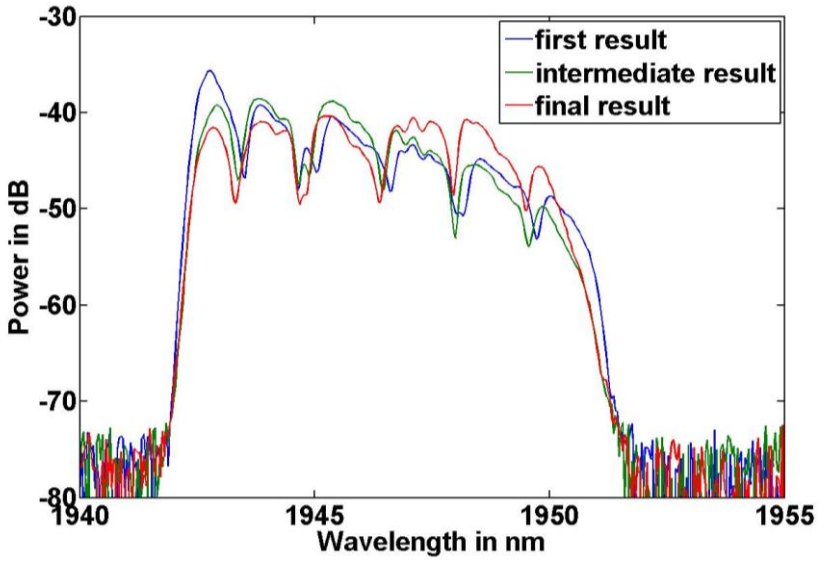

Figure 6.12 Evolution of output spectrum through picture shaping to achieve flatness

A periodic modulation on the spectrum can be seen with a period of 1.5nm. This was thought to be caused by an etalon effect between the fibre tip end in the feedback arm and the 4.5mm focal length B-coated lens used for collimation in the feedback arm, as B-coating has a reflectivity of less than a Fresnel reflection below 1850nm but goes up to 15% over 1950nm. Calculation of the spacing corresponding to the measured period gave an etalon spacing in air of 1.27mm and does not correspond to the collimated lens working distance. These periodic modulations were however suppressed by switching the collimating lens with an equivalent uncoated one.

A second method to adjust SPD whilst operating in a multiband regime is available by modification of the DMD pattern. Adjustment of the SPD can be achieved by modification of the reflective pixel density of the “on-state” areas on the DMD, creating ‘grey’ shades. Figure 6.13 shows a picture sent to the DMD, comprising three reflective bands with the middle one having a ‘grey’ shade and two spectra corresponding to these three bands. Firstly, a bitmap with three separate fully reflective areas was sent to the DMD, generating a particular spectrum (blue trace) but in the second instance, the red trace, the central bitmap line was patterned with alternating black and white pixels, creating a "grey" line. The reduced feedback at this position, and subsequently at these wavelengths, causes the spectral power density in that region to drop relative to the other regions. Adjustment of the reflective pixel density allows modulation of the SPD by decreasing feedback efficiency of a certain waveband, thus decreasing the output power contained in it. A drop of the SPD by more than 15dB for the central band was observed after use of a ‘grey’ shade as its reflective pattern. The DMD patterning can be coded to produce many combinations of spectral bands and relative spectral powers due to the multiple shades of ‘grey’ available. The system optics limits the minimal wavelength spacing between two spectral bands as when two reflective areas are positioned too close to each other, they act as one broader reflective area. This example shows both wavelength selection and relative spectral power control using the DMD only. Moreover, feedback can be adjusted to modify output spectrum in real-time as the DMD can be updated at a frequency of up to 1kHz, and even higher depending on the DMD and software used.

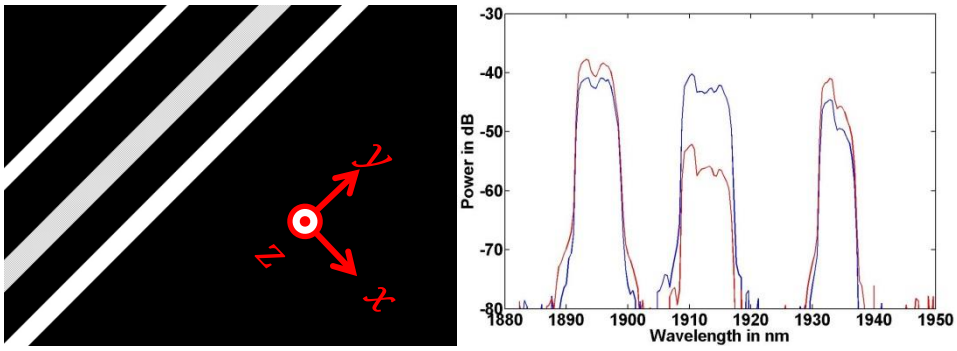

Figure 6.13 SPD control of a multi-waveband ASE spectrum

To achieve accurate control over the SPD with high precision of the amount of power enclosed in each spectral band and without SPD drops due to gas absorption lines, an enclosed area needs to be used to avoid water vapour and CO_2 lines forbidding some wavelengths to be generated particularly around 1900nm. Modification of the imaging system combined with a larger DMD with a smaller pitch size would allow broader and more accurate tuning of the output spectrum and therefore, the DMD would provide higher control over the spectrum. The maximum and minimum available wavelengths are determined by the angle of the grating and the DMD position (for a chosen DMD size and imaging system). As the DMD is fixed, only a rotation of the grating can change these extrema.

This source offers ASE generation with intra-cavity control over the output spectrum and its SPD, however, due to the core-pumping configuration and low Tm dopant concentration fibre, the generated spectrum is shifted towards the short wavelength end of the Tm emission spectrum which is not suitable for power scaling with high

dopant concentration cladding pumped fibre amplifiers. Core-pumping of active fibres is often detrimental to long wavelength operation in the active ion emission band and thus the cavity is unable to operate at these wavelengths. For future amplification schemes, cladding-pumping is required as high-power laser diodes are not compatible with core-pumping due to their high NA and delivery fibre sizes. Cladding-pumping of Thulium doped fibres implies high dopant concentration to compensate for the pumping architecture which leads to much higher reabsorption losses towards short wavelengths and higher gain towards long wavelengths of the emission band. Therefore, seed sources generating wavelengths over 1950nm are mandatory for efficient amplification through cladding-pumped Tm-fibre based power amplifier stages.

6.4 Cladding-pumped ASE source

6.4.1 Experimental setup

An ASE source based on cladding-pumped architecture for long wavelength generation was built in order to achieve high compatibility with a future amplification scheme. Figure 6.14 shows the setup used which comprises a 3m-long 2wt% Tm-doped active fibre with a 10µm core diameter and 125µm inner-cladding diameter and a 0.17 NA for the core and 0.146 for the inner-cladding. This fibre was cladding pumped at 793nm by a 35W laser diode. The active fibre was perpendicularly cleaved at one end, acting as output coupler, and angle-cleaved at the other end. The cavity contained a free-space feedback arm to allow spectral shaping. This feedback arm comprises an AOM, a diffraction grating to spatially chirp the beam along the x axis and a set of lenses to image the fibre tip onto a DMD for accurate wavelength selection. The AOM used here is the same a previously used in the core-pumped setup. The diffraction grating is blazed at 35° with a pitch of 600lines/mm. The set of imaging lenses are a 4.5mm uncoated aspheric and a 150mm plano-convex one anti-reflection coated at 2µm. The repetition rate of the AOM is set at 150kHz with a 20% duty cycle. This repetition rate was selected to ensure that no mode-locking occurs and the duty cycle was reduced to maximise peak power.

The DMD can then be configured to reflect different wavelengths according on the zone active on the DMD. Such a system has the same mechanics and variables as the tunable laser utilising a DMD previously demonstrated (Chapter 5).

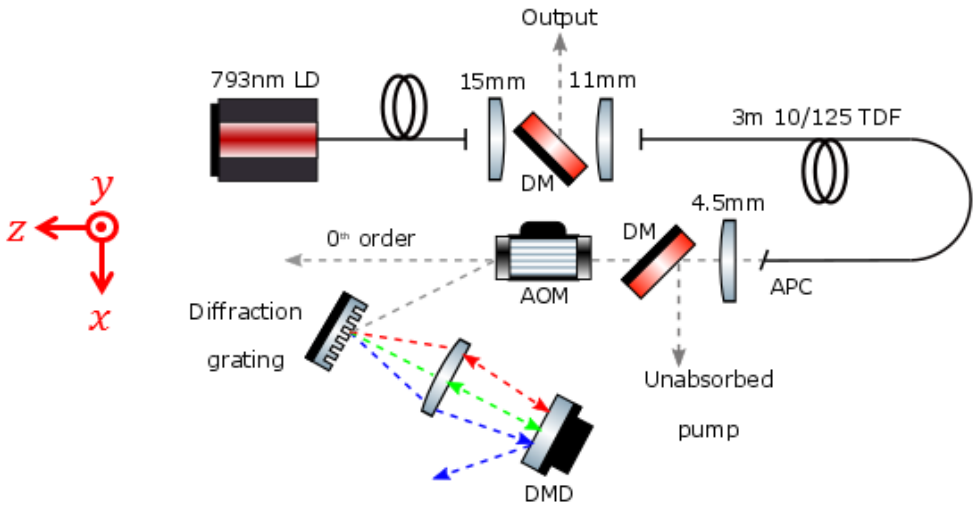

Figure 6.14 Cladding-pumped tailored ASE setup for emission centred at 1970nm

This setup based on a cladding-pumping scheme at 793nm allows us to take advantage of the cross-relaxation phenomena occurring in Tm fibres, increasing slope efficiency and allowing longer output wavelengths due to the higher dopant concentration. The grating was angularly aligned to allow generation of long wavelengths, required by the future use of an amplification stage. To avoid parasitic lasing at shorter wavelength, a short 50mm piece of Ho-doped 10/125µm active fibre was added inside the cavity, spliced between the active Tm-doped fibre and the APC connector. Ho-doped silica fibres possess a high absorption peak centred at 1950nm, creating high losses at this wavelength for the cavity, forbidding parasitic lasing to occur at this repetition rate by dropping the cavity gain around 1950nm. By increasing losses at 1950nm, the threshold for parasitic lasing increases and, coupled with the low feedback at this wavelength, is higher than the maximum pump power.

Long wavelengths are often targeted for future amplification: amplification stages at 2µm mostly use 793nm laser diodes as pump source as they are commercially available at high power whilst 1550nm pump sources consist on Er:Yb lasers which are often less reliable, more expensive and offer lower power. 793nm laser diodes achieve high output power but have high NA (0.15 or 0.22) and are delivered through a 105/125µm fibre or larger, forbidding core-pumping architectures to be used. As cladding-pumping is then compulsory for these diodes, the active fibre doping concentration required to achieve high efficiency is of more than 2wt%, creating high reabsorption losses, especially below 1950nm (CF Chapter 2, Figure 2.2). Thus, amplification stages would often require the use of a signal above 1950nm to avoid inefficient amplification and parasitic lasing. The second ASE source configuration shown in Figure 6.14 is therefore more suitable with future amplification.

6.4.2 Results

Moving to a higher dopant concentration in the fibre core for cladding pumping allows for generation at longer wavelengths by improving gain at these wavelengths and increasing reabsorption losses at short wavelengths. Such a change would normally allow a smoother output spectrum as many of the atmospheric absorption lines detrimental to thulium fibres are concentrated between 1800 and 1920nm [6.22]. Figure 6.15 shows the ASE

spectrum obtained by using the cladding pumped source described above: the output spectrum is shown at two different repetition rates of 100 and 150 kHz, the first one being broader. A quasi-continuous spectrum is obtained with few pits only located around the shorter wavelengths. These pits correspond to water vapour absorption features but are quite minute compared to the previous result as most of the water vapour absorption lines are located below 1920nm. Thus smooth output spectrum can be achieved. A broader spectrum is generated by reducing the AOM repetition rate. By reducing this rate, more time is allocated for energy storage and wavelengths situated at the edges of the available spectrum (below 1920nm and above 2000nm) will have more gain, therefore increasing the spectral power density away from the central wavelength. The spectra displayed were centred at 1960nm with an average output power of 8W, limited by the available pump-power, and with a FWHM of 20.4nm for both repetition rates. Bandwidth at 10dB is of 37.5nm for a repetition rate of 100kHz compared to 35.6nm for a 150kHz repetition rate. With such a configuration, maximal gain is achieved in the 1950 to 2000nm which corresponds to what is theoretically expected. The ASE output spectrum is also shown in a linear scale in Figure 6.15 for a repetition rate of 100kHz, corresponding to the orange curve in the dB graph.

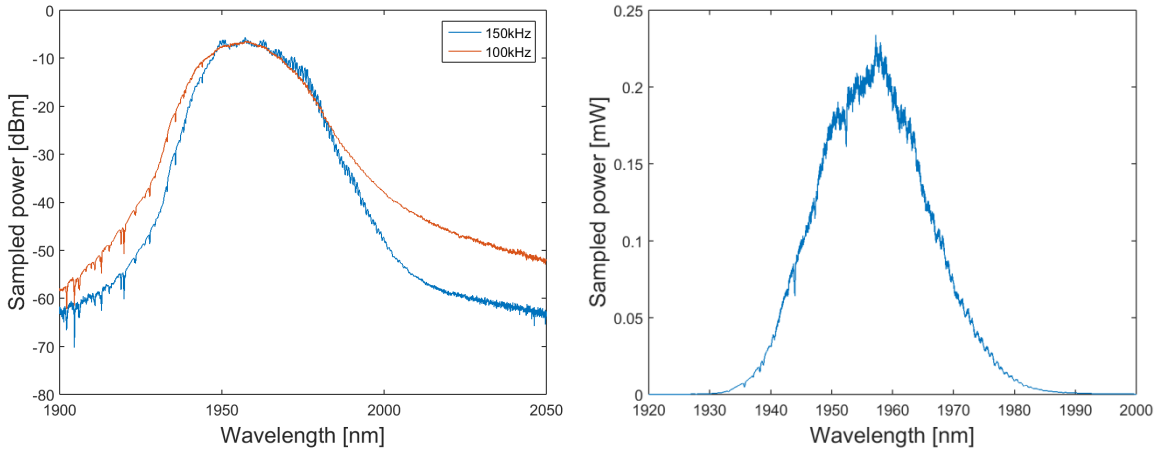

Figure 6.15 Broad pulsed ASE output in cladding pumping architecture for long wavelengths generation

The output spectrum can be tailored by configuring the reflective pattern of the DMD; combination of the diffraction grating, the imaging system (composed of two lenses) and the DMD allows a wavelength-dependent controllable feedback. Control of the number of output wavelength bands, their respective positions and widths is possible by adjustment of the DMD reflectivity pattern. Figure 6.16 shows seven different spectra obtained for various configurations of this DMD reflectivity pattern. By moving the position of the reflective area on the DMD, wavelength tuning from 1960nm to 2020nm was achieved with maximum output power of more than 7W at the central wavelength of 1990nm, corresponding to a slope efficiency of ~26%. This cavity previously yielded a slope efficiency of 32% in a tunable laser configuration (see Chapter 5). Here, by adding an AOM inside the cavity, feedback efficiency is dropped by 50 to 75% compared to laser configuration as the light is not polarised in the cavity, leading to a maximum diffraction efficiency of the AOM of 50% single-pass. Such a drop of the feedback arm reflectivity when compared with the maximum output power obtained in laser configuration gives a theoretical slope efficiency between 24 and 28%. The measured value is in the middle of the theoretical

window. Switching to high efficiency polarisation maintaining fibres should improve slope efficiency to values close to 32%.

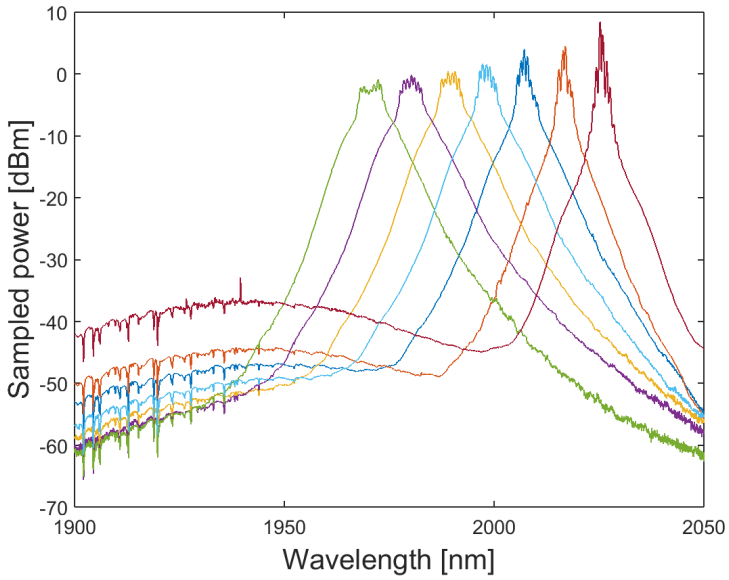

Figure 6.16 Example of ASE spectra obtained in a cladding-pumping architecture utilising different reflective band of 50 pixels width across the DMD

As the output wavelength is pushed towards longer wavelengths, the overall efficiency of the cavity decreases due to a drop in feedback, lower gain at long wavelengths, leading to lower output powers and a higher broad ASE background as seen on Figure 6.16. Tuning is demonstrated here from 1970 to 2020nm with an output power of 8W at 1970nm and down to 5W at 2020nm. The FWHM evolved throughout the experiment from 7nm at 1970, down to 4nm at 2000 and below 2nm at 2020nm. Parasitic lasing was observed for the far edge of the available tuning range caused by the low efficiency and high threshold of the cavity at this wavelength. Gain at the wavelength selected by the DMD of around 2020nm was equivalent to the gain level of wavelengths around 1940nm even though the latest were not fed back into the cavity by the DMD. This parasitic lasing was only visible at maximum pump power as when pump power increases, small unwanted reflections from lenses for example would lead to the apparition of an oscillator cavity and accordingly parasitic lasing.

Figure 6.17 shows the evolution of pulse duration as a function of repetition rate of the AOM for 7 different wavelengths. All these measurements were done at full pump power with a duty cycle of 20% using a biased InGaAs DET10D detector from Thorlabs with a rising time of less than 25ns. An example of pulse shape is also included in Figure 6.17 and shows that the AOM duty cycle is optimised to allow pulse extraction just before being turned off.

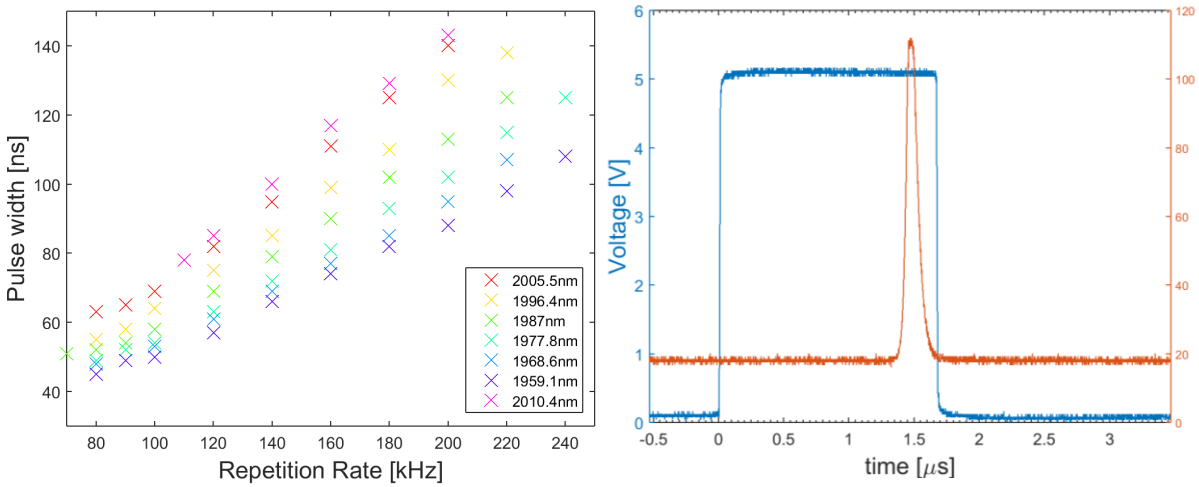

Figure 6.17 Evolution of pulse width as a function of repetition rate and wavelength.

By decreasing the repetition rate, pulse width decreases, going from 140ns at 220kHz and 2010nm to less than 60ns at 80kHz and 1960nm. By decreasing the repetition rate whilst conserving the same duty cycle of 20%, the cavity 'off' time increases, leading to higher population inversion and, accordingly, to higher small signal gain which results in shorter pulses being generated. Moreover, the shorter the wavelength, the shorter the pulses due to the higher gain of the cavity at these wavelengths. Measurements were stopped at 80kHz for most wavelengths (110kHz for a wavelength over 2010nm) as parasitic lasing started to occur. By reducing repetition rate , the cavity 'off' time increases, allowing the build-up of CW ASE in between the pulses and starts extracting cavity inversion which leads to parasitic. Parasitic lasing appears at higher repetition rates for long wavelengths over 2010nm because of the lower gain at these wavelengths, leading to lower energy extraction during the cavity 'on' time.

Figure 6.18 shows the evolution of calculated peak power as a function of repetition rate for the same 7 different wavelengths. The calculations were done by combining the pulse widths measured previously and displayed in Figure 6.17 and the average output power measured with a Gentec 15W powerhead. Previous results demonstrated a decrease in pulse width with repetition rate. As average output power is conserved for a specified wavelength, higher peak power is achieved when reducing RPF. Calculations showed a peak power going from 200W at 220kHz to more than 1500W at 80kHz. Moreover, the shorter the wavelength, the higher the peak power, due to shorter pulses and higher slope efficiency (i.e. higher output power).

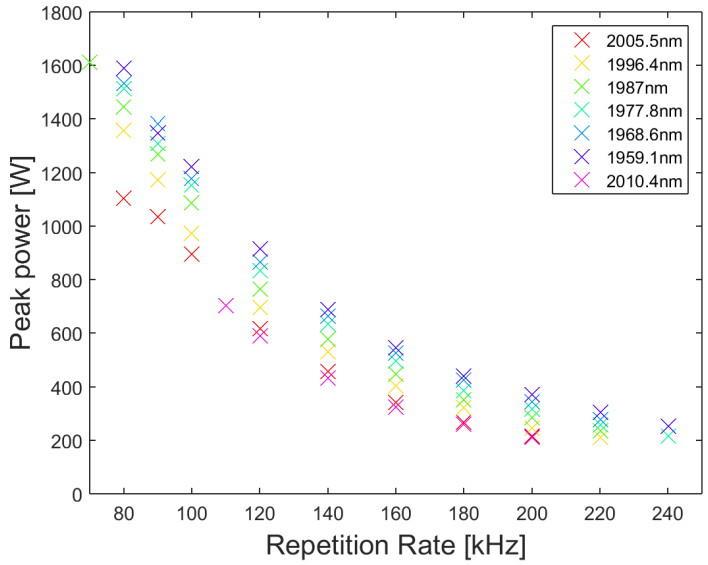

Figure 6.18 Evolution of peak power as a function of repetition rate and wavelengths

6.5 Amplification

6.5.1 Experimental setup

An amplifier stage was designed to amplify the ASE source previously described in Section 6.4 in order to reach output peak powers high enough to pump and reach threshold in a future ZGP OPO cavity discussed later on in Section 6.6. Figure 6.19 shows the amplification stage which contained a 6+1:1 combiner to inject the signal into the core of a 10/200µm 0.15/0.46NA Tm-doped active fibre with a dopant concentration of 3.5wt% whilst six 105/125µm 35W diodes at 793nm with a NA of 0.22 are injected into the inner-cladding for cladding-pumping. The seed was injected into the amplifier through an angle-cleaved SMF28e fibre end to avoid feedback at the injection point; a Fresnel reflection occurs when entering the amplifier stage which would have been fed back into the seed source if the amplifier input port was a flat cleave. This reflection could have greatly destabilised the seed ASE as it would have been equivalent to the output coupler reflectivity. An isolator was also added between seed and amplifier to avoid feedback from the amplified signal into the seed source. A 20dB tap coupler was used to monitor the seed spectrally and temporally as well as monitoring feedback levels from the amplifier. An InGaAs photodiode was used for feedback monitoring, allowing small signal detection to prevent feedback-related issues. The active fibre used was 4m long to maximise pump absorption (here around 9dB) whilst decreasing risk of SBS and SRS, whose thresholds are dependent on the gain media length. The calculated thresholds (from formula provided in Chapter 2 with a coefficient α close to 0) are for a 4m-long fibre of.108kW for SBS (considering a FWHM of 3nm i.e. 220GHz) and 320W for SRS. The active fibre was terminated by an 11° angle-cleaved endcap with a length of 300µm, avoiding end-facet damage by expanding the beam before exiting the fibre and forbidding the Fresnel reflection to be guided into the core. The beam was then collimated by an off-axis parabola (OAP) gold mirror instead of a lens to avoid thermal lensing and possible damage

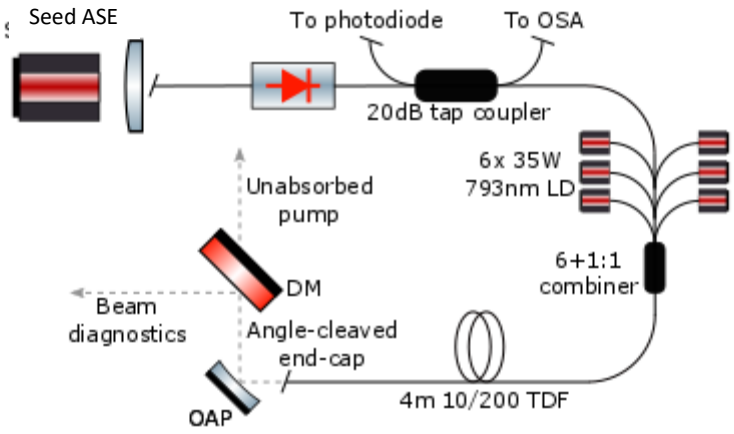

Figure 6.19 Schematic of amplifier stage for pulsed ASE amplification

For efficient amplification, the seed is required to be over 1950nm to increase compatibility with a cladding-pumped fibre amplifier and avoid reabsorption. Such fibre amplifiers require high doping concentration to operate efficiently and promote cross-relaxation when pumped at 793nm. The seed used here is configured to operate over 2µm to achieve high compatibility with the amplifier whilst allowing ZGP OPO pumping after amplification.

6.5.2 Results

A spectrum at 2010nm (dark blue curve in Figure 6.16) with a bandwidth of less than 10 nm is generated from the seed by using a 50 pixels wide reflective area on the DMD and then injected into the amplification stage. A repetition rate of 150kHz was selected to ensure proper ASE behaviour and avoid parasitic lasing. Figure 6.20 shows the amplified output power as a function of pump power, the latter corresponding to the absorbed pump power and a slope efficiency of 56% with a maximal amplification of 14 dB reaching 72W is achieved limited by available pump power.

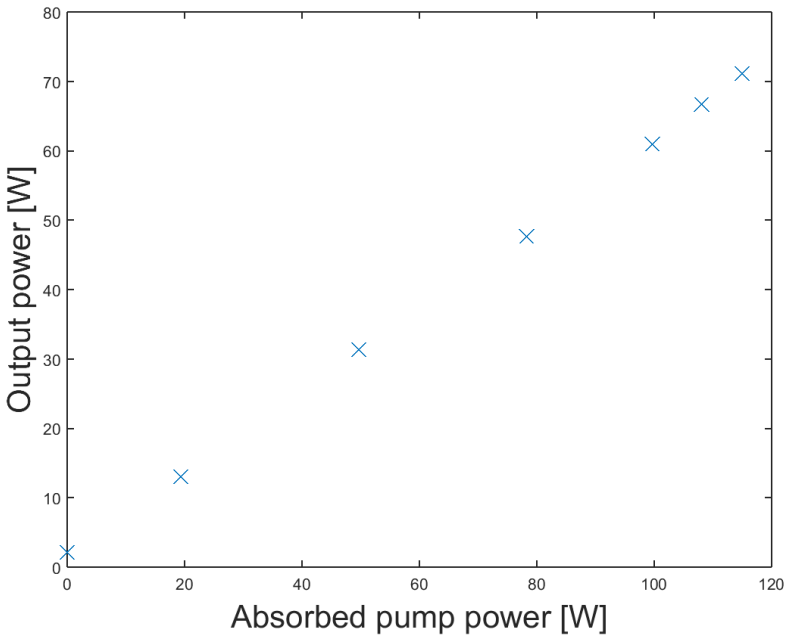

Figure 6.20 Output power versus pump power during amplification

Evolution of the output spectrum was studied during amplification for a repetition rate of 180kHz. Figure 6.21 shows this evolution at 180kHz for different amplification ratios and slight broadening of the central peak at 2010nm was observed combined with unwanted output power at shorter wavelengths (1950 to 1980nm).These wavelengths were only present in the seed source as background ASE but benefit from high gain in this fibre, as displayed by Figure 6.15. It is our belief that the 1950-1980nm spectral part of the amplified spectrum corresponds to this amplified ASE background remaining from the seed. This is confirmed by the decreasing amount of power contained in this spectral band when increasing pulse repetition rate. Background ASE is a CW signal which builds up by extracted pump inversion power. Such power is decreased when increasing repetition rate as the 'off' time of the cavity between pulses decreases. At high RPF, the seed spectrum is better defined with a lower unwanted ASE background and a sharper central peak. Thus, after amplification more output power is contained in the central peak, with the output power at shorter unwanted wavelengths stays significantly low. No parasitic lasing was detected during the amplification and this was confirmed by a temporal measurement with an InGaAs photodiode at the output of the amplifier. The latter still showed a single pulse with a constant pulse width equal to the seed pulse width and no background power.

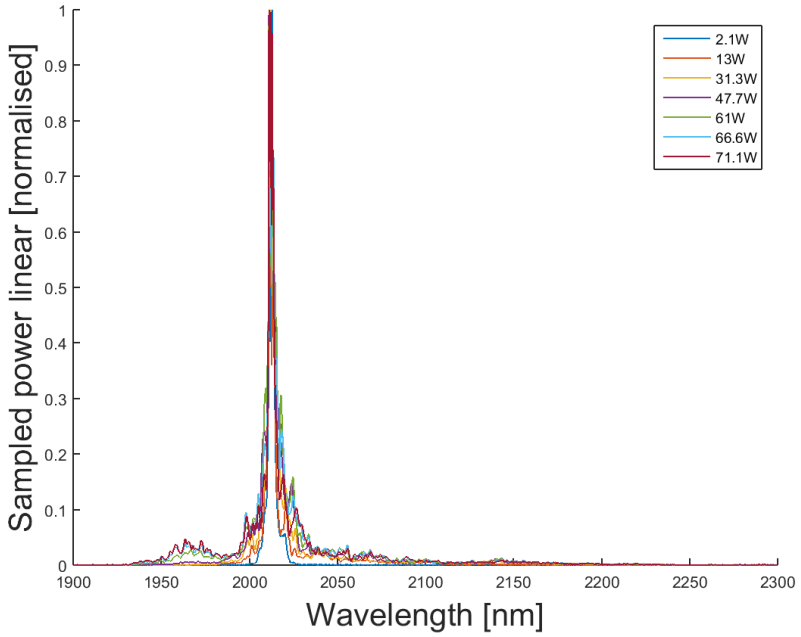

Figure 6.21 Evolution of output spectra during amplification at 180kHz

6.6 Preliminary design for optical parametric oscillator pumping

6.6.1 Introduction

This high-power ASE source main purpose was the pumping of a ZGP optical parametric oscillator (OPO) cavity to generate mid-infrared wavelengths (3-5µm). Pumping of ZGP crystals is often done by using a focused short pulse Ho:YAG laser at 2.1µm. Ho:YAG lasers are often pumped with a Thulium fibre laser, a Tm:YAP laser or Tm:YAG laser, at 1907nm. This OPO generates a signal and idler in output around 3.9 and 4.55µm respectively [6.23, 24]. These wavelengths are linked together as the pump energy equals the signal and idler energy combined after conversion, following:

$$\frac{1}{\lambda_{\text{pump}}} = \frac{1}{\lambda_{\text{signal}}} + \frac{1}{\lambda_{\text{idler}}} \tag{6.3}$$

As shown by this equation, by changing the pump wavelength or the phase-matching conditions, the signal and idler wavelengths can be adjusted [6.24, 25] to suit different needs. These wavelengths are of particular interest for many applications such as counter-measures and defence sector in general due to the atmospheric transmission windows around the 4µm wavelength as shown on Figure 6.22. The wavelengths generated by such an OPO would be situated just before the absorption zone at 4.2µm linked to CO_2 presence for the signal and just after this zone for the idler, allowing both of them to freely propagate without being absorbed.

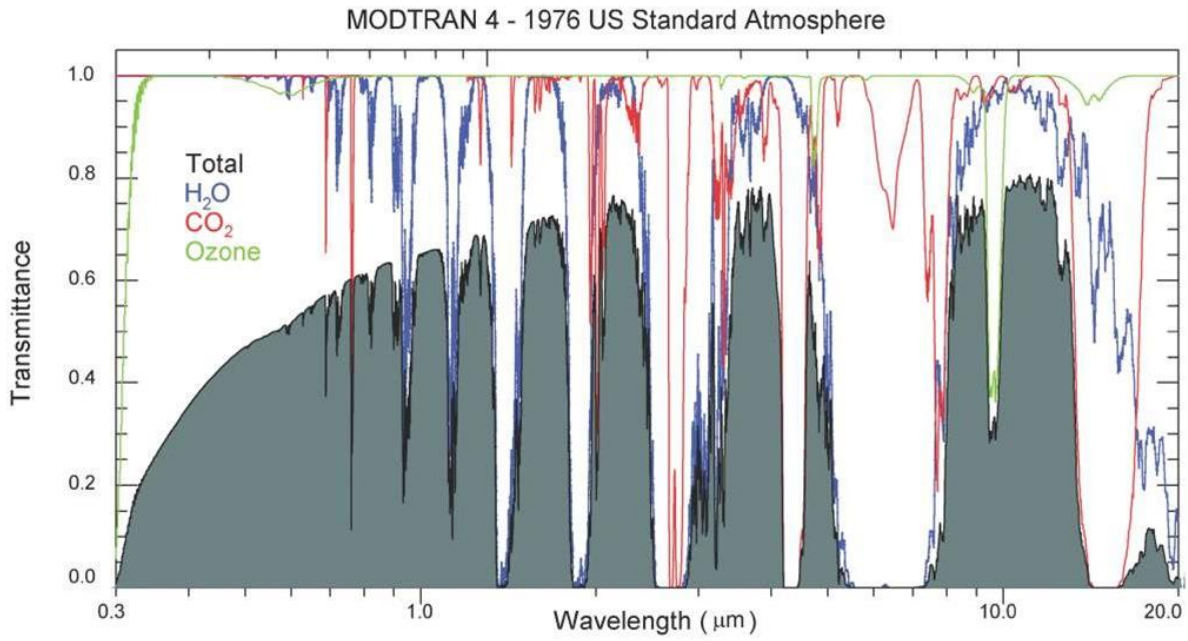

Figure 6.22 Atmospheric transmission from 0.3 to 20µm with absorption features corresponding to H_2O, CO_2 and ozone, from [6.26]

Singly-resonant ZGP OPO cavities are composed of a ZGP crystal and two mirrors to form a cavity. Such cavities are based parametric oscillation which utilises the crystal non-linear properties. To reach threshold and achieve high photon conversion, high pump power is required i.e. high energy density. Therefore, pulsed pumps are often used due to their high peak power. Such energy levels are commonly achievable in crystal-based lasers due to high energy storage capability and the ability to easily obtain relatively short pulses in Q-switching regimes. Pulsed fibre based 2µm lasers, however, generate longer pulses and have a much smaller energy storage capability before the onset of non-linear issues such as SBS, SRS or fibre damage. As a consequence, this pumping scheme requires the use of fibre amplifier stages in order to easily reach threshold and multi-mode active fibres could be used in order to achieve higher energy storage and amplification without breakage.

However, the use of multi-mode fibre amplifiers leads to beam-pointing instabilities coupled with temporally instable beam profiles which are detrimental for efficient OPO pumping. ZGP OPO cavities have a high threshold which often requires high focussing of the pump in order to achieve high pump energy density inside the crystal and reach threshold with relatively low peak power in comparison. Such beam profile and pointing instability would lead to instabilities in the OPO cavity, forbidding proper alignment. Therefore, a pump system achieving high beam pointing stability and good beam profile in output of multi-mode fibre amplifiers is essential. As explained previously, due to their short temporal coherence lengths, ASE sources are of great benefits for OPO pumping but require accurate tailoring of their spectrum to target the desired pump wavelength and fit into the crystal's phase-matching bandwidth. Moreover, variation of the ASE bandwidth at FWHM might permit to adjust the phase matching conditions of the cavity and lead to tuning of the output wavelengths position and linewidth.

6.6.2 Experimental setup

Figure 6.23 shows the OPO cavity used here where both mirrors had a curvature radius R of 250mm. The amplified ASE was polarised before injection into the ZGP crystal, losing 50% of the power and focused through a plano-convex lens. An isolator was placed at the output of the amplifier after the polariser to avoid any unwanted reflection from one of the OPO cavity mirror to be fed back into the amplifier stage and causing damage. Two dichroic mirrors were put on the output path of the OPO cavity, separating pump, signal and idler. A wedge was also added after the first dichroic mirror for beam diagnostics such as spectrum and beam quality measurements.

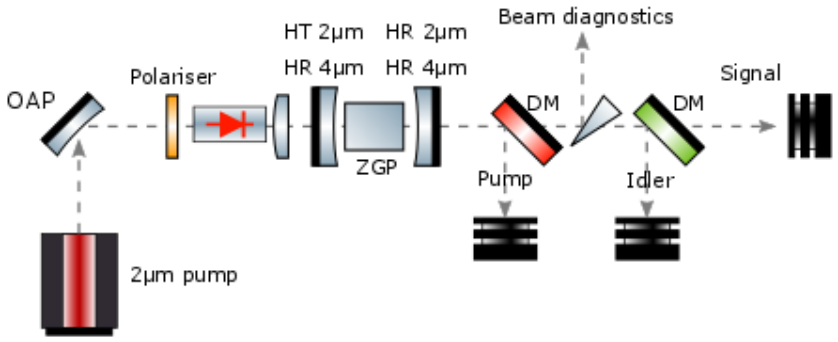

Figure 6.23 Linear ZGP OPO cavity pumped by polarised ASE at 2010nm for mid-IR generation

To achieve high efficiency in the OPO cavity, mode-matching of the pump and signal waist sizes must be realised. This OPO cavity is symmetrical and has an optical length 2d of around 20mm, giving a waist radius ω_0 for a wavelength at 4µm of $250\mu m$ following the formula:

$$\omega_0 = \frac{\lambda}{\pi}\sqrt{d(R\text{-}d)} \tag{6.4}$$

In order to achieve high efficiency in the OPO cavity, the pump spot size must match as closely as possible with the signal spot size calculated in equation (**6.4**).

$$\omega_0 = \frac{\lambda}{\pi\theta} = \frac{\lambda f_2}{\pi \emptyset_{rad}} = \frac{\lambda f_2}{\pi f_1 NA} \tag{6.5}$$

With f_1 the focal length of the lens used for collimation after the amplifier stage, f_2 the focal length of the lens used to focus in the ZGP crystal, λ the pump wavelength, NA the amplifier stage fibre NA, θ the diverging angle at the output of the amplifier stage and $\emptyset_{rad}$ the beam radius after collimation of the amplified ASE. This setup consists in imaging the amplifier fibre core into the ZGP crystal; as this fibre has a core radius of 5µm, the ratio $\frac{f_2}{f_1}$ must be of 50 to perfectly match with the signal waist size. A focal length of 750mm was selected to match the off-axis parabola used at the amplifier output for collimation which had a focal length of 15mm and plane high-reflectivity mirrors at 2µm were added in the setup to increase beam path whilst minimising footprint.

Approximate threshold can be calculated from previous results obtained with the ZGP crystal used here. This crystal, supplied by Leonardo Airborne & Space Systems, and in their system achieved a threshold of 2MW/cm^2, corresponding to an energy density of 0.07J/cm^2 when pumped at 2.1µm by a Ho:YAG laser yielding 35ns pulses at 30kHz, according to our supplier. The pulse length was measured for 2 RPF 150 and 180kHz and stayed close to 100ns with a maximum output power of 72W after full amplification. The peak power P_{peak}, pulse energy E, power density I and energy density $E_{density}$ were approximated for a top-hat beam focused in the ZGP crystal with a waist of 250µm fitting with the cavity mode radius and taking into account that half of the output power was lost through the polariser at the output of the amplifier stage.. Peak power, power density and energy density are summarised in Table 6-1 for the two repetition rates of 150 and 180 kHz for an output spectrum centred at 2010nm after full amplification, reaching 72W of output power.

RPF [kHz]	150	180
P_{peak} [kW]	2.35	1.95
I [MW/cm^2]	1.2	0.99
$E_{density}$ [J/cm^2]	0.12	0.1

Table 6-1 Power density and energy density reached by focusing the ASE source into the ZGP crystal for different RPFs

The values shown here correspond to unpolarised outputs. Thus, after polarisation, 50% of the generated power is dumped, achieving energy density of up to 0.1J/cm^2 which is still higher than the specified threshold of 0.07J/cm^2 given by our supplier.

Decrease of the repetition rate is a possible way to easily reach threshold inside the OPO cavity, however, as shown previously in Section 6.5 smaller RPFs lead to broader output spectra with undesired ASE generated at short wavelengths. Thus, even though energy density in the ZGP crystal would be higher, less energy would interact for mid-IR wavelength generation due to the crystal working efficiently only for long pump wavelengths. Moreover, a ZGP crystal has a phase-matching bandwidth of few nanometers, thus a too broad ASE source would not be suitable as the system would require the energy contained in the phase-matching bandwidth of the pump to reach calculated threshold from Table 6-1.

Figure 6.24 shows a schematic of the entire setup for ZGP OPO pumping by using a MOPA ASE source based on the tunable ASE seed source described in Section 6.4 and the amplifier stage detailed in Section 6.5.

Pumping of the OPO cavity was done at full pump power corresponding to 72W exiting the amplifier with a pulse repetition rate of 180kHz to minimise spectral broadening during amplification in order to have most of the pump power inside the phase-matching bandwidth of the ZGP crystal.

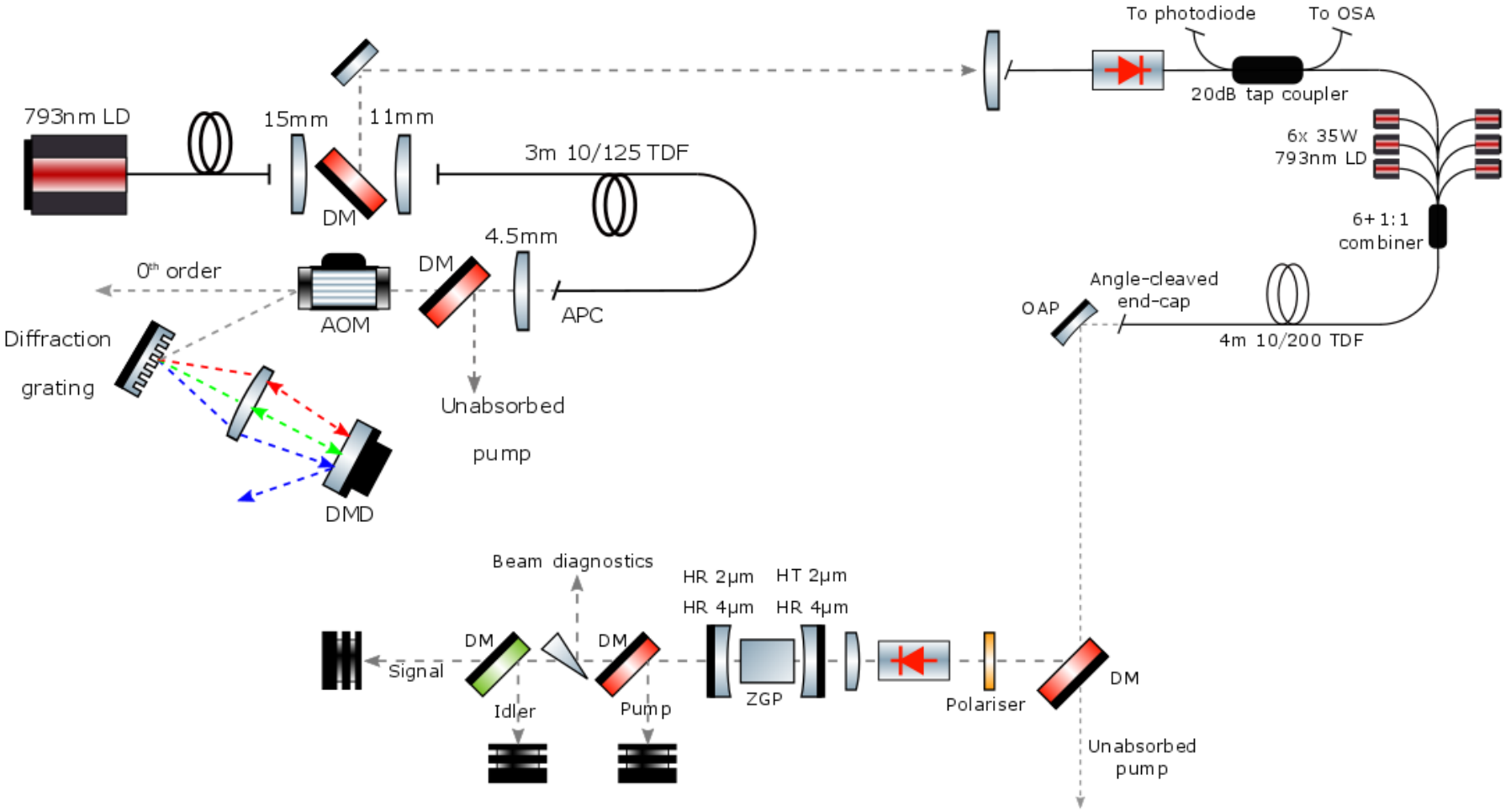

Figure 6.24 Full setup for ZGP OPO consisting in a tunable ASE seed source, an amplifier and an OPO cavity for mid-IR generation

Less than half of the generated pump power was injected into the crystal mainly due to the polariser reflecting half of the power but also the isolator and other optical components not being perfect. No mid-IR generation was achieved as available pump power reaching the crystal might not be sufficient to reach threshold as previous calculations where only a guideline obtained by scaling results from an experiment from the company lending us the crystal. Moreover, beam degradation of the remaining pump after the cavity was observed for amplification greater than 11dB, whilst the amplifier output did not suffer from beam degradation. This can be caused by deformation of one of the optic from thermal effects, either a lens or a mirror and might require careful diagnostics to identify which element is at fault.

Future pumping of this cavity therefore requires realignment of the cavity to ensure no pump beam degradation and, accordingly, high mode matching between pump and signal intra-cavity. Higher amplification is also required to achieve pump power levels significantly high to easily reach threshold. This can be done by moving to multi-mode doped fibres to increase energy storage capabilities, decrease thermal loading and increase non-linear effects thresholds. Moreover, the addition of a significantly larger end-cap to ensure no feedback from the fibre end into the amplifier and avoid end-facet damage would be of great benefit.

6.7 Future developments

Future steps for this project can already be discussed as some improvement to the actual system are rapidly achievable. The need for a polarised output to pump a ZGP OPO would require using seed/amplifier stages comprising PM fibres, avoiding a net loss of more than 50% of the output power before reaching the ZGP crystal. Such Tm fibres are already commercially available but literature shows that much lower slope efficiency are achieved within these fibres compared to non-PM ones, reducing overall output power at the end of the amplifier stage for a constant pump power value. However, non-PM fibres scramble polarisation over their entire length, thus, as the amplifier stage presented here only has a total fibre length of few meter, the use of a polarised seed with a non-PM amplifier fibre could be thought of, its short length ensuring that most of the amplified power stays linearly polarised. This polarised system would allow to double the available output power for OPO pumping whilst conserving the same amount of laser diode pump power.

The addition of a larger endcap at the end of the amplification fibre would allow to reach higher amplification values, up to 20dB gain without damaging the end-facet. This would require more pump power and better thermal management of the amplification as well as careful monitoring of the feedback levels inside the amplifier to avoid any damage.

Reduction of the OPO threshold is also possible through different scheme such as reduction of the cavity length to minimise signal waist size and therefore, by reducing the pump size to match it, an increase of pump power density inside the crystal would occur.

6.8 Conclusion

This chapter's point of focus was the creation of a MOPA system to generate tunable pulsed ASE achieving high peak power over 2µm. this source was here used to pump a ZGP OPO cavity for mid-IR generation but could be used for a variety of applications

Pulsed ASE sources allowing wavelength-selective feedback whilst forbidding lasing by utilising an AOM intra-cavity are demonstrated. This technique was based on previous work conducted by Jae Daniel [6.8] at the Optoelectronics Research Centre which showed that by exploiting the fast dynamics of a Q-switched fibre based cavity and its high small signal gain, fast pulse build-up occurs and pulse energy is extracted before the establishment of longitudinal modes. As this technique is based on the cavity dynamics rather than on feedback suppression, feedback is tolerated and can be used for wavelength-tuning.

An ASE source, core-pumped at 1550nm, achieved emission towards the short wavelength part of the broad emission band of the Thulium ion. This configuration with a low fibre doping concentration and a core-pumped architecture offered the possibility of generating ASE around 1880nm. The AOM was configured to operate at a repetition rate of 150kHz and a duty cycle of 20%. This value was chosen to maximise output power, switching the cavity back to its 'no feedback' configuration just after pulse extraction to ensure no longitudinal mode would appear. A wavelength-selective feedback arm was comprised in the setup by combining a diffraction grating and a DMD (as previously demonstrated in Chapter 5) and shaping of the output spectrum was demonstrated by utilising the advantages offered by the DMD, allowing generation of multiple wavebands in output with control over their position, width, shape and relative power through modification of the DMD reflective pattern. Up to 350mW of output was achieved, limited by the available pump-power. The source was tailored to achieve narrow-linewidth output and a FWHM as low as 0.15nm was demonstrated whilst conserving output power. As a proof of principle, shaping of an 8nm-wide output spectrum was demonstrated, improving its spectral power density flatness from 8dB to less than 2dB. A multi-waveband output spectrum comprising 3 spectral wavelengths was also generated and modification of their relative power was displayed whilst conserving the same output power.

For amplification purposes, seed spectrum over 1950nm was required to ensure compatibility between seed and the future amplifier stage which comprises a high dopant concentration fibre in a cladding-pumped configuration, making the core-pumped ASE source unsuitable for amplification. A cladding-pumped ASE source achieving emission in the long wavelength part of the Thulium ion emission band was demonstrated. Moving from core to cladding-pumping and from low to high dopant levels permitted emission over 1950nm, here up to 2025nm. Tuning from 1970nm to 2025nm was demonstrated with FWHM at 3dB of few nm. A study of pulse width and peak power as a function of output wavelength and repetition rate was performed and pulses as short as 60ns were achieved with peak powers up to 1.5kW (corresponding to an average power of 7W). This source was set-up to operate at 2010nm to ensure good amplification as shorter wavelengths would be subject to high re-absorption losses in the amplifier stage. The selected wavelength also ensured no parasitic lasing would occur in the amplifier and high compatibility with the ZGP crystal.

An amplification stage was built around a 6+1:1 combiner where the ASE seed was injected in the fibre core and cladding-pumped by six 35W laser diodes at 793nm. The fibre was terminated by an angle-cleaved endcap to ensure low feedback and avoid facet damage. The active fibre length was kept to a short value of 4m to avoid SBS and SRS by increasing their threshold (CF Chapter 2). Amplification of 14dB up to 72W corresponding to a slope efficiency of 56% relative to absorbed pump power was achieved at different repetition rates and was pump limited. No feedback from the amplifier stage to the seed was detected and no beam degradation in output was detected.

A scheme for OPO pumping was designed, utilising the high power ASE for pumping. The novelty of ASE of pumping resides in the spectral width of the pump spectrum which might offer control over the generated signal bandwidth.

6.9 References

6.1. Cheung, C.S., et al., *Optical coherence tomography in the 2μm wavelength regime for paint and other high opacity materials*. Optics Letters, 2014. **39**(22): pp. 6509-6512.

6.2. Huang, D., et al., *Optical Coherence Tomography*. Science, 1991. **254**(5035): pp. 1178-1181.

6.3. Lefèvre, H.C. *Fundamentals of the Interferometric Fiber-optic Gyroscope*. in Optical Fiber Sensors. 1996. Sapporo: Optical Society of America.

6.4. Yoda, H., P. Polynkin, and M. Mansuripur, *Beam quality factor of higher order modes in a step-index fiber*. Journal of Lightwave Technology, 2006. **24**(3): pp. 1350-1355.

6.5. Chan, J.S.P., et al., I*mpact of Modal Interference on the Output Beam Properties of Large-Core Cladding-Pumped Fiber Amplifiers*. 2008 Conference on Lasers and Electro-Optics & Quantum Electronics and Laser Science Conference, Vols 1-9, 2008: pp. 1782-1783.

6.6. Wielandy, S., *Implications of higher-order mode content in large mode area fibers with good beam quality*. Optics Express, 2007. **15**(23): pp. 15402-15409.

6.7. Daniel, J.M., et al., *Effect of seed linewidth on few-moded fiber amplifiers*. in CLEO: 2014. 2014. San Jose, California: Optical Society of America.

6.8. Daniel, J.M.O., *WAVELENGTH SELECTION AND TRANSVERSE MODE CONTROL IN HIGH POWER FIBRE LASERS*, in Faculty of Physical Sciences and Engineering, Optoelectronics Research Centre. 2013, University of Southampton.

6.9. Wang, P., J.K. Sahu, and W.A. Clarkson, *110 W double-ended ytterbium-doped fiber superfluorescent source with M-2=1.6*. Optics Letters, 2006. **31**(21): pp. 3116-3118.

6.10. Liu, J. and P. Wang, *High-Power Broadband Thulium-Doped All-Fiber Superfluorescent Source at 2μm*. Ieee Photonics Technology Letters, 2013. **25**(3): pp. 242-245.

6.11. Shen, D.Y., et al., *Broadband Tm-doped superfluorescent fiber source with 11 W single-ended output power*. Optics Express, 2008. **16**(15): pp. 11021-11026.

6.12. Wang, P., J.K. Sahu, and W. Clarkson, *High Power Single-ended Yb-doped Fiber ASE Source*. 2007 Conference on Lasers & Electro-Optics/Quantum Electronics and Laser Science Conference (Cleo/Qels 2007), Vols 1-5, 2007: pp. 1632-1633.

6.13. Kong, L.F., et al., *2W Yb-doped double-clad fiber superfluorescent source with 42 nm 3 dB bandwidth*. Optics and Laser Technology, 2005. **37**(8): pp. 597-600.

6.14. Schmidt, O., et al., *High power narrow-band fiber-based ASE source*. Optics Express, 2011. **19**(5): pp. 4421-4427.

6.15. Goldberg, L., et al., *High-power superfluorescent source with a side-pumped Yb-doped double-cladding fiber*. Optics Letters, 1998. **23**(13): pp. 1037-1039.

6.16. Schmidt, O., et al. *Relative intensity noise characterization of a linear polarized 1.1 kW fiber-amplified narrow-band ASE source*. in Frontiers in Optics 2011/Laser Science XXVII. 2011. San Jose, California: Optical Society of America.

6.17. Akcay, A.C., J.P. Rolland, and J.M. Eichenholz, *Spectral shaping to improve the point spread function in optical coherence tomography*. Optics Letters, 2003. **28**(20): pp. 1921-1923.

6.18. Sampson, D.D. and W.T. Holloway. *100 mW Spectrally-Uniform Broadband ASE Source for Spectrum-Sliced WDM Systems*. in Optical Amplifiers and Their Applications. 1994. Breckenridge, Colorado: Optical Society of America.

6.19. Espindola, R.P., et al., *80 nm spectrally flattened, high power erbium amplified spontaneous emission fibre source*. Electronics Letters, 2000. **36**(15): pp. 1263-1265.

6.20. RP Photonics Consulting GmbH. Available from: https://www.rp-photonics.com.

6.21. Sabert, H. and E. Brinkmeyer, *Pulse Generation in Fiber Lasers with Frequency Shifted Feedback. Journal of Lightwave Technology*, 1994. **12**(8): pp. 1360-1368.

6.22. J. Flaud, A.B., and N. Husson, *REFERENCES and SOURCES for HITRAN*. 2013(0, 4058–4097).

6.23. Hemming, A., et al., *99 W mid-IR operation of a ZGP OPO at 25% duty cycle*. Optics Express, 2013. **21**(8): pp. 10062-10069.

6.24. Budni, P.A., et al., *Efficient mid-infrared laser using 1.9-µm-pumped Ho:YAG and ZnGeP2 optical parametric oscillators*. Journal of the Optical Society of America B, 2000. **17**(5): pp. 723-728.

6.25. Vodopyanov, K.L., et al., *ZnGeP2 optical parametric oscillator with 3.8–12.4-µm tunability*. Optics Letters, 2000. **25**(11): pp. 841-843.

6.26. *http://modtran.spectral.com/*. Available from: http://modtran.spectral.com/.

Chapter 7. Conclusion

Thulium fibre lasers are of great interest for a wide range of applications due to their wide emission spectrum offering broad wavelength flexibility and the possibility of high output power through MOPA configurations as high power pump diodes are readily available. Throughout this thesis we demonstrate different improvements for fibre lasers in general followed by new wavelength-tuning schemes, and a novel route for controlled ASE generation. In this chapter we summarise the key results of this thesis and provide a conclusion to the work undertaken.

In Chapter 3 we investigate a new way to increase pump absorption in cladding pumped circular fibres by localised processing of the cladding to improve mode scrambling. We demonstrate a large improvement in pump absorption by creating localised sections of D-shaped fibre in a circular fibre. The fabrication process utilises a CO_2 laser to achieve localised ablation of the glass cladding to realise tapered sections, transitioning from circular to a D-shaped profile and back to circular. The fabrication setup used here requires stripping of the fibre before laser processing and protection or recoating of the uncoated section afterwards, making it delicate to achieve multiple processing operations in one fibre. This process allows full control of the mode scrambler length, including its maximal depth, length and the transition zone lengths to achieve adiabatic behaviour. An example over 1m of circular Tm-doped fibre shows pump absorption improvement from 1dB to 2dB using 3 one-millimetre-long D-shaped sections regularly distributed along the fibre length. This processed fibre reaches pump absorption levels equivalent to quasi-octagonal geometries for a same doping concentration and equivalent core-to-cladding ratio. A study of the of different parameters available to optimise the D-shaped profile is described, showing that a circular fibre regularly processed with less than 3% of its total length modified into a D-shaped profile offers satisfying results whilst retaining the ease of use for cleaving and splicing. Here, for the selected circular Tm-fibre, a D-shape profile with a total length of 7mm repeated every 30cm is suggested and first demonstrations show high mode scrambling efficiency. Lastly, a production concept is proposed, allowing this method to be conducted on a large scale during the fibre drawing process and calculations associated with this configuration are detailed. This fabrication method would offer reliability and simplify the fabrication process as the drawn fibre would be processed before coating. A CO_2 laser system delivering 10µs pulses at a steady rate of 10kHz with a peak power varying from 640 to 1040W would allow real-time processing of the drawn fibre whilst allowing 1mm wide tolerances on the fibre positioning.

In Chapter 4 we offer a new way of improving fibre tip movement insensitivity in free-space feedback arms by utilising a retro-reflector corner-cube as reflective element. Many fibre lasers utilise a free-space feedback arm to achieve different modes of operation such as a grating for wavelength-tuning or an AOM for Q-switching. Such cavities rely on high feedback from the free-space arm to operate and any fibre tip movement relative to the collimating lens, from vibrations for example, is detrimental to operation. The architecture proposed here is based on the retro-reflective property of the corner-cube, ensuring that fed back light reaches the core. This offers the advantage of being fully insensitive to vibrations, which is a main criterion for laser systems deployed for defence and sensing applications. Calculations are explained, comparing this new configuration to a plane

mirror and theory shows transverse movement tolerances in the order of few millimetres compared to previous tolerances which are of the order of a fibre core radius. The new tolerances are dependent on focal length, fibre NA and feedback arm length. Experimental results achieved in a simple linear cavity show the influence of focal length and free-space feedback arm length on fibre tip movement tolerances and agree with theoretical expectations. Increase of focal length and decrease of feedback arm length lead to improved tolerances with an improvement by more than two orders of magnitudes (>1mm), which is demonstrated in a configuration where the feedback arm length is twice the focal length. A comparison is made between the plane mirror and the corner-cube configuration maximal output powers, and the corner-cube reflectivity of 67% is deduced. Low levels of feedback are achieved in this configuration with an overall reflectivity of the feedback arm of 26%, but this still leads to high efficiency with 80% of the generated power exiting the cavity through the output coupler.

Exploiting this new movement tolerance improvement, the second half of Chapter 4 focused on utilising transverse fibre tip movement for accurate wavelength-tuning in a ring laser configuration. A unidirectional ring Tm-fibre laser was constructed using a circulator, allowing the use of a feedback arm. This feedback arm comprises a collimating lens, a Fabry-Perot etalon and a corner-cube as reflecting element. Tuning is achieved by lateral movement of the fibre tip, modifying the incidence angle on the Fabry-Perot etalon and thus, modifying its transmission spectrum. Theoretical calculations show a quasi-linear tuning with a wavelength tuning of 8pm per µm displacement of the fibre tip. Experimental results show a similar tuning rate, but required a modification of the etalon to reach a free-spectral range high enough to avoid mode-hopping. Latest results show quasi-continuous tuning over few nanometres with few discrepancies with simulated curve due to the low reflectivity of the etalon mirrors, and accordingly leading to broad transmission peaks. An output linewidth of less than 1.5GHz is achieved, the measured value is resolution-limited by the finesse of the scanning Fabry-Perot used for characterisation.

Continuing on the spectral control problematic, in Chapter 5 we demonstrate a Watt-level source with broad wavelength-tuning in the 2µm wavelength range. By introducing a diffraction grating coupled to a Digital Micro-mirror Device (DMD) in the feedback arm, we demonstrate computer-controlled wavelength-selective feedback. By utilising a DMD for wavelength selection, many benefits are achieved such as fast spectral modulation with a DMD switch time (less than 100µs) allowing quick scanning and potential for high control of the output spectrum. This source wavelength tunability was of more than 130nm from 1913 to 2044nm whilst the expected tuning range was of 140nm according to the setup used, limited by the size of the DMD. An output power of more than 8.5W was achieved, limited by the available pump power, and decreased down to 5.5W at the edges of the available tuning range because of a decrease in feedback efficiency. Good beam quality was conserved at all wavelengths thanks to the single-mode property of the fibre over the entire tuning range with an M^2 measurement varying from 1 to 1.2 during wavelength tuning. Utilising the high reconfigurability of the DMD, crude control over the output bandwidth is detailed with a minimum FWHM of 0.088nm compared to the calculated theoretical value of 0.094nm. The DMD is then utilised to emulate a cavity comprising multiple feedback arms feeding different wavelengths by having multiple reflective areas on the DMD. Each area reflects a specific wavelength, permitting a multi-wavelength behaviour. Exploiting the characteristics of the DMD,

control over the reflectivity for each wavelength can be adjusted by modulating the number of mirrors feeding back the light in the direction orthogonal to the spatial chirp created by the diffraction grating. Up to three wavelengths are demonstrated, but more can be achieved by increasing the number of independent reflective areas and carefully adjusting the feedback efficiency associated with each wavelength in order to ensure lasing at each desired wavelength. A proof of concept is shown for control over the spectral power density where two separate wavelengths are fed back and their output power ratio is modified from 1:1 to 10:1 whilst conserving the same overall output power. This setup allows Watt-level output power with high control over the output spectrum: the number of wavelengths and their positions, and is easily reconfigurable to allow a wider tuning range or better wavelength accuracy. Potential for control over the power density is described and the addition of cylindrical lenses to expand the beam in one dimension is suggested in order to achieve better control over the spectral power density.

In this thesis final experimental chapter, we look at Amplified Spontaneous Emission (ASE) sources tolerating feedback. ASE sources are highly advantageous for fibre systems due to their low temporal coherence and large linewidth, the first one solving the common beam pointing issues related to multi-mode fibres and the second one increasing the Stimulated Brillouin Scattering (SBS) threshold. Reusing a technique previously demonstrated at the Optoelectronics Research Centre based on cavity dynamics, we use an intra-cavity AOM in a fibre source feedback arm with switching time short enough to allow pulse energy extraction whilst avoiding longitudinal modes to appear. The cavity therefore operates as a seed and multi-pass amplifier and generates pulses of ASE light where the output spectrum is based on the fed back light. Combining this with the previous wavelength-tuning arrangement demonstrated in Chapter 5, spectrally-tailored pulsed ASE is generated in a core-pumped architecture for short wavelength generation (1850 to 1950nm) and proof of concept of control of spectral shaping is given. The DMD is used to generate narrow ASE with a FWHM down to 0.15nm and first step for accurate spectral shaping is demonstrated by adjusting the DMD reflective pattern. An improvement of the flatness of a 8nm-wide window is shown. A cladding-pumping setup is then built to allow generation of longer wavelengths, more compatible with an amplifier stage. This second configuration offers tuning from 1970 to 2020nm, reaching up to 1.5kW peak power at 80kHz repetition rate and 600W peak power at 150kHz, limited by pump-power available, with pulses as short as 60ns. This stage is then used as seed for an amplifier stage, power scaling to more than 70W and 4kW peak power, limited by the available pump-power.

In the final section of this chapter, a preliminary design for OPO pumping utilising this source is described, targeting the generation of mid-IR light by the use of a ZGP crystal. Pumping of such a crystal with an ASE has never been achieved before and could lead to interesting results such as control over the output linewidth through adjustment of the pump spectrum. This could be an attractive approach for a better control over mid-IR light generation. Future prospects for this setup will be a study of the generated signal and idler as a function of the ASE seed FWHM combined with a further amplification of the seed to achieve Watt-level of 4µm light. A comparison of the cavity behaviour when pumped by ASE light instead of a laser will also be required.

To conclude, over the different chapters of this thesis, we demonstrated new ways of improving fibre sources, either laser or ASE. We proposed a novel way to improve pump absorption efficiency in cladding-pumping architecture by creating fibres alternating between circular and D-shaped profile. Theses fibres benefitted from the advantages of both profiles: high pump absorption whilst retaining ease of cleave and splice for integration purposes. A way to implement such a fabrication process during fibre draw was discussed. We suggested the utilisation of corner-cubes in feedback arms to remedy output power fluctuations caused by fibre tip movements and an experimental configuration showed improved tolerances up to the millimetre level. Exploiting these improved transverse movement tolerances, we demonstrated wavelength-tuning in a ring laser with potential for rapid accurate tuning and narrow-linewidth output. Prolonging the spectral control theme, a broad CW tunable Tm-fibre laser design was presented achieving Watt-level output power, limited by the available pump power, with tuning over more than 130nm and wavelength targeting accuracy of less than 0.1nm. This system combined a diffraction grating, an imaging system and a DMD and offered capability for multi-wavelength behaviour and a first step towards spectral power density control. Methods are discussed to improve control over the output spectrum. Finally, this tunable laser source is converted into a pulsed tunable ASE source offering tailorable output with kW-level peak power and pulse length in the order of 100ns.This source is then amplified up to more than 70W of average power and utilised here for pumping of a ZGP OPO cavity in order to generate mid-IR wavelengths.

Appendix

Conference papers

A.Billaud, P.C.Shardlow, W.A.Clarkson

Spectrally-tailored thulium-doped fibre amplified spontaneous emission source at two microns

6th EPS-QEOD Europhoton Conference Neuchatel, Switzerland 24-29 Aug 2014 TuP-T1-P-24

A.Billaud, P.C.Shardlow, A.Butler, D.Jain, J.K.Sahu, W.A.Clarkson

High power spectrally-tailorable thulium-doped fibre amplified spontaneous emission source

CLEO/Europe-EQEC '15 Munich 21-25 Jun 2015 Poster

A.Billaud, P.C.Shardlow, W.A.Clarkson

Wavelength-flexible thulium-doped fiber laser employing a digital micro-mirror device tuning element

CLEO 2016 San Jose 5-10 Jun 2016 SM3Q.3

A.Billaud, P.C.Shardlow, K.Boyd, N.Simakov, A.Hemming, W.A.Clarkson

Enhanced pump absorption in double-clad fibres using localised laser-machined mode scramblers

7th EPS-QEOD Europhoton Conference Vienna 21-26 Aug 2016 PO-3.41

Antonin Billaud, Peter Shardlow, and W. A. Clarkson

Narrow-band wavelength-tunable thulium fiber ring laser

CLEO/Europe-EQEC '17 Munich CJ-1.6

Peter C. Shardlow, Nikita Simakov, Antonin Billaud, Jae M. O. Daniel, Pranabesh Barua, Jayanta Sahu, Alexander Hemming, and W. A. Clarkson

Holmium doped fibre optimised for resonant cladding pumping

CLEO/Europe-EQEC '17 Munich CJ-11.4

Journals publications

1. A. BILLAUD, P.C. SHARDLOW, AND W.A. CLARKSON

   Wavelength-agile Tm-doped fiber laser with controllable feedback and multi-wavelength output utilizing a digital micro-mirror device

   Applied Optics (in preparation)
2. A. BILLAUD, P.C. SHARDLOW, AND W.A. CLARKSON

   Enhanced pump absorption in double-clad fibres via localised laser machining of the inner-cladding

   Fibre Optics (in preparation)

3. A. BILLAUD, P.C. SHARDLOW, AND W.A. CLARKSON
   High power spectrally-tailorable thulium-doped fibre amplified spontaneous emission source
   (in preparation)
4. A. BILLAUD, P.C. SHARDLOW, AND W.A. CLARKSON
   Alignment insensitive feedback arrangement for a fibre laser by the use of a corner-cube
   (in preparation)

Section 1

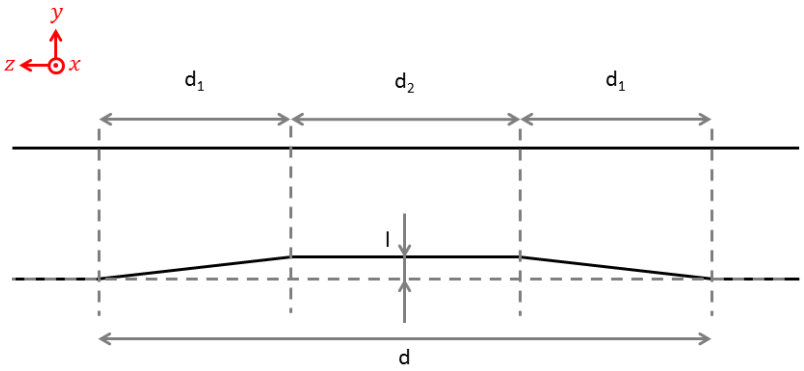

If we call A(z) the removed area of the LMS at the position z, the volume of glass removed V is:

$$V = \int_0^d A(z)dz$$

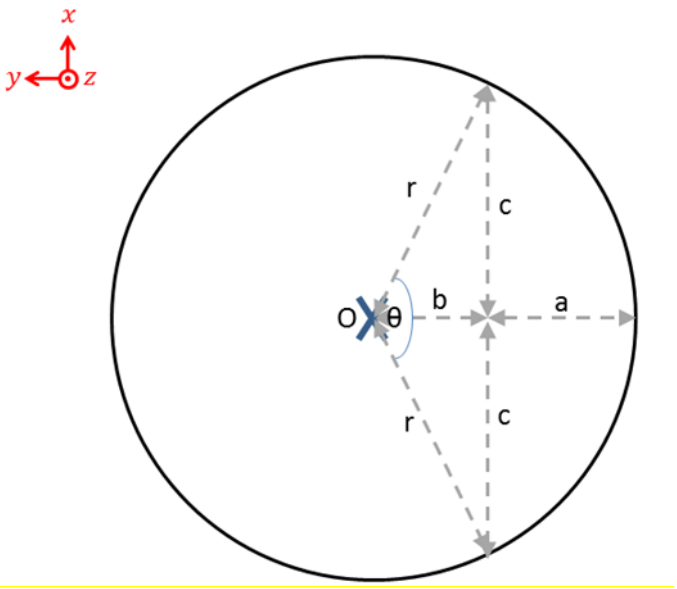

With, according to the previous figure:

$$A(z) = \pi r^2 \frac{\theta}{2\pi} - b.c$$

$$A(z) = \frac{r^2}{2} 2\cos^{-1}\left(\frac{b}{r}\right) - b.\sqrt{r^2 - b^2}$$

As b=r-a where a is the D-shape depth (here up to the value l of 15µm),

$$A(z) = r^2 \cos^{-1}\left(\frac{r-a}{r}\right) - (r-a).\sqrt{2ra - a^2}$$

$$V = \underbrace{\int_{0}^{d_1} A(z)dz}_{V_1} + \underbrace{\int_{d_1}^{d_2+d_1} A(z)dz}_{V_2} + \underbrace{\int_{d_2+d_1}^{d} A(z)dz}_{V_3}$$

$$V = V_1 + V_2 + V_3 = 2V_1 + V_2$$

In V_1, $a = \frac{z}{d_1} l$ and in V_2, $a = l$, leading to

$$V_2 = d_2 \left[r^2 \cos^{-1}\left(\frac{r-l}{r}\right) - (r-l).\sqrt{2rl-l^2} \right]$$

And

$$V_1 = \int_{0}^{d_1} \left[r^2 \cos^{-1}\left(\frac{r-zl}{d_1 r}\right) - \left(r-\frac{zl}{d_1}\right).\sqrt{2r\frac{zl}{d_1} - \left(\frac{zl}{d_1}\right)^2} \right] dz$$

$$V_1 = \int_{0}^{d_1} \left[r^2 \cos^{-1}\left(\frac{r-zl}{d_1 r}\right) \right] dz - \int_{0}^{d_1} \left[\left(r-\frac{zl}{d_1}\right).\sqrt{2r\frac{zl}{d_1} - \left(\frac{zl}{d_1}\right)^2} \right] dz$$

We can write V_1 as $V_{11} + V_{12}$ with

$$V_{11} = \int_{0}^{d_1} \left[r^2 \cos^{-1}\left(\frac{r-zl}{d_1 r}\right) \right] dz = \frac{r^3 d_1}{l} \int_{1-l/r}^{1} \cos^{-1}(y)\, dy$$

$$V_{11} = \frac{r^3 d_1}{l} \left[y \cos^{-1}(y) - \sqrt{1-y^2} \right]_{1-l/r}^{1}$$

And

$$V_{12} = -\int_{0}^{d_1} \left[\left(r-\frac{zl}{d_1}\right).\sqrt{2r\frac{zl}{d_1} - \left(\frac{zl}{d_1}\right)^2} \right] dz = -\frac{d_1}{l} \int_{r-l}^{r} y\sqrt{r^2-y^2}\, dy$$

$$V_{12} = \frac{d_1}{l} \left[-\frac{(r^2-y^2)^{3/2}}{3} \right]_{r-l}^{r}$$

Leading to

$$V = 2V_1 + V_2 = 2V_{11} + 2V_{12} + V_2$$

$$V = \frac{2r^3 d_1}{l} \left[y \cos^{-1}(y) - \sqrt{1-y^2} \right]_{1-l/r}^{1} + \frac{2d_1}{l} \left[-\frac{(r^2-y^2)^{3/2}}{3} \right]_{r-l}^{r} + d_3 \left[r^2 \cos^{-1}\left(\frac{r-l}{r}\right) - (r-l).\sqrt{2rl-l^2} \right]$$

$$V = \frac{2r^3 d_1}{l} \left(\sqrt{1-\left(\frac{r-l}{r}\right)^2} - \frac{r-l}{r} \cos^{-1}\frac{r-l}{r} \right) - \frac{2d_1}{l} \frac{(2rl-l^2)^{3/2}}{3} + d_2 \left[r^2 \cos^{-1}\left(\frac{r-l}{r}\right) - (r-l).\sqrt{2rl-l^2} \right]$$

Section 2

Part 1

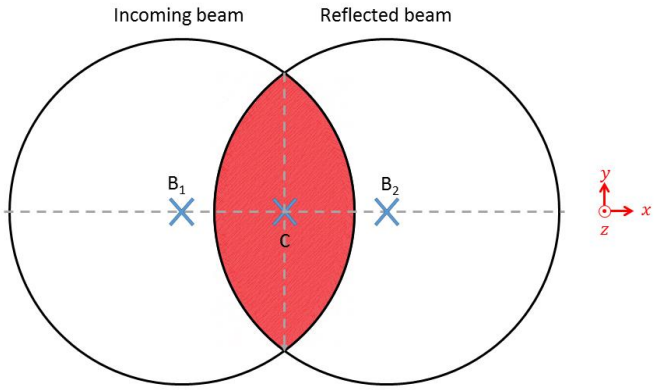

Where C is the apex of the corner cube, B_1 is the centre of the input beam and B_2 the centre of the output beam. If C has for coordinates (0,0), the area S_1 corresponding to this overlap contains all the points P(x,y) such as:

$$P(x,y) \in S_{\text{incoming beam}} \;\&\; P(x,y) \in S_{\text{reflected beam}}$$

To be fed back into the fibre core without NA mismatch, a point P needs to verify the following distance criteria:

$$PB_1 \leq f.NA \;\&\; PB_2 \leq f.NA$$

With $B_1(\frac{d-f}{f}\delta, 0)$ and $B_2(\frac{f-d}{f}\delta, 0)$

$$PB_1 = \sqrt{\left(x-\frac{d-f}{f}\delta\right)^2 + y^2} \;\&\; PB_2 = \sqrt{\left(x+\frac{d-f}{f}\delta\right)^2 + y^2}$$

This corresponds to:

$$P(x,y) \in S_1 \Leftrightarrow \begin{cases} |x| \leq f.NA-\dfrac{|d-f|}{f}\delta \\ |y| \leq \sqrt{(f.NA)^2-\left(|x|+\dfrac{|d-f|}{f}\delta\right)^2} \end{cases}$$

For an input beam centered on $B_1(\frac{d-f}{f}\delta, 0)$ having an intensity profile I(x,y), the corner-cube reflectivity is:

$$R = \frac{\int_{x=-\left(f.NA-\frac{|d-f|}{f}\delta\right)}^{x=f.NA-\frac{|d-f|}{f}\delta} \int_{y=-\sqrt{(f.NA)^2-\left(|x|+\frac{|d-f|}{f}\delta\right)^2}}^{y=\sqrt{(f.NA)^2-\left(|x|+\frac{|d-f|}{f}\delta\right)^2}} I(x,y)\,dxdy}{\iint_{-\infty}^{+\infty} I(x,y)\,dxdy}$$

For an incoming beam having an axial symmetry along the horizontal axis, this becomes:

$$R = 2\frac{\int_{x=-\left(f.NA-\frac{|d-f|}{f}\delta\right)}^{x=f.NA-\frac{|d-f|}{f}\delta}\int_{y=0}^{y=\sqrt{(f.NA)^2-\left(|x|+\frac{|d-f|}{f}\delta\right)^2}} I(x,y)dxdy}{\iint_{-\infty}^{+\infty} I(x,y)dxdy}$$

For a normalised intensity profile we obtain:

$$R = 2\int_{x=-\left(f.NA-\frac{|d-f|}{f}\delta\right)}^{x=f.NA-\frac{|d-f|}{f}\delta}\int_{y=0}^{y=\sqrt{(f.NA)^2-\left(|x|+\frac{|d-f|}{f}\delta\right)^2}} I(x,y)dxdy$$

For a top hat beam, the ratio of this area to the collimated beam area gives the reflectivity of the corner (the latest being considered lossless here).

$$R = 4\int_{x=0}^{x=f.NA-\frac{|d-f|}{f}\delta}\sqrt{(f.NA)^2-\left(x+\frac{|d-f|}{f}\delta\right)^2}\,dx$$

For $z= x+\frac{|d-f|}{f}\delta$

$$R = 4\int_{x=\frac{|d-f|}{f}\delta}^{x=f.NA}\sqrt{(f.NA)^2-z^2}\,dz$$

$$R = 4\left[\frac{z\sqrt{(f.NA)^2-z^2}}{2}+\frac{(f.NA)^2}{2}\sin^{-1}\frac{z}{f.NA}\right]_{\frac{|d-f|}{f}\delta}^{f.NA}$$

$$R = 1-\frac{4}{\pi(f.NA)^2}\left(\frac{|d-f|\delta\sqrt{(f.NA)^2-\left(\frac{|d-f|}{f}\delta\right)^2}}{2f}+\frac{(f.NA)^2}{2}\sin^{-1}\frac{|d-f|\delta}{f^2.NA}\right)$$

Part 2

$$\begin{bmatrix}A & B\\ C & D\end{bmatrix} = \begin{bmatrix}1 & f+\Delta z\\ 0 & 1\end{bmatrix}\begin{bmatrix}1 & 0\\ -1/f & 1\end{bmatrix}\begin{bmatrix}1 & 2d\\ 0 & 1\end{bmatrix}\begin{bmatrix}1 & 0\\ -1/f & 1\end{bmatrix}\begin{bmatrix}1 & f+\Delta z\\ 0 & 1\end{bmatrix}$$

$$\begin{bmatrix}A & B\\ C & D\end{bmatrix} = \begin{bmatrix}1 & f+\Delta z\\ 0 & 1\end{bmatrix}\begin{bmatrix}1 & 0\\ -1/f & 1\end{bmatrix}\begin{bmatrix}1 & 2d\\ 0 & 1\end{bmatrix}\begin{bmatrix}1 & f+\Delta z\\ -1/f & -\Delta z/f\end{bmatrix}$$

$$\begin{bmatrix}A & B\\ C & D\end{bmatrix} = \begin{bmatrix}1 & f+\Delta z\\ 0 & 1\end{bmatrix}\begin{bmatrix}1 & 0\\ -1/f & 1\end{bmatrix}\begin{bmatrix}1-2d/f & f+\Delta z-2d\Delta z/f\\ -1/f & -\Delta z/f\end{bmatrix}$$

$$\begin{bmatrix}A & B\\ C & D\end{bmatrix} = \begin{bmatrix}1 & f+\Delta z\\ 0 & 1\end{bmatrix}\begin{bmatrix}1-2d/f & f+\Delta z-2d\Delta z/f\\ 2d/f^2-2/f & 2d\Delta z/f^2-1-2\Delta z/f\end{bmatrix}$$

$$\begin{bmatrix} A & B \\ C & D \end{bmatrix} = \begin{bmatrix} 1 - 2d/f + (f + \Delta z)\left(2d/f^2 - 2/f\right) & f + \Delta z - 2d\Delta z/f + (f + \Delta z)\left(2d\Delta z/f^2 - 1 - 2\Delta z/f\right) \\ 2d/f^2 - 2/f & 2d\Delta z/f^2 - 1 - 2\Delta z/f \end{bmatrix}$$

$$\begin{bmatrix} A & B \\ C & D \end{bmatrix} = \begin{bmatrix} -1 + 2\Delta z/f\left(d/f - 1\right) & -2\Delta z\left(1 + d\Delta z/f^2 - \Delta z/f\right) \\ 2/f\left(d/f - 1\right) & -1 - 2\Delta z/f\left(d/f + 1\right) \end{bmatrix}$$

Part 3

$$q_1 = \frac{Aq_0 + B}{Cq_0 + D}$$

$$\frac{1}{q_1} = \frac{Cq_0 + D}{Aq_0 + B}$$

$$\frac{1}{q_1} = \frac{Cq_0 + D}{Aq_0 + B} \cdot \frac{B - Aq_0}{B - Aq_0}$$

$$\frac{1}{q_1} = \frac{q_0(BC - AD) + BD - ACq_0^2}{B^2 - A^2 {q_0}^2}$$

As

$$q_0 = \frac{i\pi\omega_0^2}{\lambda}$$

$$\frac{1}{q_1} = \frac{\frac{i\pi\omega_0^2}{\lambda}(BC - AD) + BD - AC\left(\frac{i\pi\omega_0^2}{\lambda}\right)^2}{B^2 - A^2\left(\frac{i\pi\omega_0^2}{\lambda}\right)^2}$$

$$\frac{1}{q_1} = \frac{\frac{i\pi\omega_0^2}{\lambda}(BC - AD) + BD + AC\left(\frac{\pi\omega_0^2}{\lambda}\right)^2}{B^2 + A^2\left(\frac{\pi\omega_0^2}{\lambda}\right)^2}$$

$$\mathrm{Im}\left(\frac{1}{q_1}\right) = \frac{\frac{\pi\omega_0^2}{\lambda}(BC - AD)}{B^2 + A\left(\frac{\pi\omega_0^2}{\lambda}\right)^2} = -\frac{\lambda}{\pi\omega_1^2}$$

$$\omega_1^2 = -\frac{\lambda^2}{\pi^2\omega_0^2}\frac{B^2 + A\left(\frac{\pi\omega_0^2}{\lambda}\right)^2}{(BC - AD)}$$

$$\omega_1 = \frac{\lambda}{\pi\omega_0}\sqrt{\frac{B^2 + A\left(\frac{\pi\omega_0^2}{\lambda}\right)^2}{(AD - BC)}}$$

Part 4

$$\frac{P_1}{P_2} = \frac{1\text{-}R_1}{1\text{-}R_2}\sqrt{\frac{R_2}{R_1}}$$

$$\frac{P_1}{P_2}\frac{\sqrt{R_1}}{1\text{-}R_1} = \frac{\sqrt{R_2}}{1\text{-}R_2}$$

$$\left(\frac{P_1}{P_2}\frac{\sqrt{R_1}}{1\text{-}R_1}\right)(1\text{-}R_2) = \sqrt{R_2}$$

$$\left(\frac{P_1}{P_2}\frac{\sqrt{R_1}}{1\text{-}R_1}\right)^2 (1\text{-}R_2)^2 = R_2$$

$${R_2}^2\text{-}\left(2 + \frac{1}{\left(\frac{P_1}{P_2}\frac{\sqrt{R_1}}{1\text{-}R_1}\right)^2}\right) R_2 + 1 = 0$$

$${R_2}^2\text{-}\left(2 + \frac{{P_2}^2(1\text{-}R_1)^2}{{P_1}^2 R_1}\right) R_2 + 1 = 0$$